THESIS FOR THE DEGREE OF DOCTOR OF PHILOSOPHY

Facing Complex Soft Matter: Tools, Validation, and Case Studies

CARL MIKAEL FROSTENSON

Department of Microtechnology and Nanoscience (MC2)
Electronics Materials and Systems Laboratory
Chalmers University of Technology
Göteborg, Sweden, 2024

Facing Complex Soft Matter:
Tools, Validation, and Case Studies
CARL MIKAEL FROSTENSON
ISBN 978-91-8103-061-7

Doktorsavhandlingar vid Chalmers tekniska högskola
Ny serie nr 5137
ISSN 0346-718X

Electronics Materials and Systems Laboratory
Department of Microtechnology and Nanoscience (MC2)
Chalmers University of Technology
SE–412 96 Göteborg
Sweden
Telephone +46 (0)31-772 1000

Cover: Illustration of polymer Spheurlite

Chalmers Digitaltryck
Göteborg, Sweden, 2024

Facing Complex Soft Matter:
Tools, Validation, and Case Studies
CARL MIKAEL FROSTENSON
Electronics Materials and Systems Laboratory
Department of Microtechnology and Nanoscience (MC2)
Chalmers University of Technology

Abstract

We face a complex soft matter challenge where ab-initio theory can offer unique insight. The behavior of soft matter reflects the competition between intricate intermolecular interactions and subtle energy balances. Most of those problems are complex, that is, we lack complete experimental characterizations. In fact, empirical characterization of these systems are difficult because the systems can easily change under external stimuli. This status is a challenge for traditional material theory that normally relies on at least some measurement input: with complex soft matter we must start by making plausible predictions for the structure that may have multiple relevant phases.

This thesis develops computational tools and methods capable of predicting and analyzing the behavior of complex soft matter. We advance the application of Density Functional Theory through the development of new computational tools, notably a range-separated hybrid van der Waals Density Functional (vdW-DF) called AHCX. AHCX integrates non-local correlation and exchange mechanisms, demonstrating enhanced accuracy and transferability across various problems, from thermophysical properties in bulk materials to molecular and adsorbate systems. Additionally, this thesis work documents the implementation of the vdW-DF spin-stress tensor in Quantum ESPRESSO, enabling efficient predictions of spin-polarized systems and magnetic properties.

We apply AHCX, and the latest range-separated hybrid vdW-DF termed AHBR, to characterize the activation of oxygen in complex catalytic systems such as Cu-Chabazite zeolites and enzymatic crystals. We prove the utility of these functionals in accurately modeling both chemical and physical binding without empirical adjustments.

Finally, I introduce our methods and tools to study the properties of orthorhombic phases of polyvinylidene fluoride (PVDF) and polyvinyl fluoride (PVF). We contrast these with those of polyethylene (PE) using the related vdW-DF-cx functional. Unlike PVDF and PE, PVF lacks a definitive experimental consensus on its structure, and is an example of a complex soft-matter problem. We validate vdW-DF-cx's accuracy with PE and PVDF and extend our analysis to the PVF system, allowing for the impact of thermal excitations. This investigation furthermore predicts PVF's mechanical behavior, polarization response, and plastic deformation.

In summary, the thesis seeks to enhance the understanding of complex soft matter and improve theoretical tools for predicting their behavior.

Keywords: Density Functional Theory, Soft Matter, Complex Matter, Catalysis, Flourinated Polymer Crystals, Spin-Polarized Systems, van der Waals Density Functionals

Acknowledgments

I am grateful to my supervisor, Per Hyldgaard, whose vast knowledge and boundless enthusiasm have continually motivated and inspired me throughout my research journey. His guidance has been instrumental in shaping my academic pursuits.

I am similarly thankful to my co-supervisor, Henrik Grönbeck, for enriching my experience with his insights and engaging discussions. Participating in the theory meetings within his group has been particularly rewarding.

I owe a debt of gratitude to Jochen Rohrer, for his assistance with MTP and LAMMPS, and for our enlightening discussions on machine learning, all of which have greatly expanded my understanding of computational methods.

I am also thankful to Pär A.T. Olsson, whose expertise in polymers, and straightforward and kind approach, have been immensely beneficial.

I am truly thankful for the camaraderie and intellectual stimulation provided by my office mate, Vivekanand Shukla. Our discussions on physics, politics, and life in general have taken me through some dark times, broadening my perspectives and opening my eyes.

I appreciate the collegial atmosphere and stimulating conversations with my colleagues at AQP and EMSL. The shared moments of fun and laughter during lunch, fika, and afterwork gatherings have made my time at Chalmers truly memorable.

I am ever grateful to my friends, who have supported me through thick and thin—the Gothenburgers of old, whom I almost thought I'd lost, and the steadfast love and support from my brothers in Stockholm.

Family is the bedrock of my life, and I am forever thankful for the unwavering support and love from my parents, my sister, and my extended family.

Most importantly, I am deeply thankful to my girlfriend, Gabriella Ivarsson, for her unwavering support and love, which has surpassed all my expectations. Her wisdom, ingenuity, and subtle guidance have been my anchor in times of both struggle and celebration.

Carl Mikael Frostenson, Göteborg, May 2024

List of publications

This thesis is based on the following papers:

A Hard and soft materials: Putting consistent van der Waals density functionals to work
Carl M Frostenson, Erik Jedvik Granhed, Vivekanand Shukla, Pär A T Olsson, Elsebeth Schröder, Per Hyldgaard
Electronic Structure, 4(1), 014001, 2022

B vdW-DF-ahcx: A range-separated van der Waals density functional hybrid
Vivekanand Shukla, Yang Jiao, **Carl M Frostenson**, Per Hyldgaard
Journal of Physics: Condensed Matter, 34(2), 025902, 2021

C Range-Separated Hybrid van der Waals Density Functional to Describe Cu_2O_2-complexes
Carl M Frostenson, Yingxin Feng, Per Hyldgaard, Henrik Grönbeck
Being revised for resubmission

D Fluorinated Polymer Crystals: Structure predictions, nature of slippage, and possibility of finite-temperature ferroelectricity in a complex soft material
Carl M Frostenson, Pär A.T. Olsson, Per Hyldgaard
Submitted to Physical Review Materials

Contents

Chapter 1

Introduction

1.1 What is Soft Matter?

Soft matter systems is a broad category encompassing materials distinguished by their inherent flexibility, weak restoring forces, and their large response to external stimuli. Soft matter includes a diverse array of substances such as polymers, phospholipids, and DNA, each demonstrating distinctive behaviors that challenge the conventional understanding of solid and liquid states.

The effects of feeble restoring forces is particularly noticeable in substances like polymers and DNA. In these systems, thermal fluctuations often overshadow elastic forces, playing a significant role in determining their behavior. As a result, the dynamics of these materials is an interplay between thermal fluctuations and internal energy. An illustrative example given by Feynman [1] is that of a rubber band returning to its original shape after being stretched - a process driven by the thermal motion of the polymer chains.

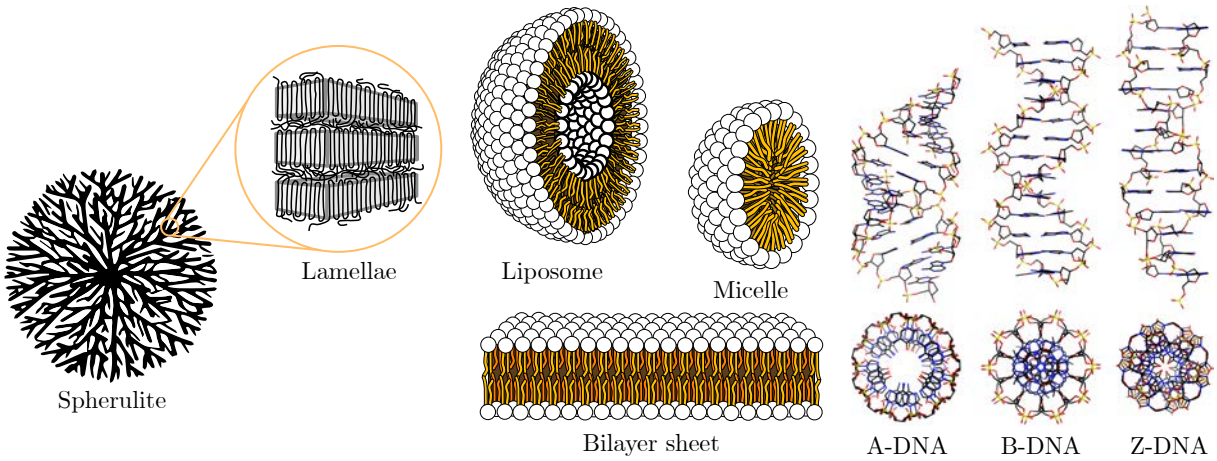

Figure 1.1: Representative structures of soft matter systems showcasing polymers (spherulite and lamellae), phospholipids (liposome, nicelle, and bilayer sheet), and DNA conformations (A-DNA, B-DNA, Z-DNA). These illustrations demonstrate the diverse and flexible nature of soft matter, highlighting their complex behavior under thermal fluctuations and van der Waals interactions. Many of the figures are taken from wikimedia commons.

The diversity in material states due to small energy variations is another cornerstone of

soft matter. Soft matter systems can adopt numerous low-energy configurations, leading to a multitude of stable or metastable states. This is evident in polymers and in DNA, which exhibits multiple conformations such as A, B, and Z, see Figure 1.1. Each of these states arises from and contributes to the material's unique properties.

In the realm of soft matter, the role of van der Waals (vdW) interactions cannot be overstated. These interactions arise from the phenomena of fluctuating polarization due to zero point fluctuations of the electron cloud. For substances ranging from polymers to DNA, vdW forces act as an essential intermolecular force that dictates long range structure and stability without the need for strong covalent bonds. This balance plays a critical role in the formation of the complex structures observed in soft matter. For instance, the self-assembly of phospholipids into bilayers, a fundamental process for the formation of cell membranes, is largely driven by vdW forces alongside hydrophobic interactions. Similarly, the conformational flexibility of polymers and the double helix structure of DNA is governed by the interplay of vdW, electrostatic and steric interactions. vdW interactions stabilize specific structures and configurations while allowing for the dynamic responses characteristic of soft matter. Thus, an accurate understanding and modelling of vdW forces is central to comprehending the details of soft matter behavior and its sensitivity to external stimuli.

1.2 What is Complex Soft Matter?

The central theme of this thesis is the development of tools for investigating complex materials, where complex means atomic systems and structures with limited or incomplete experimental characterizations. In the realm of complex soft matter, characterization and analysis is often challenging due to the interplay of interaction scales and delicate energy balances.

Perovskites is one class of materials that can act as testing ground. Before we can trust our tools to accurately predict properties of complex soft matter systems, we of course have to test and verify their capabilities. This leads us to also study systems that exhibit near-order characteristics. Such systems serve as a preliminary testing ground for our computational tools and methodologies, allowing us to refine our approaches in a controlled environment.

Their well-defined yet flexible structural properties offer a balance between order and soft complexity, in the form of vibrations leading to incipient or actual phase transitions [2–5]. This makes perovskites one type of suitable objects for honing our analytical techniques and, at Chalmers, we test our methods on this important class of materials [6–9].

The discussion presented below exemplify the need for rigorous theoretical computational tools in the study of the ubiquitous class of complex soft matter.

1.2.1 Semi-Crystalline Polymers: Complexity and Function

In polymer science, interaction between different crystalline and amorphous regions showcases the complexity in dispersion interactions and size effects. In Figure 1.2 we illustrate some different applications of polymers, such as food coatings and hearing aids, whose macroscopic properties relevant to these applications emerge from a detailed web of microscopic interactions. Experimentally characterizing these interactions is challenging due to the multitude of variables and the nature of the forces involved.

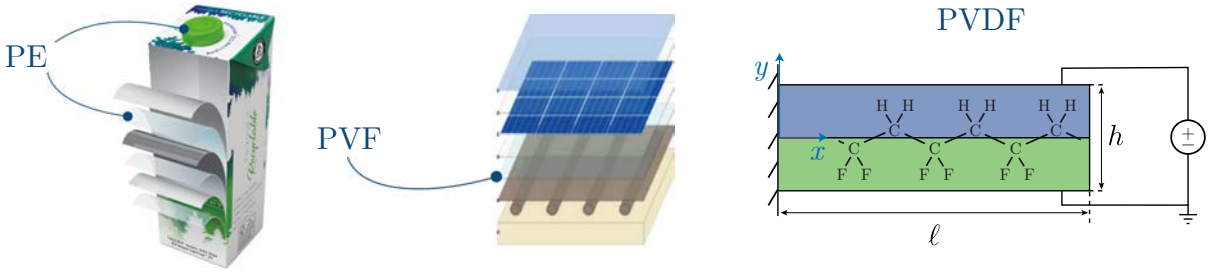

Figure 1.2: Illustration of multifunctional applications of polymers. Left: Use of polyethylene (PE) in recyclable packaging. Middle: Layered polyvinyl fluoride (PVF) in solar panel construction. Right: Cross-sectional diagram of a polyvinylidene fluoride (PVDF) film in a piezoelectric device setup, illustrating its molecular structure and electrical connections.

Semi-crystalline polymers exhibit a large variety of properties, largely dictated by their inherent structural polymorphism and the interplay between their crystalline and amorphous regions [10–12]. These materials are characterized by their ability to exist in different crystalline forms, also known as polymorphs, each with distinct molecular packing and orientation. The polymorphic nature significantly influences the physical characteristics of the polymers, including mechanical strength, thermal resistance, and polarization response.

The complexity in semi-crystalline polymers emerges not only from their molecular composition and the presence of multiple phases but also from the dynamic nature of these phases under varying thermal and mechanical conditions. Each crystal phase exhibits unique properties that are hard to isolate in experiments, being highly sensitive to processing conditions, such as cooling rates and mechanical stretching.

The crystalline regions of these polymers provide structural rigidity and contribute significantly to the tensile strength and thermal stability. Conversely, the amorphous regions impart flexibility and impact resistance, which are critical for applications where materials must absorb energy without fracturing. The amorphous phase facilitates the mobility of polymer chains, allowing the material to deform under stress. This phase is also crucial in governing the glass transition temperature of the polymer, a fundamental thermal characteristic that defines the operational temperature range of the material [13–15]. The degree of crystallinity — a ratio depicting the amount of crystalline material relative to the amorphous matrix — thus directly influence many of the properties of semi-crystalline polymers.

The interaction between the amorphous and crystalline phases is particularly evident in the stress-strain behavior of semi-crystalline polymers. During deformation, the amor-

phous regions deform first, providing initial ductility. As the strain increases, the load is transferred to the crystalline regions, which then contribute to the material's strength and stiffness. The behaviour is not merely of academic interest: the phase interplay is critical in applications requiring a balance between strength and flexibility, such as in automotive parts and packaging materials [16–18].

Advanced computational modeling techniques, including density functional theory (DFT), molecular dynamics and finite element analysis, are important to investigate and predict the behavior of these polymers under controlled conditions. DFT helps predict the structural and electronic properties of the crystal phases, while molecular dynamics simulations provide insights into the mechanical response of the larger polymer system at for, e.g., interphase boundaries. Finite element analysis complements these techniques by modeling the macroscopic behavior of the material under different loading conditions. Understanding the contributions of different phases and their interactions, enables design of polymers with optimized properties for specific applications.

In summary, the polymorphic nature and the interplay between crystalline and amorphous phases endow semi-crystalline polymers with a varied set of properties that, once understood, can be finely tuned through material processing. Their complexity presents a challenge to empirical material characterization techniques. We need better computational tools to predict and optimize the performance of polymer-based materials.

1.2.2 Engineering Molecular Function

Molecular crystals, especially those used in pharmaceuticals, is a challenging area soft matter research due to their intermolecular interactions defining both macroscopic properties and biological activity. The characterization of molecular crystals involves a detailed understanding of their structure, often complicated by the existence of different polymorphs. Here each polymorph (crystal phase) can exhibit vastly different solubility, stability, and bioavailability [19–21].

From a theoretical perspective, accurately predicting the stability of different polymorphic forms requires advanced computational techniques. DFT, particularly with the incorporation of van der Waals interactions through exchange-correlation (XC) functionals such as those from the van der Waals density functional (vdW-DF) method, provide a critical tool for this. The ability of vdW-DFs (i.e. the XC functionals of the method) to account for dispersion forces is crucial in modeling the weak intermolecular forces that dominate the structure and stability of soft matter molecular crystals [22].

Dispersion interactions, although weak compared to covalent bonds, determine the packing of molecules within the crystal lattice. Understanding these forces allows for the prediction of lattice structures and, consequently, the physico-chemical properties of the crystals. Such predictions are essential for the design and development of new pharmaceutical compounds with optimized properties [23–25].

The computational modeling of molecular crystals poses several challenges. First, the accurate representation of the crystal's electronic structure requires a functional capable of handling non-local interactions. The non-empirical nature of the vdW-DF formulations is advantageous in this context, making prediction of novel crystal structures possible without the need for synthesis. Furthermore, the inherent anisotropy in molecular crystals, due to directional bonding and molecular shape, often complicates the computational study, necessitating a careful set-up of the calculation parameters.

In Figure 1.3, we compare a set of vdW-inclusive XC functionals using the GMTKN55

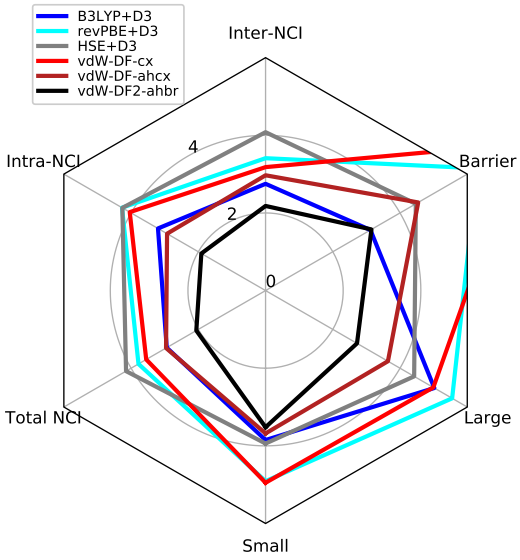

Figure 1.3: Comparison of performance for vdW-inclusive functionals asserted against coupled-cluster quantum chemistry reference values across the GMTKN55 benchmark suite [26] for broad molecular properties. The radar plot report weighted mean absolute deviations (so-called WTMAD1) values in kcal per mol, sorting a total of 55 benchmarks (2500 individual calculations) into groups of small chemical-system reaction energies ('Small'), large-system reaction enegiers and isomerizations ('Large'), barrier heights across small and cyclic molecules ('Barrier'), as well as non-covalent interactions ('NCI') energies. The latter group is subdivided into benchmarks covering both intra- and intermolecular NCI binding problems. The reference calculations are defined in Ref. [26].

molecular benchmark set, focusing on these discussed in this thesis. The benchmark was constructed to evaluate functional performance on non-covalent interactions (NCIs), reaction energies (small and large), and barrier heights (transition states) by comparison with high-precision quantum chemistry calculations. This radar plot contrasts the weighted mean average total deviation (WTMAD1) in kcal/mol of vdW-corrected range-separated hybrid (RSH) functionals from orbital-based (B3LYP+D3) and plane-wave based studies (HSE+D3), against non-hybrid vdW-DF-cx (CX), and the RSH vdW-DF-ahcx (AHCX) launched in this work. It also reports the performance of the most recent RSH vdW-DF2-ahbr (AHBR). Generally, orbital-based codes (B3LYP+D3) are more effective for molecular systems, with HSE+D3 (and the new AHCX,AHBR) excelling in extended systems. CX performs remarkably well for a non-hybrid functional — better than HSE+D3 for NCI systems — the only outlier being the 'Barrier' group of benchmarks. A primary motivation for developing RSH vdW-DFs was to enhance the accuracy of the vdW-DF method on such transition state energy predictions. Both AHCX and AHBR demonstrate robust performance across various systems. AHCX rivals B3LYP+D3 except in Inter-NCI and barrier categories and surpasses HSE+D3 except on barriers. AHBR leads in all categories, tying with B3LYP+D3 on barriers.

The implications of performance progress extend to the realm of drug development and other fine chemicals. By accurately predicting the behavior of various crystal phases, pharmaceutical scientists can enhance control over production processes, optimize drug formulations, and ensure consistent and effective drug delivery systems. This underscores

the potential utility of DFT studies in pharmaceutical research and crystal engineering, potentially enhancing the ability to tailor drug properties to specific therapeutic needs [27–29].

1.2.3 Enzymatic Crystals and Single-Atom Catalysis: Structural Flexibility and Catalytic Efficiency

One of the main challenges for complex soft matter, is the need for a good description of weak interactions and charge transfer processes.

On the one hand, enzymatic crystals are highly ordered structures that maintain a balance between rigidity and flexibility, essential for efficient catalysis [30, 31]. These crystals stabilize transient states in catalytic cycles, enhancing enzyme activity [32]. The adaptability of these structures allows for necessary conformational changes during substrate interaction [33], while integrated water molecules often play a critical role in catalysis by mediating interactions within the crystal lattice [34].

On the other hand, few-atom catalysis, exemplified by zeolites and Cu-Chabazite, showcases a different paradigm where pairs of metal atoms exist in complexes that are mobile within a robust inorganic matrix [35–39]. This means that they may relocate to places where the doping of the framework can facilitate charge transfer that enhances the function. The isolation as a charged Cu-complex is crucial for maintaining high catalytic activity and selectivity, as it prevents the metal atoms from clustering into less reactive forms. Here the complexity is twofold: it involves the details of the catalytic sites and the subtleties of charge transfer processes [40]. The interaction between d-orbitals and reactants presents a significant challenge for experimental characterization. At the same time, the effectiveness of such few/single-atom catalysts is heavily dependent on the electronic environment which needs to be well understood to be precisely tailored to enhance reactivity and stability.

Bridging experimental techniques with theoretical and computational methods enriches our understanding of these systems. Tools like X-ray crystallography, NMR spectroscopy, and advanced microscopy, needs to be integrated with accurate theoretical predictions to provide a comprehensive picture of the catalytic mechanisms at play. While the dynamic nature of active catalysis challenges traditional static models, computational methods like DFT and molecular dynamics offer insights into the reaction pathways that govern catalytic activity — that is, as long as the XC functional delivers sufficient accuracy on transition state problems.

1.3 Importance of Computational Tools

With the advancement of highly efficient computational tools, the study of complex soft matter has entered a new era of discovery and understanding. For soft matter, where direct observation and measurement can alter the material properties themselves, computational models provide non-intrusive means to predict and analyze their behavior under various conditions. This opens up new possibilities not only for hypothesizing new materials and their properties but also for understanding fundamental interactions and properties at the atomic level.

Ab-initio, and thus parameter-free DFT has consequently emerged as the cornerstone

of computational materials science. Providing the scientific community with the ability to probe complex soft systems with the precision and depth they require. Yet, even the advanced capabilities of robust DFT methods like the conventional PBE [41] or the consistent-exchange vdW-DF-cx (CX) [42], a product of the Chalmers vdW-DF development program, are not always enough in themselves to deal with the features of complex soft matter. For example, many DFT codes lack the features or implementation necessary to extract predictions that are optimal for experimental validation in specific systems.

We take a magnetic perovskite as a simple example. Perovskite structures also warrant a good understanding of weak interactions acting in concert with charge transfer. These materials are distinguished by their strong correlations, soft modes and multiferroic properties. Each of these properties is crucial for their use in applications such as solar cells and computer memory. The soft phonon modes in these materials introduce variability and flexibility, suggesting that a single structural snapshot might not fully represent their functional state [5, 7, 43–46].

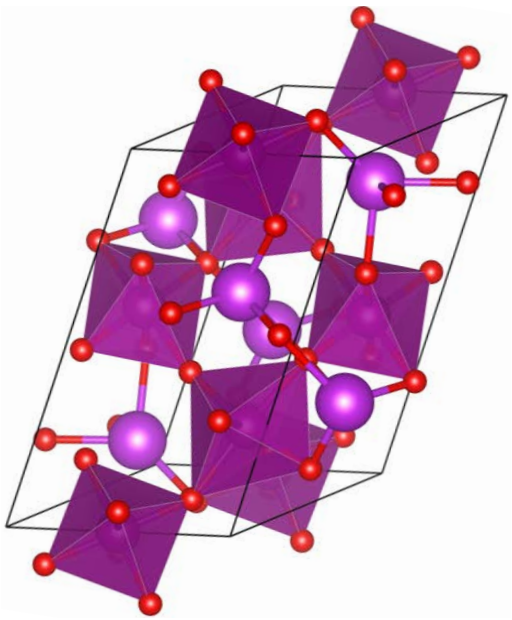

Figure 1.4: The unit cell of $BiMnO_3$ with the MnO_6 octahedra and Bi atoms. The MnO_6 octahedra are corner-sharing, and the Bi atoms are located in between these octahedra.

In this thesis we introduce tools to enhance the capabilities of DFT based on the Chalmers-Rutgers vdW-DF method. As an example, consider the unit cell of ferromagnetic $BiMnO_3$ with 4 lattice parameters, as depicted in figure 1.4. To comprehensively map out the entire 4D space of lattice parameters for this material, one would need to perform approximately $10^4 = 10000$ fixed-cell DFT relaxations. Using our spin-stress tensor implementation, we can reduce this to a single variable-cell calculation. This approach forms one part of this thesis, wherein we enhance the capabilities of DFT by incorporating both spin and mechanical stress analysis into a cohesive spin-stress tensor within the vdW-DF method framework. With this tool, we are, for example, set up to predict the interplay between magnetic properties and structural stability in spin-polarized soft matter systems.

Accuracy and transferability in the choice of non-empirical functional is essential exactly because we need to trust it to make predictions. We have found that while CX is very often highly accurate, it is challenged when we need it to compute energies of systems

that have very electron densities. This may happen in transition states [47], but can also happen on when a weak binding causes a large amount of electron relocation [48].

For those harder cases, we have at Chalmers and with international collaborators recently developed range-separated hybrids (RSH) vdW-DFs: vdW-DF-ahcx (AHCX) [49] and vdW-DF-ahbr (AHBR) [47]. In this thesis we include the work towards the formulation and launch of AHCX. It is a systematic extension of the consistent-exchange CX version, which integrates both truly non-local correlation and truly non-local exchange within the electron-gas framework. AHBR is the corresponding extension of another regular vdW-DF functional called vdW-DF2-B86r. Both of these new RSH mix in a partly screened Fock exchange. As we shall also see in this thesis, AHCX and AHBR are truly general-purpose functionals, excellent for many applications.

Figure 1.5 shows an example from catalysis where CX is not aligned with the little data that exists for the case of O_2 dissociation over pairs of $Cu(NH_3)_2^+$ in copper chabazite (Cu-CHA). Cu-CHA is a zeolite — a microporous, aluminosilicate mineral — characterized by the incorporation of copper ions within its framework. The copper ions act as a catalytic site in applications of selective catalytic reduction of NOx gases, often in diesel engines [50]. The figure shows the relative energy as predicted by a set of different functionals for each of the reaction steps C1-C5, with a spin-flip transition state TS (between C2 and C3), as the O_2 molecule is split at the active site of the copper ions. All of the functionals qualitatively agree on the relative trends up to the actual dissociation step from C4 to C5. Both CX (cyan) and PBE using the D3 dispersion correction (blue) favour complete dissociation. The same is true for the standard PBE (black). Experiments indicate that the proper reaction stops at the C4 step, just short of complete dissociation, and so C4 should be the lower energy state.

To accurately describe the C4 structure (and the C4-C5 energy difference), the functional has to be able to reproduce the 3d-localization of the Cu-O bond, while simultaneously treat the dispersion interactions with the zeolite framework. With the well-known potential for delocalization errors in non-hybrid functionals, it comes as no surprise that one needs the RSH extension of PBE, HSE, together with D3 corrections (green) to accurately predict the stability of C4. One can also deal with the exchange-interaction between the 3d-states of Cu by including the ad-hoc Hubbard U term to PBE. In that case the value of U was determined from fitting to experimental data relevant to this exact reaction. With such an empirical approach, PBE+U recovers the correct preference for C4, see Figure 1.5. The fact that PBE+U prefer the correct state both with (dark brown) and without D3 (pink) is also not that surprising: the vdW-interaction energy is small in comparison to the localization effect.

We furthermore observe that the semiempirical vdW-inclusive BEEF functional also manages to make correct predictions without any Fock exchange or U term. This is notable, albeit not unexpected, given that it has been designed through optimization over experimental data — including catalysis experiments. In **Paper C** we return to this problem, armed with the latest RSH vdW-DFs to tackle this problem without the need for any empirical input or corrections.

The development and adherence to best practices in computational materials science ensure that the results are robust, reproducible, and verifiable. A systematic workflow from the initial design of the computation to the interpretation of results - that has been extensively validated and then publicized - is the way to achieve reproducible results and contribute to computational materials science. This challenge is compounded by the fact that computational studies of complex systems often generate large data sets that

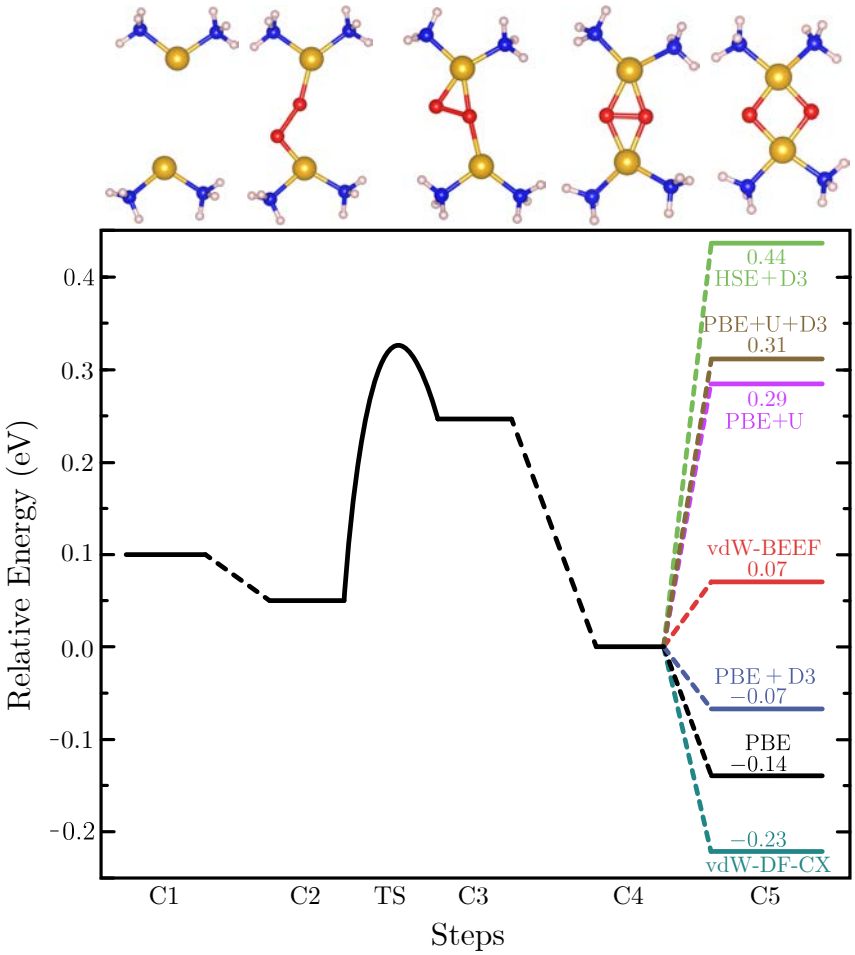

Figure 1.5: The potential energy landscape of direct O_2 dissociation on $Cu(NH_3)_2^+$-pairs in CHA by different functionals. Data for trend taken from Ref. [40]; we focus on reporting (previous) results for the C4-C5 energy difference. The structure for each step is shown on top, atom color codes: copper (yellow), nitrogen (blue), oxygen (red) and hydrogen (white). The triplet to singlet transition for O2 occurs between steps C2 and C3. 'TS' stands for the transition state from C2 to C3.

are difficult to manage effectively. There is a risk of data mismanagement (e.g. false or redundant entries) or analysis errors.

In this thesis we strive to avoid these problems by utilizing Python scripting for automation of generation, and analysis, of data. We deliberately attempt to stay clear of empirical methods, avoiding the use of standard EOS fitting procedures by using a formal lattice parameter expansion when computing thermophysical properties. To confirm the validity of our approach, we rigorously validate our scheme by ensuring consistency between two complementary methods under conditions where they are expected to agree. Additionally, to reduce computational cost when studying crystalline polymers, we design a computational scheme to avoid any unphysical stretching of the individual polymer chains. This approach provides an initial input to the subsequent DFT calculation that is closer to the distorted configuration we need. Consequently, it reduces the number of fixed-cell relaxation steps required to map out the polymers' energy landscapes along the lattice parameters. There is an added benefit in that the approach does not get trapped in what could be a local minima of some distorted (unrelated) system. Similarly, this

method enables the prediction of elastic coefficients without the spurious contributions from covalent interactions, which should not be included in low-order elastic constants. By aligning polymer chains along the c-axis and utilizing the ASE library within our Python scripts, we can precisely manipulate the positions of individual chains within the unit cell without distorting covalent bonds. We also thus streamline the workflow for the prediction of the spontaneous polarization. It enables straightforward rotation of monomers and efficient parallel execution of DFT computations for multiple phases and angles. Most of this code is already available on request and will be released after our preprints are accepted. The idea is to provide other researchers with the opportunity to access, adapt, utilize, and modify it according to their specific needs

Overall, the integration of computational tools in the study of complex soft matter is far from merely a supplement to experimental approaches; they are a foundational component in the modern scientific investigation of these materials. By enabling precise control over variables, providing insights where experimental challenges limit direct observation, DFT and computational tools hold the key to understand many of the details that are still obscure within the field of soft matter. Towards this end, we address some of the limitations in current DFT implementations and methodologies in the upcoming sections. Our aim is contribute to both theoretical foundations and tools together as well as to give practical simulation schemes in the study of complex soft matter systems.

1.4 Outline of Thesis

In this thesis we introduce new vdW-DF functionals, hybrid functionals, and computational workflows that we argue are tailored to help meet the specific needs of facing complex soft matter systems by a computational approach. This chapter provides the context and setting for the work presented in this thesis. Chapter 2 provides a summary of the theory needed to develop the RSH vdW-DF within the Chalmers-Rutgers framework. We go from the Hamiltonian to the functional approximations LDA, GGAs and vdW-DFs. We also cover the formulation of global and range-separated hybrids. We briefly touch on similar methods to give some context of our vdW-DF method work.

In chapter 3 we provide some theoretical background and details of the tools and methods we develop in the studies included in this work. In the first section we outline the details of the theory behind the vdW-DF spin-stress tensor we implemented within the Quantum ESPRESSO (QE) suite [51–53] in **Paper A**. he workflow for structure search in nearly ordered soft matter is introduced in the second section; this is the method used to determine the plausible ground state of PVF in **Paper D**. In the third section we outline the method and workflow implemented in Python, needed in the benchmark work of **Paper B** and structure optimization of polymers in **Paper A** and **Paper D**. The supercell method for studying the plastic slip-deformation of polymers in **Paper D**is introduced in the fourth section. We end the chapter by outlining the method of 'modern theory of polarization' used to compute the polarization of polymers, also used in **Paper D**.

In chapter 4 we summarize and contextualize the results from the work in the included papers. The first section summarize the benchmarking of thermophysical properties for both AHCX and AHBR, while comparing to CX, PBE, and HSE. The second section contains the work towards characterizing catalysis and enzymatic systems using AHCX and AHBR. We close the chapter with a characterization of orthorhombic polymers, as a

simple demonstrator case. We report our works to provide multiple property predictions by ab-initio theory for the PVF complex matter problem. The logic is that by delivering a set of predictions, one may use any one of possible future experimental characterizations as a validation test. Once we have such validation we can furthermore use the rest of the set of theoretical characterizations as a substitute for actual measurement.

In the fifth and final chapter we summarize the findings from the four papers included herein. We also argue for our choice of focusing the implementation work on open source software and our dedication towards a collaborative environment in computational materials science. The thesis is concluded with future perspectives on the vdW-DF method and generally improving computational tools and methods for the study of complex soft matter.

Chapter 2

Theory for Complex Soft Matter

In this chapter we introduce what we call the theoretical framework for complex soft matter. It is the DFT-based framework that does, in fact, strives to cover all types of material problems: DFT is in principle exact for simple ground state properties, such as structure. A balanced inclusion of vdW-forces in the defining DFT approximation, namely the exchange-correlation (XC) functional the renders DFT practical, has long presented a challenge. The Chalmers-Rutgers vdW-DF program for developing vdW-inclusive XC functionals systematically emphasize a general-purpose capability so that we can also reliably cover weak interactions in efficient computations. However using such truly non-local DFT for complex soft matter requires extra and sharper computational tools and techniques.

The main focus remains accuracy and efficiency in a new vdW-inclusive approximation that is based on understanding the electron gas behavior. The foundations of DFT were developed in the later half of the 20th century [54–60]. We start by introducing the full electronic Hamiltonian, and then proceed to the density formulation of DFT. The theory's effectiveness is well documented [61, 62], for hard materials with a dense electron distribution [41, 63] and for molecules [64]. We then introduce the Kohn-Sham scheme for highly efficient studies that exploits introduction of a universal XC functional. From there we furthermore introduce the vdW-DF and its RSH form.

2.1 Density Functional Theory (DFT)

2.1.1 Full Electronic Hamiltonian

To model complex matter from first principles, we need to accurately describe the interactions among atomic nuclei and electrons. We also need to compute the implications for properties defined by the response of the ground state by solving the many electron Schrödinger equation. The interplay of interactions form the cornerstone of understanding materials at scales where quantum mechanical effects manifest. The full non-relativistic, stationary description of matter is encapsulated in the Hamiltonian for a system of N_e electrons and N_N nuclei, which can be written as [65]:

$$\hat{H}_{\mathrm{N+e}} = \hat{H}_{\mathrm{N}} + \hat{H}_{\mathrm{e}}, \tag{2.1}$$

where H_{N} is the Hamiltonian for the nuclei and H_{e} is the Hamiltonian for the electrons, including the electron-nuclei interaction.

The two Hamiltonians have a similar structure. The nuclear Hamiltonian is given by

$$\hat{H}_{\mathrm{N}} = -\frac{\hbar^2}{2}\sum_{j}^{N_N}\frac{\nabla^2_{\boldsymbol{R}_j}}{M_j} + \sum_{j<k}^{N_N}\frac{Z_j Z_k}{|\mathbf{R}_j - \mathbf{R}_k|}, \tag{2.2}$$

with the first term being the sum of the kinetic energy for each nucleus j of mass M_j at position $\mathbf{R}_j$, while the second term is the sum of Coulombic interactions between nucleus j and k of charge Z_j and Z_k.

The electron Hamiltonian is given by

$$\hat{H}_{\mathrm{e}} = -\frac{\hbar^2}{2}\sum_{i}^{N_e}\nabla^2_{\boldsymbol{r}_i} + \sum_{i,j;\,i<j}^{N_e}\frac{1}{|\boldsymbol{r}_i - \boldsymbol{r}_j|} + \sum_{i,j}^{N_e,N_N}\frac{Z_j}{|\boldsymbol{r}_i - \boldsymbol{R}_j|}, \tag{2.3}$$

where the first term is the sum of the kinetic energy for each electron i at position $\mathbf{r}_i$, the second term is the sum of the Coulomb repulsion between electrons i and j and the third term is the sum of the Coulomb attraction between electron i and nucleus j.

To render this complex problem more tractable, most computational methods rely on the Born-Oppenheimer (BO) approximation [66]. This assumption posits that, due to their significantly greater inertial mass, nuclei respond much slower than electrons. Thus we shall in the proceeding discussion decouple the electronic and nuclear components, and solve for the electronic structure for a given 'frozen' nuclear configuration. That means the nuclear Hamiltonian $\hat{H}_{\mathrm{N}}$ is treated as a constant $E_{NN} = \langle \hat{H}_N \rangle$ when studying fixed atom configurations. Forces from that term are computed and handled separately in a DFT-based structural relaxation stages. In effect, we work with an external potential acting on the electrons [65, 67]:

$$\hat{V}_{\mathrm{ext}}(\mathbf{r}) \equiv \sum_{i}^{N_e}\hat{v}_{\mathrm{ext}}(\mathbf{r}_i) = \sum_{i,j}^{N_e,N_N}\frac{Z_j}{|\boldsymbol{r}_i - \boldsymbol{R}_j|} - V_0 \tag{2.4}$$

and adjust V_0 to avoid a divergence in the expectation values for $\hat{V}_{\mathrm{ext}}(\mathbf{r}) + \hat{V}_{\mathrm{ee}}$ for periodic systems [65]. This is important also for molecules when treated in plane-wave codes.

To summarize the BO approximation, we treat the effective electron Hamiltonian:

$$\hat{H} = \hat{T} + \hat{V}_{\mathrm{ext}} + \hat{V}_{\mathrm{ee}}, \tag{2.5}$$

where kinetic energy is described by,

$$\hat{T} = -\frac{\hbar^2}{2}\sum_{i}^{N_e}\nabla^2_{\boldsymbol{r}_i}, \tag{2.6}$$

and the electron-electron interaction is given by

$$\hat{V}_{\mathrm{ee}} \equiv \sum_{i,j;\,i<j}^{N_e}\hat{v}_{\mathrm{ee}}(\mathbf{r}_i, \mathbf{r}_j), = \sum_{i,j;\,i<j}^{N_e}\frac{1}{|\boldsymbol{r}_i - \boldsymbol{r}_j|}. \tag{2.7}$$

Despite these simplifications, the electronic Hamiltonian remains a daunting many-body problem. The ground-state wavefunction $\Psi(\{\mathbf{r}_i\})$ will depend on $3N_e$ spatial and

N_e spin variables. It must also adhere to the Pauli exclusion principle, exhibiting anti-symmetry under the exchange of any two electrons. This requirement results in a wave-function with $N_e(N_e-1)$ nodal planes in a $3N_e^2$-dimensional space, forming a complicated topological object.

The total energy of the system can be expressed in terms of density matrices. We introduce $\mathbf{r} = (\mathbf{x}, \sigma)$ as shorthand for the spatial and spin variables, and the summation over the spin variables is implicit. We can then express the electron density matrix in coordinate representation as [67]

$$\gamma(\{\mathbf{r_i}\};\{\mathbf{r_i'}\}) = \Psi^*(\{\mathbf{r_i}\})\Psi(\{\mathbf{r_i'}\}), \tag{2.8}$$

and define one and two-particle density matrices $\gamma_1(\mathbf{r},\mathbf{r}')$ and $\gamma_2(\mathbf{r},\mathbf{r}')$:

$$\gamma_1(\mathbf{r}_1,\mathbf{r}_1') = N_e \int d\mathbf{r}_2 \dots d\mathbf{r}_{N_e}\, \Psi^*(\mathbf{r}_1,\mathbf{r}_2,\dots,\mathbf{r}_{N_e})\Psi(\mathbf{r}_1',\mathbf{r}_2,\dots,\mathbf{r}_{N_e}), \tag{2.9}$$

$$\gamma_2(\mathbf{r}_1,\mathbf{r}_2;\mathbf{r}_1',\mathbf{r}_2') = \frac{N_e(N_e-1)}{2} \int d\mathbf{r}_3 \dots d\mathbf{r}_{N_e}\, \Psi^*(\mathbf{r}_1,\mathbf{r}_2,\dots,\mathbf{r}_{N_e})\Psi(\mathbf{r}_1',\mathbf{r}_2',\dots,\mathbf{r}_{N_e}). \tag{2.10}$$

The introduction of these restricted density matrices allows us to rewrite the ground-state energy $E = \langle H \rangle$ as

$$E = -\frac{1}{2}\int_{\mathbf{r}} \left[\nabla^2 \gamma_1\left(\mathbf{r},\mathbf{r}'\right)\right]_{\mathbf{r}=\mathbf{r}'} + \int_{\mathbf{r}} \gamma_1(\mathbf{r},\mathbf{r})\hat{v}_{\text{ext}}(\mathbf{r}) + \frac{1}{2}\int_{\mathbf{r}}\int_{\mathbf{r}'} \frac{\gamma_2\left(\mathbf{r},\mathbf{r}';\mathbf{r},\mathbf{r}'\right)}{|\mathbf{r}-\mathbf{r}'|}. \tag{2.11}$$

where

$$T[\gamma_1] = -\frac{1}{2}\int_{\mathbf{r}} \left[\nabla^2 \gamma_1\left(\mathbf{r},\mathbf{r}'\right)\right]_{\mathbf{r}=\mathbf{r}'}, \tag{2.12}$$

$$E_{\text{ext}}[\gamma_1, v] = \int_{\mathbf{r}} \gamma_1(\mathbf{r},\mathbf{r}) v_{\text{ext}}\left(\mathbf{r}\right), \tag{2.13}$$

$$E_{\text{ee}}[\gamma_2] = \frac{1}{2}\int_{\mathbf{r}}\int_{\mathbf{r}'} \gamma_2\left(\mathbf{r},\mathbf{r}';\mathbf{r},\mathbf{r}'\right)\hat{v}_{\text{ee}}(\mathbf{r},\mathbf{r}'). \tag{2.14}$$

$$\tag{2.15}$$

denotes the kinetic energy functional, the external potential energy functional, and the Coulomb energy functional, respectively [54]. In Eq. (2.11), and through the rest of the thesis, a subscript '$\mathbf{r}$' implies a complete spatial integration.

The exact wavefunction solution can in principle always be obtained by diagonalization of the Hamiltonian via a variational principle, a technique known as Full Configuration Interaction (FCI) [68–71]. In chemistry, FCI is revered for providing, in principle, exact solutions for reference calculations where feasible. However, its applicability is generally limited to systems with a small number of electrons, where the practical limit is around the size of a Benzene molecule [72]. This limit stems partly from the memory complexity of FCI which is extreme due to the dimensionality and incurs the need for a large orbital basis sets. Additionally there is highly demanding computational complexity, that for FCI scales by the factorial of the number of electrons ($\mathcal{O}(N_e!)$). It is not a viable option for complex soft matter systems where the number of electrons is at least in the order of 10^2 [67, 73, 74].

2.1.2 Density Formulation

All we have done so far is to rewrite the Hamiltonian in terms of the electron density matrices. An idea pioneered by Thomas [75], Fermi [76], Dirac [77], and others in the in 1930s, is that we can compute the total energy from just the diagonal of the one-particle density matrix

$$n(\mathbf{r}) = \gamma_1(\mathbf{r}, \mathbf{r}). \tag{2.16}$$

The central theorems of DFT, published by Hohenberg and Kohn validate the idea, proving that the ground-state energy of a system is a unique functional of the electron density $n(\mathbf{r})$. These deceptively simple theorems [54] provide a means to determine the ground state energy of a system through its electron density alone, integrating out the need for the many-body wavefunction. This is an enormous simplification, as the electron density is a function of just three spatial variables, regardless of the number of electrons, in contrast to the wavefunction which, as mentioned above, depends on $3N_e$ spatial variables for N_e electrons. The simplification is possible because the ground-state energy of the system can be expressed as a functional of the electron density:

$$E[n] = F[n] + E_{\text{ext}}[n, v_{\text{ext}}]. \tag{2.17}$$

Here $F[n]$ and $E[n]$ are strictly independent of v_{ext}, because v_{ext} is itself a functional of n [54]. The functional $F[n]$ contains all the internal energies of the interacting electron system. It is a functional of the electron density that keeps $T[\gamma_1]$ and $E_{\text{e-e}}[\gamma_2]$ together [54, 55].

At the same time, the theorems guarantee the existence of the energy functional $F[n]$, but they do not specify its exact form. Still the ingenuity of the theorems lies in the fact that approximating the density (and the energy density functional $E[n]$) is a much simpler task than approximating the complicated many-body wavefunction $\Psi(\{\mathbf{r}_i\})$. Furthermore, the $F[n]$ functional is universal, that is independent of the system. $F[n]$ is a perfect tool in the sense that if we fabricate a good approximation once, we can use it forever. We strive to also make such designs useful. The proof is then in the pudding: we try to use it for many different types of materials problems, and ideally we may then see it validated as a general purpose approach.

2.1.3 The Kohn-Sham System: Independent Particles

With the follow-up work of Kohn and Sham in 1965 [55], density functional theory was taken from a theoretical concept to a practical computational tool. The Kohn-Sham (KS) scheme is a way to reformulate the search for the ground-state density $n(r)$ into a search for KS single-particle orbitals $\psi_k(\mathbf{r})$ of a system of neutral particles (fictitious non-interacting electrons) that move in an effective potential, producing the same ground-state particle density as the real system of interacting electrons. In this orbital basis the one-particle density matrix is

$$\gamma_{\text{KS}}(\mathbf{r}, \mathbf{r}') \equiv \sum_{k=1}^{N_e} \psi_k(\mathbf{r}) \psi_k^*(\mathbf{r}'). \tag{2.18}$$

With a correct effective potential, the KS description will result in a determination of the true density

$$n(\mathbf{r}) = \gamma_{\text{KS}}(\mathbf{r}, \mathbf{r}'), \tag{2.19}$$

and a simple evaluations of the non-interacting kinetic energy functional,

$$T_{\mathrm{KS}}[n] = \lim_{\mathbf{r}'\to\mathbf{r}} -\frac{1}{2}\int d^3r \left[\nabla^2 \gamma_{\mathrm{KS}}\left(\mathbf{r},\mathbf{r}'\right)\right]. \tag{2.20}$$

More broadly, Eq. (2.20) permits us to complete a full DFT calculation as if it concerns independent particles moving in an effective potential $V_{\mathrm{eff}}(\mathbf{r})$ that produce all energy contributions, and that is also given by Eq. (2.19).

The full electron-electron energy should be close to the the Hartree energy $E_{\mathrm{H}}[n]$, that is the mean-field Coulomb energy of the non-interacting system,

$$E_{\mathrm{H}}[n] = \frac{1}{2}\int_{\mathbf{r}}\int_{\mathbf{r}'} \frac{n(\mathbf{r})n(\mathbf{r}')}{|\mathbf{r}-\mathbf{r}'|}, \tag{2.21}$$

This is always a dominant part of $\langle \hat{V}_{\mathrm{ee}}\rangle$. The total KS energy functional is given by:

$$E_{\mathrm{KS}}[n] = T_{\mathrm{KS}}[n] + E_{\mathrm{H}}[n] + E_{\mathrm{ext}}[n,v] + E_{\mathrm{xc}}[n], \tag{2.22}$$

where the XC energy functional $E_{\mathrm{xc}}[n]$ contains all the remaining terms in the true energy functional $E[n]$ of the fully interacting system [65, 78]. This XC functional is the difference in kinetic energy due to the correlated motion of the fully interacting electrons and the non-interacting electrons in the KS system, together with the difference in the Coulomb energy of the same two systems:

$$E_{\mathrm{xc}}[n] = T[\gamma_1] - T_{\mathrm{KS}}[n] + E_{\mathrm{ee}}[\gamma_2] - E_{\mathrm{H}}[n] = \langle \hat{T}\rangle - \hat{T}_{\mathrm{KS}}[n] + \langle \hat{V}_{\mathrm{ee}}\rangle - E_{\mathrm{H}}[n]. \tag{2.23}$$

2.2 Adiabatic Connection Formula and Holes

An important step in the development of transferable and accurate XC-functionals for practical (efficient) DFT came with the use of the adiabatic connection formula. It was proposed independently by Gunnarsson and Lundqvist in 1976 [56] and by Langreth and Perdew in 1975 [79] and 1977 [57]. They realized that the exchange-correlation energy E_{xc} can be expressed using an idea from formal many particle perturbation theory (MBPT). In essence, the electronic charge is varied from zero (the noninteracting case) to the actual value with the added constraint that the density must be kept constant during this variation. Mathematically, the procedure is a coupling constant integration, where the coupling constant, $0 \le \lambda \le 1$, is introduced in the Hamiltonian as a scaling factor for the electron-electron interaction.

The XC functional can be related to the system's response to external perturbations through the fluctuation-dissipation theorem (FDT). This relation involves the many-body linear response function $\chi_\lambda(\mathbf{r},\mathbf{r}';\omega)$, which describes how the electron density at point $\mathbf{r}$ responds to a small, frequency-dependent external potential $\delta\Phi^{\omega}_{\mathrm{ext}}(\mathbf{r}')$ applied at point $\mathbf{r}'$, again characterized as a function of the assumed coupling constant λ. The density response of the system to this external potential, in the linear regime, is given by

$$\delta n^{\omega}_{\lambda}(\mathbf{r}) = \int_{\mathbf{r}'} \chi\left(\mathbf{r},\mathbf{r}';\omega\right)\delta\Phi^{\omega}_{\mathrm{ext}}\left(\mathbf{r}'\right), \tag{2.24}$$

where $\chi_\lambda\left(\mathbf{r},\mathbf{r}';\omega\right) = \delta n^{\omega}_{\lambda}(\mathbf{r})/\delta\Phi^{\omega}_{\mathrm{ext}}\left(\mathbf{r}'\right)$ can be expressed via MBPT [80]. As the electronic system responds to the external field, it uncovers the underlying interactions within the

system. Through the FDT this response is related to XC functional by [56, 57, 79–81]:

$$E_{\mathrm{xc}} = -\int_0^1 \mathrm{d}\lambda \int_0^\infty \frac{\mathrm{d}u}{2\pi} \int_{\mathbf{r}} \int_{\mathbf{r}'} \frac{\chi_\lambda(iu, \mathbf{r}, \mathbf{r}')}{|\boldsymbol{r} - \boldsymbol{r}'|} - E_{\mathrm{self}}, \tag{2.25}$$

$$= -\int_0^1 \mathrm{d}\lambda \int_0^\infty \frac{\mathrm{d}u}{2\pi} \mathrm{Tr}\{\chi_\lambda(iu)V\} - E_{\mathrm{self}}, \tag{2.26}$$

where we have suppressed the spatial dependence in the last line for clarity. In this formulation, $V = |\boldsymbol{r} - \boldsymbol{r}'|^{-1}$ represents the matrix element of the electron-electron interaction operator $\hat{V}_{\mathrm{ee}}$. The term E_{self} accounts for the self-interaction energy, which is the energy an electron would have interacting with itself [80]:

$$E_{\mathrm{self}} = \mathrm{Tr}\{n(r)V(r - r')\delta(r - r')\}. \tag{2.27}$$

The integration in Eq. (2.26) is performed over the imaginary frequencies, picking up poles in the response function. These poles reflects both the single particle and the collective excitations that sets the dynamic response of the system. The trace of the product $\chi_\lambda V$ essentially measures the interaction energy between an electron and the induced changes in the electron density around it. This interaction energy, which includes both exchange and correlation effects, is commonly cast in terms of the XC hole $n_{\mathrm{xc}}(\mathbf{r}, \mathbf{r}')$ [57, 79],

$$n_{\mathrm{xc}}\left(\mathbf{r}; \mathbf{r}' - \mathbf{r}\right) = -\delta\left(\mathbf{r} - \mathbf{r}'\right) - \frac{2}{n(\mathbf{r})} \int_0^\infty \frac{\mathrm{d}u}{2\pi} \int_0^1 \mathrm{d}\lambda \chi_\lambda\left(\mathbf{r}, \mathbf{r}'; iu\right). \tag{2.28}$$

Specifically this hole captures the tendency of like-spin electrons to avoid each other (i.e. Pauli exclusion principle) and the tendency of opposite-spin (charged) electrons to also avoid each other (part of the correlation effects). The exchange-correlation energy can then be expressed as Hartee-like term [56]:

$$E_{\mathrm{xc}} = \frac{1}{2} \int_{\mathbf{r}} \int_{\mathbf{r}'} \frac{n(\mathbf{r}) n_{\mathrm{xc}}(\mathbf{r}, \mathbf{r}')}{|\mathbf{r} - \mathbf{r}'|}. \tag{2.29}$$

I note in passing that the exchange-correlation hole is an inherently non-local quantity, as it depends on the density at all points in space, and that it can be decomposed into an exchange hole and a correlation hole:

$$n_{\mathrm{xc}}(\mathbf{r}, \mathbf{r}') = n_{\mathrm{x}}(\mathbf{r}, \mathbf{r}') + n_{\mathrm{c}}(\mathbf{r}, \mathbf{r}'). \tag{2.30}$$

The charge-conservation sum rule ensures that the integral of the exchange-correlation hole equals -1, effectively accounting for the "removal" of one electron,

$$\int_{\mathbf{r}'} n_{\mathrm{xc}}(\mathbf{r}, \mathbf{r}') = -1. \tag{2.31}$$

In practice, we constrain our response description by two criteria:

$$\int_{\mathbf{r}'} n_{\mathrm{x}}(\mathbf{r}, \mathbf{r}') = -1 \quad \text{and} \quad \int_{\mathbf{r}'} n_{\mathrm{c}}(\mathbf{r}, \mathbf{r}') = 0. \tag{2.32}$$

Analysis and physics-based modeling of the xc-hole, is one of the primary approaches for design of the approximations for $E_{\mathrm{xc}}[n]$. The hole must satisfy a sum rule Eq. (2.32),

because the hole is there to screen out the charge of the electron — how else can we pretend to work with independent particles in the KS scheme? This charge-conservation rule as well as other constraints are used to design robust approximations for the exchange-correlation functional. For example, in CX (and inside the non-local correlation energy part, $E_c^{\rm nl}$, of all vdW-DFs) we enforce current conservation, a criterion that automatically ensures also the hole-charge conservation implied in Eq. (2.32) [42].

The exchange hole can be expressed in closed form using the KS density matrix

$$\tilde{n}_{\rm x}(\mathbf{r},\mathbf{r}') = -\frac{|\gamma_{KS}(\mathbf{r},\mathbf{r}')|^2}{n(\mathbf{r})}|_{\sigma=\sigma'} \tag{2.33}$$

giving the unscreened Fock-exchange energy [82]:

$$E_{\rm x}^{\rm Fock} = \frac{1}{2}\int_{\mathbf{r}}\int_{\mathbf{r}'}\frac{n(\mathbf{r})\tilde{n}_{\rm x}(\mathbf{r},\mathbf{r}')}{|\mathbf{r}-\mathbf{r}'|}. \tag{2.34}$$

However, this formulation cannot be used directly in a density functional. This is because it does not incorporate proper screening of the Coulomb interaction when approximating the shape of n_{xc} and hence when setting the details of E_{xc} via Eq. (2.29).

The exchange hole is also constrained by the behavior that emerges in the uniform or homogeneous electron gas (HEG) limit. In essence, the exchange hole should approach that of the HEG in the limit of a slowly varying density,

$$n_{\rm x}^{\rm HEG}(\boldsymbol{r},\boldsymbol{r'}) = n_{\rm x}^{\rm HEG}(\boldsymbol{r}-\boldsymbol{r'}) \tag{2.35}$$

For the HEG of density n_0, Slater [65] computed the exchange energy per particle;

$$\varepsilon_{\rm x}^{\rm HEG}[n_0] = -\frac{3}{4\pi}\left(\frac{3}{\pi}\right)^{1/3} n_0^{1/3}. \tag{2.36}$$

That result connects to the HEG exchange hole via:

$$\varepsilon_{\rm x}^{\rm HEG}[n_0] = \frac{1}{2}\int_{\mathbf{r}'}\frac{n_{\rm x}(\mathbf{r},\mathbf{r}')}{|\mathbf{r}-\mathbf{r}'|}, \tag{2.37}$$

When Eq. (2.37) is used for a study of an actual system (that has a spatial density variation $n(\mathbf{r})$) using the so-called local density approximation (LDA), we replace $\varepsilon_{\rm x}^{\rm HEG}[n_0]$ by $-\frac{3}{4\pi}k_F$ where k_F denotes the local value of Fermi vector $k_F(\mathbf{r}) \equiv (3\pi^2 n(\mathbf{r}))^{1/3}$.

One constraint is the Lieb-Oxford bound that establishes a lower bound on the XC energy,

$$E_{\rm x}[n] \geq E_{\rm xc}[n] \geq -1.68e^2\int d^3r\, n(\mathbf{r})^{4/3}. \tag{2.38}$$

Of relevance for a discussion of the vdW-DF designs we observe that the Lieb-Oxford bound is sometimes enforced at the local level but that is not an actual constraint. Instead Eq. (2.38) must hold on a molecular or unit cell level as discussed in **Paper B** (and we have provided code to check whether it does so in practice [49]).

The coming sections detail the vdW-DF method and specific XC-functional implementations. To that end we will discuss approximations for $\chi_\lambda(\mathbf{r},\mathbf{r}';\omega)$ that are used to construct the correlation holes for a truly non-local functional design like a vdW-DF. I also summarize how to construct RSHs based on the shape of the exchange hole. The

method treats the problem of designing an XC-functional approximation as an electrodynamics problem. Specifically we use the screened Lindhard dielectric function, $\kappa_\lambda(\omega)$, averaged over the interaction strength λ. In practice, in the framework of the vdW-DF method we work with the definition [83]

$$\ln\big(\kappa_{\mathrm{ACF}}(\omega)\big) \equiv -\int_0^1 \mathrm{d}\lambda V \chi_\lambda(\omega). \tag{2.39}$$

The function $\kappa_{\mathrm{ACF}}(\mathbf{r},\mathbf{r}';\omega)$ represents an effective non-local dielectric function, as defined by the formally exact adiabatic connection fluctuation-dissipation (ACF) theorem and the XC-hole definition. It allows us to provide an exact rewrite of the exchange-correlation energy

$$E_{\mathrm{xc}} = \int_0^\infty \frac{\mathrm{d}u}{2\pi}\,\mathrm{Tr}\left\{\ln\big(\kappa_{\mathrm{ACF}}(\mathrm{i}u)\big)\right\} - E_{\mathrm{self}}. \tag{2.40}$$

Since $\kappa_{\mathrm{ACF}}(\omega)$ must obey the f-sum rule [83, 84], representing the longitudinal component of the electrodynamic response, we write

$$\kappa_{\mathrm{ACF}}(\omega) = \nabla\cdot\epsilon(iu)\cdot\nabla G. \tag{2.41}$$

Here G is the Coloumb Green's functions and $\varepsilon(\omega)$ is a dielectric function that corresponds to some simpler 'input', or approximation to the the electrodynamical screening in the electron gas. In summary, we can express the XC energy succinctly as

$$E_{\mathrm{xc}} = \int_0^\infty \frac{\mathrm{d}u}{2\pi}\,\mathrm{Tr}\{\ln\big(\nabla\epsilon(iu)\nabla G\big)\} - E_{\mathrm{self}}\,. \tag{2.42}$$

The trick of the vdW-DF method, detailed below, is to set $\varepsilon(\omega)$ as corresponding to a simpler, trusted (semilocal) approximation for E_{xc} i.e. the so-called internal (GGA type) functional [6, 83]

$$E_{\mathrm{xc}}^{\mathrm{in}} = \int_0^\infty \frac{\mathrm{d}u}{2\pi}\,\mathrm{Tr}\{\ln\big(\epsilon(iu)\big)\} - E_{\mathrm{self}}\,. \tag{2.43}$$

We note that both Eq. (2.42) and (2.43) have poles when the dielectric function ($\varepsilon(\omega)$ or $\kappa_{\mathrm{ACF}}(\omega)$) equals zero. Such excitations of the electron systems are called plasmons.

2.3 Functional approximations

The first conceived and simplest approximation for the exchange-correlation functional is the LDA, which today serves as the foundation for more complex functional forms [56, 85, 86]. The LDA assumes that the exchange-correlation energy per electron can be approximated by the value it would have in a uniform electron gas [55]:

$$E_{\mathrm{xc}}^{\mathrm{LDA}} = \int_{\mathbf{r}} n(\mathbf{r})\,\varepsilon_{\mathrm{xc}}^{\mathrm{HEG}}(n(\mathbf{r})), \tag{2.44}$$

LDA is successful in describing systems where the electron density varies slowly, providing an acceptable approximation for some materials [87]. However, its accuracy and consistency diminishes for systems with important variations in electron density, for example in molecules [88, 89]. This problem motivated the development of the generalized gradient approximations (GGAs) and eventually also the vdW-DFs.

Semi-local functionals in the GGA form, are an extension of LDA. In practice it implies that the LDA exchange energy per particle $\varepsilon_{\mathrm{x}}^{\mathrm{HEG}}(n(\mathbf{r}))$ is enhanced by a factor;

$$f_{\mathrm{xc}}\left(n(\mathbf{r}), s(\mathbf{r})\right) = f_{\mathrm{c}}^{\mathrm{GGA}}\left(n(\mathbf{r}), s(\mathbf{r})\right) + f_{\mathrm{x}}^{\mathrm{GGA}}\left(s(\mathbf{r})\right), \tag{2.45}$$

$$E_{\mathrm{xc}}^{\mathrm{GGA}} \equiv \int_{\mathbf{r}} n(\mathbf{r})\, \varepsilon_{\mathrm{x}}^{\mathrm{HEG}}(n(\mathbf{r}))\, f_{\mathrm{xc}}\left(n(\mathbf{r}), s(\mathbf{r})\right). \tag{2.46}$$

The enhancement depends on the density and on the reduced density gradient $s(\mathbf{r})$ [41]:

$$s(\mathbf{r}) \equiv \frac{\left|\nabla n(\mathbf{r})\right|}{2k_{\mathrm{F}} n(\mathbf{r})}. \tag{2.47}$$

In Fig. 2.1 we show the dependency of the enhancement factor $f_{\mathrm{x}}^{\mathrm{GGA}}(s)$ on the reduced density gradients for the set of GGA-exchange components for vdW-DF versions that are relevant to this thesis. We also show the enhancement factors that characterize the exchange in the popular GGA functionals PBE [41] and PBEsol [90].

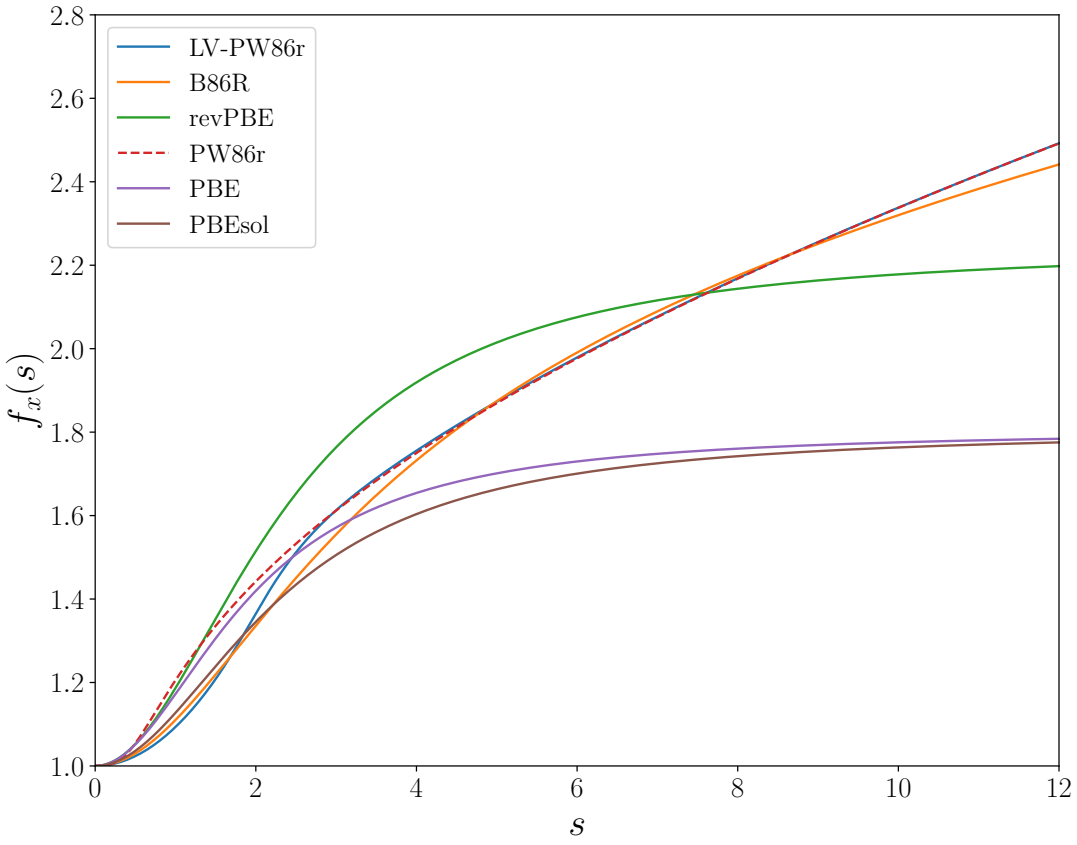

Figure 2.1: Comparative plot of the exchange enhancement factor $f_x(s)$ as a function of the reduced density gradient s, where 0 corresponds to the homogeneous electron gas, for various GGA exchange functionals. The enhancement factors for LV-PW86r (or cx13), B86R, revPBE, and PW86r [91] functionals are shown; these are used inside the vdW-DF-cx [42], vdW-DF2-B86r [92], vdW-DF1 [84], and vdW-DF2 [93] functionals, respectively. For comparison we also show the enhancement factor that characterize exchange in the popular GGAs PBE [41] and PBEsol [94].

The dependence on the density gradient allows GGAs to better reflect the impact of inhomogeneities in the electron gas, leading to improved results, when compared to

LDA [26, 87, 88], for bulk structure [95, 96], and for surface properties that are sensitive to the details of the electron distribution, e.g. Refs. [89, 97–101]

With our discussion of the GGAs, we have simultaneously [47, 59, 100] set the stage to introduce the vdW-DFs, as decomposed into two components:

$$E_{\rm xc}^{\rm vdW-DF} = E_{\rm xc}^{0} + E_{\rm c}^{\rm nl}. \tag{2.48}$$

Here $E_{\rm xc}^{0} = E_{\rm xc}^{\rm in} + \delta E_{\rm x}^{0}$ contains the actual exchange description. $E_{\rm xc}^{0}$ is also nearly the above mentioned internal GGA type functional $E_{\rm xc}^{\rm in}$ [100, 102] that is taken as input for defining the truly nonlocal-correlation term $E_{\rm c}^{\rm nl}$. Specifically, by working with $E_{\rm xc}^{\rm in}$ we obtain a paramterization of the plasmon dispersion that sets the form of $\varepsilon(\omega)$ and an in turn set the net functional behaviour via Eq. (2.43). The actual exchange of a given vdW-DF ($E_{\rm xc}^{0}$), also contains a cross over exchange-only term $\delta E_{\rm x}^{0}$ that permits us to recoup some (exchange) energy that is lost when we pick a simple approximation for the input dielectric function $\varepsilon(\omega)$ [83, 103, 104].

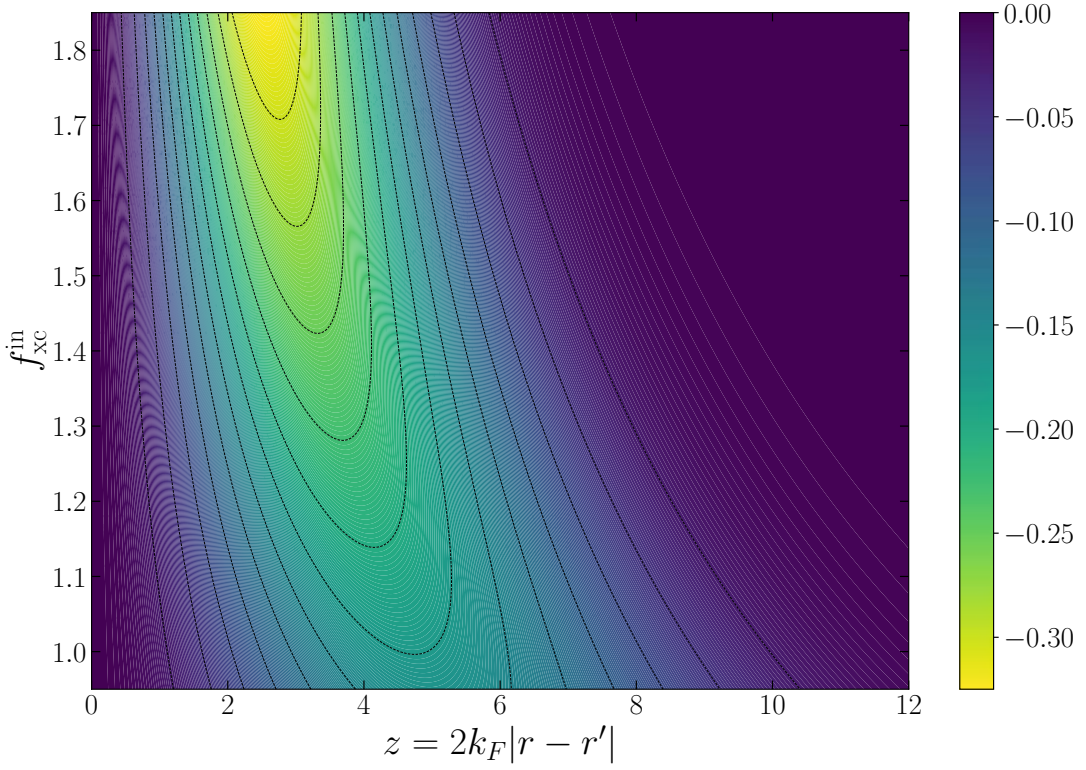

Figure 2.2: Contour plot of the vdW-DF internal functional xc hole $\bar{n}_{\rm xc}^{\rm in}$, spatially weighted and scaled. The hole is mapped as a function of scaled separation $z = 2k_F\,|\mathbf{r}' - \mathbf{r}|$ and the characteristic internal functional enhancement factor $f(\mathbf{r}) = f_{\rm xc}^{\rm in}(\mathbf{r}) = q_0[n](\mathbf{r})/k_F[n](\mathbf{r})$, which is fixed for a given density $n(\mathbf{r})$ and a given scaled density gradient $s = |\nabla n|/\,(2k_{\rm F}n)$. Contour spacing is 0.025.

In the vdW-DF design, the internal functional is given by the LDA-correlation term - given by $f_{\rm c}^{\rm LDA}(n)$ and an exchange-gradient enhancement $f_{\rm x}^{\rm in}(s)$ [84, 105]:

$$f_{\rm xc}^{\rm in}(n,s) = f_{\rm c}^{\rm LDA}(n) + f_{\rm x}^{\rm in}(s). \tag{2.49}$$

The form is similar to Eq. (2.45) but we deliberately restrict correlation to the LDA level to avoid double counting: we include all beyond-LDA correlation in the non-local term

$E_{\rm c}^{\rm nl}$ that is characteristic of the vdW-DF method. With Eq. (2.49), the internal semi-local exchange-correlation energy is defined as [105]:

$$\begin{aligned} E_{\rm xc}^{\rm in} &= \int_{\mathbf{r}} n(\mathbf{r})\varepsilon_{\rm xc}^{\rm in}(\mathbf{r}) = \int_{\mathbf{r}} n(\mathbf{r})\varepsilon_{\rm x}^{\rm HEG}(\mathbf{r}) f_{\rm xc}^{\rm in}(n,s) \\ &= \frac{1}{2}\int_{\mathbf{r}} \frac{n(\mathbf{r})n_{\rm xc}^{\rm in}(\mathbf{r},\mathbf{r}')}{|\mathbf{r}-\mathbf{r}'|} \end{aligned} \tag{2.50}$$

The internal energy-per-particle $\varepsilon_{\rm xc}^{\rm int}(\mathbf{r})$ is used to formulate the respective internal exchange-correlation hole $n_{xc}^{\rm in}(\mathbf{r})$,

$$\bar{n}_{\rm xc}^{\rm in}(\mathbf{r},q) = -\exp\left[-\gamma\left(q/q_0(\mathbf{r})\right)^2\right]. \tag{2.51}$$

Here $q_0(\mathbf{r})$ is the inverse screening length for the hole.The parameter γ is arbitrary — that is, changing it's value has no effect on $E_c^{\rm nl}$. Picking $\gamma = 4\pi/9$ gives a simple relation for $q_0(\mathbf{r})$,

$$q_0[n](\mathbf{r}) = k_{\rm F}[n](\mathbf{r}) f_{\rm xc}^{\rm in}[n](\mathbf{r}). \tag{2.52}$$

A plot of the scaled internal xc-hole $n_{\rm xc}^{\rm in}$, as used to represent $E_{\rm c}^{\rm nl}$ in vdW-DFs, can be seen in Figure 2.2, giving the dependence of $n_{\rm xc}^{\rm in}$ of both $|\mathbf{r}-\mathbf{r}'|$ and the magnitude of the local $f_{\rm xc}^{\rm in}$ value.

The choice of internal functional description gives us the input $\varepsilon(\mathbf{r},\mathbf{r}';\omega)$ via Eq. (2.43) and we can express the non-local correlation energy [89]:

$$E_{\rm c}^{\rm nl} = E_{\rm xc}^{\rm vdW-DF} - E_{\rm xc}^{0} = \int_0^\infty \frac{{\rm d}u}{2\pi}\,{\rm Tr}\{\ln\big(\nabla\epsilon(iu)\nabla G\big) - \ln\big(\epsilon(iu)\big)\}. \tag{2.53}$$

In practice, we rely on an exponential resummation of the dielectric function, we use a form that can be expressed in terms of the plasmon propagator $S_{\rm xc}(iu)$ as [100]:

$$\epsilon(iu) = e^{S_{\rm xc}(iu)}. \tag{2.54}$$

That is, the plasmon poles of $S_{\rm xc}(iu)$ are parameterised by connecting the dielectric function to the internal functional [84, 105],

$$E_{\rm xc}^{\rm int} = \int_0^\infty \frac{{\rm d}u}{2\pi}\,{\rm Tr}\left\{S_{\rm xc}\right\} - E_{\rm self} = \int_{\mathbf{r}} n(\mathbf{r})\,\varepsilon_{\rm xc}^{\rm int}(\mathbf{r}), \tag{2.55}$$

The plasmon propagator is modeled as [106]

$$S_{\rm xc}(\omega) \equiv \frac{1}{2}\left[S_{\rm xc}(\omega,\mathbf{q},\mathbf{q}') + S_{\rm xc}(-\omega,\mathbf{q},\mathbf{q}')\right], \tag{2.56}$$

which in Fourier space is given by [84]

$$S_{\rm xc}\left(\omega,\mathbf{q}',\mathbf{q}\right) = \int_{\mathbf{r}} {\rm e}^{{\rm i}(\mathbf{q}-\mathbf{q}')\cdot\mathbf{r}} \frac{\omega_{\rm p}^2(\mathbf{r})}{\left[\omega+\omega_{\mathbf{q}}(\mathbf{r})\right]\left[-\omega+\omega_{\mathbf{q}'}(\mathbf{r})\right]}. \tag{2.57}$$

Here

$$\omega_{\rm p}^2(\mathbf{r}) = 4\pi\, n(\mathbf{r}), \tag{2.58}$$

is the classical plasma frequency and we describe the plasmon dispersion via

$$\omega_q(\mathbf{r}) = \frac{q^2}{2}\frac{1}{h\left(q/q_0\right)} \quad ; \quad h(x) = 1-\exp\left(-4\pi/9\cdot x^2\right). \tag{2.59}$$

To arrive at a computationally tractable non-local correlation functional [84, 102, 105], we also expand to second order in the plasmon propagator

$$E_c^{\mathrm{nl}} = \int_0^\infty \frac{du}{4\pi} \mathrm{Tr}\left[S_{\mathrm{xc}}(iu)^2 - \left(\nabla S_{\mathrm{xc}}(iu)\cdot\nabla G\right)^2\right] \tag{2.60}$$

$$= \int_0^\infty \frac{\mathrm{d}u}{4\pi} \sum_{\mathbf{q},\mathbf{q}'} \left(1 - \left(\hat{\mathbf{q}}\cdot\hat{\mathbf{q}}'\right)^2\right) S_{\mathrm{xc}}\left(iu,\mathbf{q},\mathbf{q}'\right) S_{\mathrm{xc}}\left(iu,\mathbf{q}',\mathbf{q}\right); \tag{2.61}$$

Refs. [83, 100, 104] details the nature of all higher order terms. The non-local internals can now be handled once and for all in a universal vdW-DF correlation kernel ϕ. This, in turn, mean that we write the non-local correlation energy in the now popular form [28, 102, 107]:

$$E_{\mathrm{c}}^{\mathrm{nl}} = \frac{1}{2}\int_{\mathbf{r}}\int_{\mathbf{r}'} n(\mathbf{r})\,\phi\left(|\mathbf{r}-\mathbf{r}'|; n(\mathbf{r}), n\left(\mathbf{r}'\right), s(\mathbf{r}), s\left(\mathbf{r}'\right)\right)\, n\left(\mathbf{r}'\right), \tag{2.62}$$

The distinction among the major van der Waals density functional version releases, vdW-DF1/vdw-DF-cx and vdW-DF2/vdW-DF2-B86r, hinges on the choice of the internal GGA exchange enhancement factor, $f_{\mathrm{x}}^{\mathrm{in}}(s)$ and on the corresponding enhancement factor $f_{\mathrm{x}}^{0}(s)$ for the actual exchange (expressed in $E_{\mathrm{xc}}^{0} = E_{\mathrm{xc}}^{\mathrm{in}} + \delta E_{\mathrm{x}}^{0}$). The nature of $f_{\mathrm{c}}(n) + f_{\mathrm{x}}^{\mathrm{in}}(s)$ is the defining factor in the non-local correlation energy $E_{\mathrm{c}}^{\mathrm{nl}}$.

In this thesis, we have primarily used the consistent-exchange vdW-DF-cx version and it's extension to a RSH, vdW-DF-ahcx. In these functionals, the internal exchange enhancement is defined by merging aspects of the Langreth-Vosko approach with the revised Perdew-Wang 86 formulation. The exchange enhancement factor, $f_{\mathrm{x}}^{0}(s) = f_x^{\mathrm{CX}}(s)$, for CX is given by [42]:

$$f_x^{\mathrm{LV}}(s) = \left[1 + \mu_{\mathrm{LV}} s^2\right], \tag{2.63}$$

$$f_x^{\mathrm{PW86r}}(s) = \left(1 + as^2 + bs^4 + cs^6\right)^{1/15}, \tag{2.64}$$

$$f_x^{\mathrm{CX}}(s) = \left(\frac{1}{1+\alpha s^6}\right) f_x^{\mathrm{LV}}(s) + \left(\frac{\alpha s^6}{\beta + \alpha s^6}\right) f_x^{\mathrm{PW86r}}(s), \tag{2.65}$$

where $\mu_{\mathrm{LV}} = -Z_{\mathrm{ab}}/9$ and $Z_{\mathrm{ab}} = -0.8491$, together with $\alpha = 0.02178$ and $\beta = 1.15$. Specifically, within the regime where the reduced gradient is less than approximately 2.5 — a domain that is sufficient to represent binding in bulk, and in most molecular systems [42, 47, 49] — the enhancement factor closely mirrors the Langreth-Vosko screened exchange profile in Eq. (2.63). The $f_x^{\mathrm{CX}}(s)$ transitions smoothly to adopt the characteristics of the revised Perdew-Wang-86 form, Eq. (2.64), for s-values beyond this threshold in the CX design.

The rationale for taking the high-s limit from the PW86r form is to enforce charge conservation in the original and simplest possible interpretation of many-body perturbation theory (MBPT) input for $n_{\mathrm{x}}(\mathbf{r},\mathbf{r}')$ [100]. That framework was later adjusted to make the hole less deep, forming modern GGAs such as PBE. In any case, the coefficients α and β of Eq. (2.65) are determined by a least-squares fit for a smooth transition between the two regimes [42]. The complete implicit functional form is

$$E_{\mathrm{x}}^{\mathrm{CX}} = \int_{\mathbf{r}} n(\mathbf{r})\varepsilon_{\mathrm{x}}^{\mathrm{HEG}}(\mathbf{r}) f_{\mathrm{x}}^{\mathrm{CX}}(s), \tag{2.66}$$

$$E_{\mathrm{xc}}^{\mathrm{vdW-DF-cx}} = E_{\mathrm{x}}^{\mathrm{CX}} + E_{\mathrm{c}}^{\mathrm{LDA}} + E_{\mathrm{c}}^{\mathrm{nl}}. \tag{2.67}$$

The reason CX is called a consistent-exchange vdW-DF [6, 42, 100] is that there is alignment between the inner and actual exchange whenever the binding is saturated by s-value contributions up to the $s \sim 2.5$ threshold [42]. This often holds, but transition-state problems do challenge this implicit criterion for the CX design logic [42, 49].

In our work we have also used the vdW-DF2-B86r and the recently developed the RSH form thereof, called vdW-DF2-ahbr. The B86r internal exchange enhancement factor is constructed from the revised Becke 86 (B86b) form that is also based on a MBPT expansion, using a slightly different sorting of the diagrams, setting a scaled small-s expansion coefficient $\mu_{\mathrm{GEA}} = 10/81$. Moreover, there is an additional condition on the high-s behaviour resulting in the form [108]:

$$f_{\mathrm{x}}^{\mathrm{B86R}}(s) = 1 + \frac{\mu_{\mathrm{GEA}} s^2}{\left(1 + \mu_{\mathrm{GEA}} s^2/\kappa\right)^{4/5}}. \tag{2.68}$$

The resulting functional form is

$$E_{\mathrm{xc}}^{\mathrm{vdW-DF2-B86r}} = E_{\mathrm{x}}^{\mathrm{B86r}} + E_{\mathrm{c}}^{\mathrm{LDA}} + E_{\mathrm{c}}^{\mathrm{nl}}. \tag{2.69}$$

Since we've also utilized the vdW-DF1 and vdW-DF2 in our benchmark, we state also their forms here for completeness. The vdW-DF1 is built with the exchange of the revPBE [109] GGA:

$$E_{\mathrm{xc}}^{\mathrm{vdW-DF1}} = E_{\mathrm{x}}^{\mathrm{revPBE}} + E_{\mathrm{c}}^{\mathrm{LDA}} + E_{\mathrm{c}}^{\mathrm{nl}}, \tag{2.70}$$

while vdW-DF2 is built with PW86r [86, 91] exchange:

$$E_{\mathrm{xc}}^{\mathrm{vdW-DF2}} = E_{\mathrm{x}}^{\mathrm{PW86r}} + E_{\mathrm{c}}^{\mathrm{LDA}} + E_{\mathrm{c}}^{\mathrm{nl}}. \tag{2.71}$$

2.4 Spin formulation of vdW-DF method

Incorporating spin effects into the vdW-DF framework, termed svdW-DF framework necessitates modifications to both the semilocal and non-local components of the exchange-correlation energy. This adaptation enables the accurate description of spin-polarized systems, where the spin interactions significantly affect the electronic structure and properties, broadening the scope of materials that can be accurately studied to include for example magnetic and metallic systems.

The semilocal exchange part E_{xc}^0 of the vdW-DF is extended to account for spin polarization through the exact spin scaling of exchange, formulated as

$$E_x[n_\uparrow, n_\downarrow] = \frac{E_x[2n_\uparrow]}{2} + \frac{E_x[2n_\downarrow]}{2}. \tag{2.72}$$

This spin-scaling relation sets the impact of working with general spin densities $n_\uparrow$ and $n_\downarrow$ for spin-up and spin-down electrons, respectively, on the exchange energy description. Additionally, the established spin dependence of the local correlation, the local spin density approximation (LSDA), is integrated, ensuring that the svdW-DF framework can accurately capture the effects of spin polarization on all parts of the exchange-correlation energy.

The nonlocal correlation energy $E_{\mathrm{c}}^{\mathrm{nl}}$ component of svdW-DF is constructed by introducing a spin-dependent semilocal response function S_{xc}, with modifications to how spin influences the plasmon dispersion $\omega_q(\mathbf{r})$ in Eq. (2.57). The effective response parameter

$q_0[n]$ is adapted to $\tilde{q}_0[n_\uparrow, n_\downarrow]$ to reflect the explicit dependence on spin polarization. This adaptation is rooted in the formulation of the nonlocal correlation energy as a summation of zero-point energy shifts. The spin modifications impact the semilocal exchange-correlation holes and, by extension, the plasmon-pole shifts that defines the $E_{\mathrm{c}}^{\mathrm{nl}}$ through Eq. (2.62). Specifically, the correlation and exchange components of q_0, denoted as $q_{0c}[n]$ and $q_{0x}[n]$, are modified to incorporate spin density components, leading to $\tilde{q}_{0c}[n_\uparrow, n_\downarrow]$ and $\tilde{q}_{0x}[n_\uparrow, n_\downarrow]$. The correlation $\tilde{q}_{0c}[n_\uparrow, n_\downarrow]$ is given by

$$\tilde{q}_{0c}[n_\uparrow, n_\downarrow] = -\frac{4\pi}{3e^2}\varepsilon_c^{\mathrm{LSDA}}[n_\uparrow, n_\downarrow], \tag{2.73}$$

using the spin-dependent PW92 LDA correlation energy per particle $\varepsilon_c^{\mathrm{LSDA}}$. The exchange part is formed based on spin-scaling relation giving

$$\tilde{q}_{0x}\left[n_\uparrow, n_\downarrow\right] = \frac{n_\uparrow}{n_\uparrow + n_\downarrow} q_{0x}\left[2n_\uparrow\right] + \frac{n_\downarrow}{n_\uparrow + n_\downarrow} q_{0x}\left[2n_\downarrow\right], \tag{2.74}$$

where $q_{0x}[n]$ is the exchange part of $q_0[n]$, scaling the exchange component for each spin state.

2.5 Global Hybrids

The concept of hybrid functionals was first introduced by Becke in 1993 as a way to improve the accuracy of DFT for the electronic structure of molecular systems. They are for example employed to improve the description of charge-transfer systems which is especially useful in many soft matter and biological systems. However, hybrid functionals are today also employed to improve the descriptions of band gaps and electronic structure of strongly correlated systems (transition-metal complexes, transition-metal oxides, and rare-earth compounds).

The reason for their success is that they help cancel some of the self-interaction errors that arise in the Hartree term. In effect they compensate for forcing the exchange-hole description to comply with a simple approximation for an 'input' or GGA-level dielectric function $\epsilon(\omega)$. The idea is to mix orbital dependent Fock-exchange from Hartree-Fock theory with the density dependent functionals of DFT.

To include Fock exchange in the exchange functional, the underlying GGA exchange functional needs to be described in terms of an exchange hole that is free from Friedel oscillations and inherently include XC cancellation mechanisms. The exchange-hole is represented using a form function $J_{\mathrm{x}}^{\mathrm{GGA}}$ as

$$n_{\mathrm{x}}(\mathbf{r}; \mathbf{r}') = n(\mathbf{r}) \cdot J_{\mathrm{x}}^{\mathrm{GGA}}\left(s(\mathbf{r}); y = k_{\mathrm{F}}(\mathbf{r})|\mathbf{r} - \mathbf{r}'|\right), \tag{2.75}$$

where $|\mathbf{r} - \mathbf{r}'|$ is the separation between the electron at $\mathbf{r}$ and the exchange 'hole' at $\mathbf{r}'$, scaled by the local Fermi wavevector $k_{\mathrm{F}}(\mathbf{r})$. A proper formulation ensures that the LDA exchange-hole form, $n(r)J_{\mathrm{x}}^{\mathrm{LDA}}(s)$, emerges as the baseline $s \to 0$ limit.

The exchange enhancement factor derived from this model is given by

$$f_{\mathrm{x}}(s) = -\frac{8}{9}\int_0^\infty y \cdot J_{\mathrm{x}}^{\mathrm{GGA}}(s; y)\, dy. \tag{2.76}$$

This holds for PBE as well as for the exchange used in the nonempirical vdW-DFs. The shape of the analytic-hole formulation (see next section) [110] for the exchange-hole for PBE, PBEsol, CX and B86r is shown in Fig. 2.3.

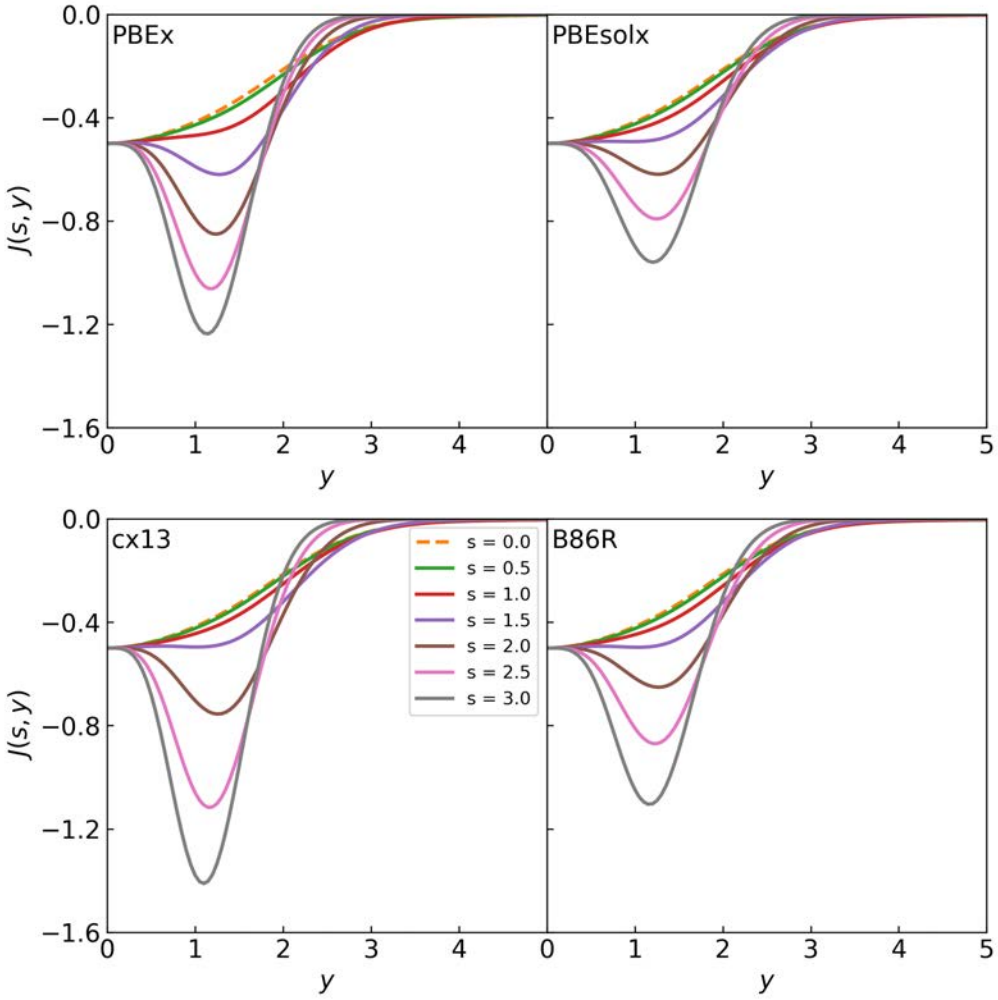

Figure 2.3: The AH exchange-hole shape $J(s, y) = n_{\mathrm{x}}(\mathbf{r}, \mathbf{r}')/n(\mathbf{r})$ as a function of the locally scaled separation $y = k_{\mathrm{F}}(\mathbf{r})|\mathbf{r} - \mathbf{r}'|$, which represents the distance between an electron at $\mathbf{r}$ and its corresponding 'hole' at $\mathbf{r}'$. The curves spans a range of local scaled density gradient values $s(\mathbf{r})$, from 0 (homogeneous electron gas) up to 3. Each of the four panels correspond to the exchange-hole for different functionals: PBE (PBEx) in the upper left, PBEsol (PBEsolx) in the upper right, and vdW-DF-cx (cx13 or LV-rPW86 exchange) in the lower left and B86r in the lower right.

A global hybrid is constructed by direct mixing of Fock exchange, exemplified by the functionals

$$E_{\mathrm{xc}}^{\mathrm{PBE0}} = \alpha E_{\mathrm{x}}^{\mathrm{Fock}} + (1-\alpha)E_{\mathrm{x}}^{\mathrm{PBE}} + E_{\mathrm{c}}^{\mathrm{PBE}}, \tag{2.77}$$

$$E_{\mathrm{xc}}^{\mathrm{CX0}} = \alpha E_{\mathrm{x}}^{\mathrm{Fock}} + (1-\alpha)E_{\mathrm{x}}^{\mathrm{CX}} + E_{\mathrm{c}}^{\mathrm{nl}} + E_{\mathrm{c}}^{\mathrm{LDA}}. \tag{2.78}$$

The PBE0 global hybrid functional [94, 111], defined as Eq. (2.77), commonly employs a mixing parameter of $\alpha = 0.25$. This choice was motivated in part by the analysis work of Perdew, Burke, and Ernzerhof [111], who introduced a coupling constant scaling approach to extend the PBE functional. The same $\alpha = 0.25$ choice is used as default in the vdW-DF-cx0 (CX0) global hybrid, Eq. (2.78) [102] and in the vdW-DF2-br0 (released together with cx0 to QE in 2017 [47, 112]). Yang, Schröder and Hyldgaard [112] repeated

the coupling constant analysis for CX for atomization energies to arrive at a particular implementation defined with $\alpha = 0.20$, called vdW-DF-cx0p (CX0P). This $\alpha = 0.2$ value is also used in B3LYP [64] for most molecular systems. Alternative non-empirical ways to determine the mixing involves tuning α to the reflect the inverse of the dielectric constant κ_0 [113].

Use of global hybrids is problematic when dealing with extended metallic systems. The exchange energy in a global hybrid is dominated by the Fock exchange at large separations $|\mathbf{r} - \mathbf{r}'|$ [100]. However, in a metallic system, the screening must impact all Coulombic interactions, for example these entering the exchange energy description Eq. (2.34).

2.6 Range-Separated Hybrid vdW-DFs

To create a general-purpose hybrid functional that avoids the previously mentioned issues, one needs to take into account the impact of screening on all $E_{\mathrm{KS}}[n]$ components. A *range-separated hybrid* (RSH) functional is based on the idea that the effectiveness of screening is dependent on the distance. There is little screening of the Fock-exchange part at short distances, but the screening reaches a complete compensation of the Coulomb interaction at large distances, at least in a metallic system. The design separates the exchange energy into long-range and short-range components using an error function separation

$$\frac{1}{r_{12}} = \frac{\mathrm{erfc}\,(\gamma r_{12})}{r_{12}} + \frac{\mathrm{erf}\,(\gamma r_{12})}{r_{12}}, \tag{2.79}$$

of the Coulomb matrix elements for electrons separated by $r_{12} = |\mathbf{r} - \mathbf{r}'|$ and a range-separation parameter γ.

We base the RSH vdW-DFs on the idea Henderson, Janesko and Scuseria (HJS) presented in 2008, where the exchange hole is constructed using an analytic hole (AH) method [110]. The AH exchange hole form $J_{\mathrm{x}}^{\mathrm{GGA}}(s; y)$ is based on an exchange hole model that is free from Friedel oscillations and permits an easy correction to the exchange enhancement factor $f_{\mathrm{x}}(s)$. For the AH framework, HJS first considered the exchange-hole corresponding to LDA:

$$\begin{aligned} J_{\mathrm{x}}^{\mathrm{LDA}}(y) = &- \frac{9}{4y^4}\left(1 - \mathrm{e}^{-\overline{\mathcal{A}}y^2}\right) \\ &+ \left(\frac{9\overline{\mathcal{A}}}{4y^2} + \mathcal{B} + \mathcal{C}y^2 + \mathcal{E}y^4\right)\mathrm{e}^{-\mathcal{D}y^2}, \end{aligned} \tag{2.80}$$

where the parameters $\mathcal{A}, \mathcal{B}, \mathcal{C}, \mathcal{D}$ and $\mathcal{E}$ are determined by physics constraints:

- The exchange hole is negative definite, meaning that the exchange hole density around an electron is always less than or equal to zero, relative to the electron density at that point.
- For spin independent systems, $n_x(\mathbf{r}, \mathbf{r}) = -\frac{1}{2}n(\mathbf{r})$ corresponding to the exchange hole at a point $\mathbf{r}$ halving the electron density at that point, effectively removing like-spin electrons.
- The normalization condition of Eqn. (2.32) ensures that the exchange hole integrates to -1, accounting for the "removal" of one electron.

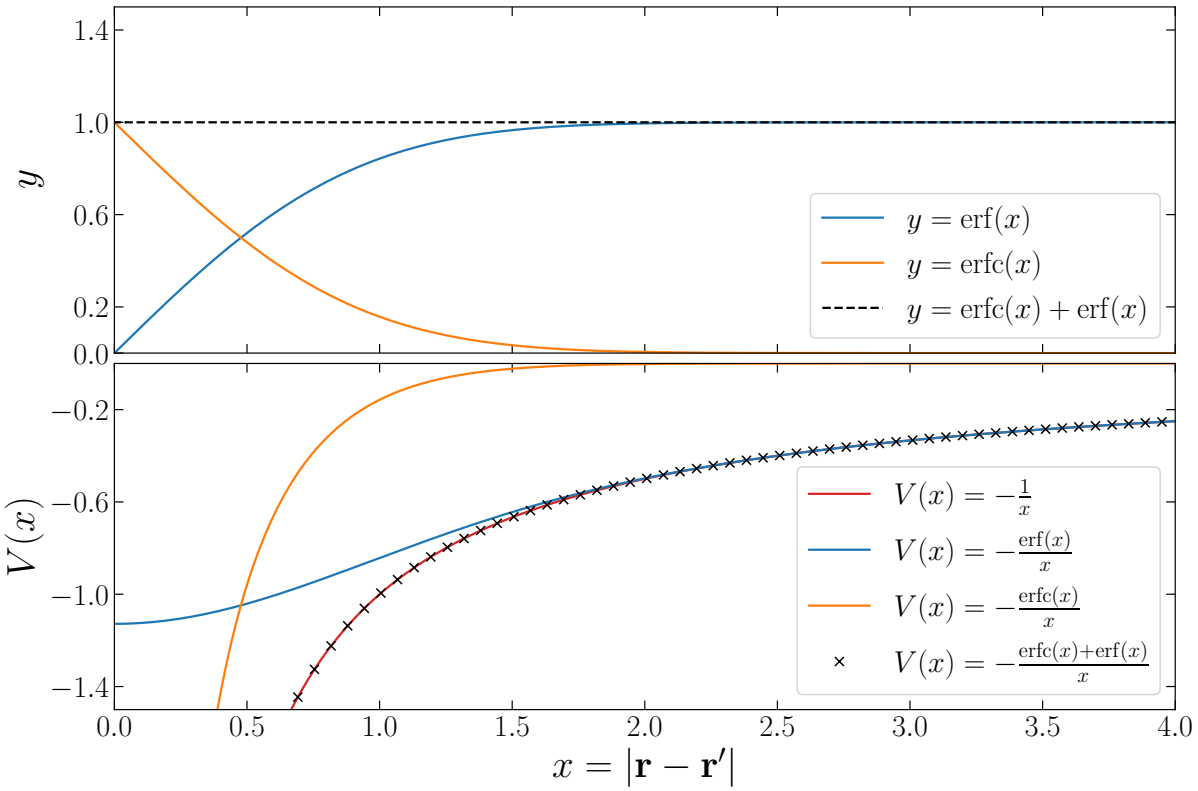

Figure 2.4: Illustration of the error and complimentary error function and their separation of the Coulomb interaction into long-range and short-range components. The top panel shows the plot of the error function, $\mathrm{erf}(x)$ (blue), and the complimentary error function, $\mathrm{erfc}(x)$ (orange), as a function of the separation x. The dashed black line shows the sum of the two functions, which is unity for all x. The bottom panel shows the separation of the Coulomb interaction (red) into long-range (blue) and short-range (orange) and their sum (black cross).

- The exchange hole integrates to the exchange energy as $E_x = -\frac{1}{2}\int_{\mathbf{r}}\int_{\mathbf{r}'}\frac{n(\mathbf{r})n_x(\mathbf{r},\mathbf{r}')}{r_{12}}$.

There are also some design constraints:

- The curvature of $J_{\mathrm{x}}^{\mathrm{LDA}}(s)$ is the same as that for the HEG at $y = 0$. This ensures that the exchange hole, and the subsequent GGA exchange enhancement factor, are consistent with the HEG at the local density.

- The exchange hole should approach the non-oscillating parts of the HEG at large y. The long-range contributions of these oscillations to the total energy and electron density are minimal, allowing for their exclusion for practical computational efficiency and accuracy

- It should maximize information entropy, to ensure that the resulting model is as unbiased as possible while satisfying known constraints. This approach effectively smooths out unnecessary details in the exchange hole, leading to a model that adheres closely to physical reality without overfitting to specific features that aren't supported by the underlying physics or constraints.

To fully determine the parameters of $J_{\mathrm{x}}^{\mathrm{LDA}}(y)$ requires numerical optimization to satisfy the constraints and design criteria, but they are determined once and for all by HJS.

The next step is to construct the gradient corrected exchange hole, $J_{\mathrm{x}}^{\mathrm{GGA}}(s;y)$ based on the gradient corrected enhancement factor $f_{\mathrm{x}}^{\mathrm{GGA}}(s)$ of choice. The gradient corrected exchange hole is essentially a Gaussian smearing of the LDA exchange hole, with the damping factor $\mathcal{H}(s)$,

$$\begin{aligned} J_{\mathrm{x}}^{\mathrm{GGA}}(s,y) =& \mathcal{I}(s,y)\mathrm{e}^{-s^2\mathcal{H}(s)y^2}, \\ \mathcal{I}(s,y) =& \left(\frac{9\overline{\mathcal{A}}}{4y^2} + \mathcal{B} + \mathcal{C}\overline{\mathcal{F}}(s)y^2 + \mathcal{E}\overline{\mathcal{G}}(s)y^4\right)\mathrm{e}^{-\mathcal{D}y^2} \\ & - \frac{4}{9y^4}\left(1-\mathrm{e}^{-\mathcal{A}y^2}\right). \end{aligned} \tag{2.81}$$

The $\overline{\mathcal{F}}(s)$ function (affecting the y^2 term of the LDA description) has the form

$$\overline{\mathcal{F}}(s) = 1 - \frac{1}{27C}\frac{s^2}{1+(s/2)^2} - \frac{1}{2C}s^2\mathcal{H}(s). \tag{2.82}$$

This choice ensures that it is possible to solve for $\mathcal{H}(s)$ analyticall at all s [110]. The $\overline{\mathcal{G}}(s)$ function (affecting the y^4 term of the LDA description) is essentially determined by the normalization condition. In the end both $\overline{\mathcal{F}}(s)$ and $\overline{\mathcal{G}}(s)$ is set through $\mathcal{H}(s)$.

To determine $\mathcal{H}(s)$ the energy integral is solved analytically, giving the exchange enhancement factor as

$$\begin{aligned} f_{\mathrm{x}}(s) = \overline{\mathcal{A}} &- \frac{4}{9}\frac{\mathcal{B}}{\lambda} - \frac{4}{9}\frac{\mathcal{C}\overline{\mathcal{F}}(s)}{\lambda^2} - \frac{8}{9}\frac{\mathcal{E}\overline{\mathcal{G}}(s)}{\lambda^3} \\ &+ \zeta\ln\left(\frac{\zeta}{\lambda}\right) - \eta\ln\left(\frac{\eta}{\lambda}\right), \end{aligned} \tag{2.83}$$

where $\zeta = s^2\mathcal{H}(s), \eta = \overline{\mathcal{A}} + \zeta$, and $\lambda = \mathcal{D} + \zeta$ all depend on $\mathcal{H}(s)$. Assuming $\mathcal{H}(s)$ to be a rational function of the form

$$\mathcal{H}(s) = \frac{\sum_{n=2}^{7} a_n s^n}{1 + \sum_{m=1}^{9} b_m s^m}, \tag{2.84}$$

the coefficients are determined by a fit to the numerical results found by solving Eq. (2.83) for $\mathcal{H}(s)$ at a range of s-values. Once these coefficients are determined, Eq. (2.82) gives $\overline{\mathcal{F}}(s)$ and the exchange hole is fully determined.

In the AHCX functional the analytic hole is constructed using the CX exchange enhancement factor, Eq. (2.65), to create a RSH vdW-DF that is designed to be accurate across periodic solids and extended systems. Specifically, it can retain accuracy also in the presence of charge transfer and strong correlation effects. In the AHBR functional the analytic hole is constructed using the vdW-DF2-B86r exchange enhancement factor of Eq. (2.68), to create a range-separated hybrid functional that performs at an excellent level for finite systems and for molecules [47].

With the exchange hole determined, the RSH can be constructed by mixing the long-range (LR) and short-range (SR) exchange components

$$E_{\mathrm{x}}^{\mathrm{Fock}} = E_{\mathrm{x,SR}}^{\mathrm{Fock}}(\gamma) + E_{\mathrm{x,LR}}^{\mathrm{Fock}}(\gamma), \tag{2.85}$$

$$E_{\mathrm{x}}^{\mathrm{GGA}} = E_{\mathrm{x,SR}}^{\mathrm{GGA}}(\gamma) + E_{\mathrm{x,LR}}^{\mathrm{GGA}}(\gamma), \tag{2.86}$$

using the error function separation in Eq. (2.79). To obtain for example the long-range components of the exchange energy we have

$$f_{\mathrm{x,LR}}^{\mathrm{GGA}}\left(k_{\mathrm{F}}, s; \gamma\right) = -\frac{8}{9}\int_0^\infty \mathrm{d}y\, y^2 J_{\mathrm{x}}^{\mathrm{GGA}}(s, y) \cdot \left[\mathrm{erf}\left(\gamma y / k_{\mathrm{F}}\right) / y\right]. \tag{2.87}$$

and similarly for the short-range components.

In the AHCX and AHBR design the short-range exchange energies are combined in a PBE0 like manner, together with the long-range component of the GGA exchange to give the final functional

$$E_{\mathrm{xc}}^{\mathrm{AHCX}} = (1-\alpha)E_{\mathrm{x,SR}}^{\mathrm{GGA}}(\gamma) + \alpha E_{\mathrm{x,SR}}^{\mathrm{Fock}}(\gamma) + E_{\mathrm{x,LR}}^{\mathrm{GGA}}(\gamma) + E_{\mathrm{c}}^{\mathrm{nl}} + E_{\mathrm{c}}^{\mathrm{LDA}}. \tag{2.88}$$

This is reminiscent of the HSE functional but using the truly non-local correlation energy of the vdW-DFs from the previous section. The RSH vdW-DF is based on the exchange hole corresponding to the actual GGA type exchange used in AHCX (or in AHBR). In the QE release, the Fock exchange mixing parameter defaults to $\alpha = 0.20$ based on CX0p analysis for atomization energy systems [114] and $\gamma = 0.106$ as in the HSE06 design. For bulk and surface problems we recommend setting the AHCX mixing at $\alpha = 0.25$.

Chapter 3

Computational Tools and Techniques

In this chapter we introduce the computational tools and techniques used in the attached papers.

3.1 Stress Analysis in Spin-Dependent van der Waals Systems

We first deal with the interplay between spin polarization and mechanical stress in vdW within the vdW-DF framework. The presentation begins by recalling the foundations of continuum followed by the ground laid by Nielsen & Martin [115], and by Sabatini et al. [116] for non-spin-polarized vdW-DF calculations. The goal is to enable effective KS structure optimizations: finding the equilibrium geometry of a material is in general a formidable task unless we can pursue variable-cell relaxations.

3.1.1 Stress tensor in the vdW-DF Framework

The stress tensor, σ_{ij}, plays a major role in variable cell calculations. This tensor quantity contains the material's response to applied or internal forces. Guiding both the atomic positions and the lattice parameters towards an equilibrium geometrical state where the system's total energy is minimized. On the other hand, strain ε_{ij}, quantifies the material's deformation, describing the relative displacement of atoms within the material. The strain tensor is defined as:

$$\varepsilon_{ij} = \frac{1}{2}\left(\frac{\partial u_i}{\partial r_j} + \frac{\partial u_j}{\partial r_i}\right), \tag{3.1}$$

where subscripts, i or j, identify Cartesian coordinates of the position vector r, u_i represents the displacement of particles in the direction i, and r_j denotes the coordinate in the direction j.

The relationship between stress and strain is can be connected through a fundamental quantity in DFT: the internal energy E of the system. When a material undergoes deformation there is mechanical work $dW = PdV$ done on the system. Here V denotes a volume of the material and P the pressure. This work, in turn, is related to the applied stress and the resultant strain:

$$dW = \sigma_{ij} d\varepsilon_{ij} V. \tag{3.2}$$

In the framework of DFT, we are treating ground state systems at 0 K, meaning the change in the system's internal energy is simply

$$dE = TdS|_{T=0} - PdV = -PdV. \tag{3.3}$$

The implication,

$$dE = -dW, \tag{3.4}$$

means that we can compute stress in terms of a DFT energy change,

$$\sigma_{ij} = -\frac{1}{V}\frac{\partial E}{\partial \varepsilon_{ij}}. \tag{3.5}$$

To proceed consider homogeneous strain of the crystal cell using small deformations or scalings given as

$$\tilde{r}_i = \sum_j (\delta_{i,j} + \varepsilon_{i,j})\, r_j\,, \tag{3.6}$$

where $\delta_{i,j}$ is the Kronecker delta. In a spin-balanced vdW-DF study, Sabatini et al. [116] derived the non-local correlation stress tensor corresponding to E_c^{nl} (Eq. (2.62)) by expressing the kernel in terms of the coordinate distance $D = |\mathbf{r} - \mathbf{r}'|$ and the $q_0(\mathbf{r})$,$q_0(\mathbf{r}')$ variables. Using the rigid scaling of the wavefunctions and the density derived by Nielsen and Martin [115], the resulting stress tensor is given by the equation

$$\begin{aligned}\sigma_{c,i,j}^{\mathrm{nl}} = \delta_{i,j}\left[2E_c^{\mathrm{nl}} - \int n(\boldsymbol{r}) v_c^{\mathrm{nl}}(\boldsymbol{r})\right] + \frac{1}{2}\int_{\boldsymbol{r}}\int_{\boldsymbol{r}'} n(\boldsymbol{r}) n\left(\boldsymbol{r}'\right)\frac{\partial\phi}{\partial D} C_{i,j}\left(\boldsymbol{r},\boldsymbol{r}'\right) \\ - \int_{\boldsymbol{r}}\int_{\boldsymbol{r}'} n(\boldsymbol{r}) n\left(\boldsymbol{r}'\right)\frac{\partial\phi}{\partial q_0} G_{i,j}(\boldsymbol{r})\end{aligned} \tag{3.7}$$

where the factors $C_{i,j}(\boldsymbol{r},\boldsymbol{r'})$ and $G_{i,j}(\boldsymbol{r})$ are given by

$$C_{i,j}(\boldsymbol{r},\boldsymbol{r'}) = (r_i - r_i')(r_j - r_j')/D, \tag{3.8}$$

$$G_{i,j}(\boldsymbol{r}) = \frac{\partial q_0(\boldsymbol{r})}{\partial|\nabla n(\boldsymbol{r})|}\,\frac{(\partial n(\boldsymbol{r})/\partial r_i)(\partial n(\boldsymbol{r})/\partial r_j)}{|\nabla n(\boldsymbol{r})|}. \tag{3.9}$$

Our aim is to formulate the stress $\sigma_{\mathrm{c},i,j}^{\mathrm{nl,sp}}$ that emanates from the spin-dependent formulation of the nonlocal-correlation energy, denoted as $E_{\mathrm{c}}^{\mathrm{nl,sp}}$, through the derivative of strain within the material's volume

$$\sigma_{\mathrm{c},i,j}^{\mathrm{nl,sp}} = -\frac{1}{V}\frac{\delta E_{\mathrm{c}}^{\mathrm{nl,sp}}}{\delta\varepsilon_{i,j}}\,. \tag{3.10}$$

To accomplish this we track the impact of both spin and coordinate scaling on the $E_{\mathrm{c}}^{\mathrm{nl,sp}}$ of Eq. (2.62). We have to take into account that the plasmon response is transformed, in case of a nonzero spin polarization, as represented in the changes in the local inverse length scale $q_0(\boldsymbol{r})$. This scale itself is determined by the spin-density gradients $\nabla n_{\mathrm{s}=\uparrow,\downarrow}(\boldsymbol{r})$, as specified in Eq. (2.52), thus we also need to track the stress induced by these variations. The gradients change with coordinate scaling because scaling implies both a density change and a change in taking the derivative with positions. The approach is simply to apply the chain rule for derivatives with strain. The transformation Jacobian, J, to the lowest order, reflects volume changes due to strain:

$$J = \left|\frac{d\tilde{\boldsymbol{r}}}{d\boldsymbol{r}}\right| = 1 + \sum_i \varepsilon_{i,j}\,, \tag{3.11}$$

with its strain derivative being $\partial J/\partial\varepsilon_{i,j} = \delta_{i,j}$.

The kernel ϕ, incorporates terms explicitly dependent on D, akin to the Hartree component in Coulomb stress analysis. The spin-polarized case requires evaluating $\partial\phi/\partial D$ with the spin-density distributions in in question.

In reciprocal space, transformations due to scaling are described by the transpose of $-\varepsilon_{i,j}$, affecting reciprocal lattice vectors as:

$$\tilde{G}_i = \sum_j (\delta_{i,j} - \varepsilon_{j,i}) G_j \,. \tag{3.12}$$

and in a plane-wave basis, the wavefunction $\Psi_{\boldsymbol{k},j} = \sum_{\boldsymbol{G}} c^{(j)}_{\boldsymbol{k}-\boldsymbol{G}} \exp\big(-i(\boldsymbol{k}-\boldsymbol{G})\cdot\boldsymbol{r}\big)$ expansion leads to important cancellations of many strain effects [65]. The scaling of spin-density components $n_{s=\uparrow,\downarrow}$, however, is governed by derivatives influenced by the volume factor

$$\frac{\partial n_s(\boldsymbol{r})}{\partial\varepsilon_{i,j}} = -\delta_{i,j} n_s(\boldsymbol{r}), \tag{3.13}$$

and we can use the logic of Nielsen and Martin's analysis to summarize the volume scaling of densities in terms of the XC potential's spin-resolved components $v^{\mathrm{nl}}_{\mathrm{c,s}}(r)$ as

$$-\delta_{i,j} \sum_s \int n_{\mathrm{s}}(\boldsymbol{r}) v^{\mathrm{nl}}_{\mathrm{c,s}}(\boldsymbol{r}) \mathrm{d}\boldsymbol{r}. \tag{3.14}$$

The comprehensive analysis also permits us to capture the effects of strain scaling on the spin-density gradient $\nabla n_s(\boldsymbol{r})$, assuming a constant variation of $n_s(\boldsymbol{r})$:

$$\frac{\partial n_s(\boldsymbol{r})}{\partial r_i} \to \frac{\partial n_s(\boldsymbol{r})}{\partial \tilde{r}_i} \approx \frac{\partial n_s(\boldsymbol{r})}{\partial r_i} - \sum_j \varepsilon_{i,j} \frac{\partial n_s(\boldsymbol{r})}{\partial r_j} \,. \tag{3.15}$$

For the magnitude of these derivatives, we find:

$$\frac{\partial|\nabla n_s(\boldsymbol{r})|}{\partial\varepsilon_{i,j}} = -\frac{1}{|\nabla n_s(\boldsymbol{r})|} \frac{\partial n_s}{\partial r_i} \frac{\partial n_s}{\partial r_j} \,, \tag{3.16}$$

whereby the volume scaling of the density is treated separately.

Transitioning to spin-polarized systems, we adapt these formulations to reflect the contributions from spin-up and spin-down electron density components, $n_\uparrow(\boldsymbol{r})$ and $n_\downarrow(\boldsymbol{r})$, affecting the plasmon dispersion and, consequently, the exchange-correlation energy in a spin-dependent manner. This necessitates an update to the stress tensor equation to a slightly modified form

$$\begin{aligned}\sigma^{\mathrm{nl,sp}}_{c,i,j} = \delta_{i,j} \left[2E^{\mathrm{nl}}_c - \sum_{s=\uparrow,\downarrow} \int n_s(\boldsymbol{r}) v^{\mathrm{nl,sp}}_{c,s}(\boldsymbol{r}) \right] + \frac{1}{2} \int_{\boldsymbol{r}} \int_{\boldsymbol{r'}} n(\boldsymbol{r}) n(\boldsymbol{r'}) \frac{\partial\phi}{\partial D} C_{i,j}(\boldsymbol{r},\boldsymbol{r'}) \\ - \int_{\boldsymbol{r}} \int_{\boldsymbol{r'}} n(\boldsymbol{r}) n(\boldsymbol{r'}) \frac{\partial\phi}{\partial q_0} \sum_{s=\uparrow,\downarrow} G^s_{i,j}(\boldsymbol{r}) \,,\end{aligned} \tag{3.17}$$

where

$$G^{s=\uparrow,\downarrow}_{i,j}(\boldsymbol{r}) = \frac{\partial q_0(\boldsymbol{r})}{\partial|\nabla n_s(\boldsymbol{r})|} \frac{(\partial n_s/\partial r_i)(\partial n_s/\partial r_j)}{|\nabla n|} \,. \tag{3.18}$$

This theoretical framework, inclusive of spin polarization effects was presented in **Paper A**and is now made available in the QE suite. It makes it possible for a vdW-DF stress analysis of spin polarized systems and enables us to conduct effective structure optimizations also for spin systems with important van der Waals binding.

3.1.2 Verification of Accuracy: Structural Properties

To validate our implementation of our spin vdW-DF stress result, we perform a series of test calculations on simple magnetic BCC iron and nickel. By comparing the results of a structural optimization using our spin-dependent stress tensor in variable cell relaxations to those obtained from polynomial fit on a set of fixed geometry calculations at different lattice parameters we can judge the robustness of our implementation.

Ni	PBE	CX	**Experiment***
$a_{0\,(\mathrm{fit})}$ [Å]	3.524	3.466	**3.510**
$a_{0\,(\mathrm{stress})}$ [Å]	3.524	3.466	
E_{coh} [eV]	4.668	5.217	**4.477**
B_0 [GPa]	197.0	226.3	**192.5**
B'	4.93	4.92	**4**
Fe	PBE	CX	**Experiment***
$a_{0\,(\mathrm{fit})}$ [Å]	2.843	2.794	**2.855**
$a_{0\,(\mathrm{stress})}$ [Å]	2.840	2.796	
E_{coh} [eV]	4.905	5.572	**4.322**
B_0 [GPa]	158.1	216.1	**168.3**
B'	7.51	6.41	**4.6**

Table 3.1: Results of the structural optimization of magnetic elements Ni and Fe using spin-vdW-DF stress calculations for CX compared to PBE. The subscript 'fit' implies that we have determined the lattice constants from a polynomial fit, while 'stress' denotes the results of a unit cell relaxations using the spin-stress tensor. All the bulk structure properties, the lattice constant a_0, cohesive energy E_{coh} and bulk modulus B_0, are compared to back-corrected experimental values given in the 'Experiments' column. This means they are adjusted for zero-point and thermal vibrational lattice effects so that the predicted values can be directly compared to corresponding empirical data.

As shown in Table 3.1, the results of the structural optimization of magnetic elements using spin-vdW-DF stress calculations for CX agree well with the polynomial fit results. They are also in good agreement with the experimental values. We take this as evidence of the consistency and predictive power of the spin-vdW-DF stress tensor. These results, together with those remaining of **Paper A**, indicate that we are set to model complex magnetic systems with both efficiency and accuracy.

3.2 Structure Search for Nearly Ordered Soft Matter

We use vdW-DFs, specifically CX, to characterize and predict mechanical- and ferroelectric response of polyvinyl fluoride (PVF) in **Paper D**. This is a prototypical soft-complex-

matter system due to the inconclusive experimental data and absence of single-crystal samples, which complicates the determination of its lowest-energy unit cell structure. Discrepancies in experimental data regarding PVF's conformation and tacticity further necessitate the use of vdW-inclusive, parameter-free DFT for an accurate structural assessment. One challenge with PVF lies in that it combines both a hard and soft nature: robust covalent-ionic bonds determine the molecular chains, while weaker van der Waals forces and steric interactions hold these chains together.

Our methodology centers on constructing a (small) database of potential PVF motifs, considering both ground state (GS) and excited state (ES) conformers, to predict the properties of crystalline PVF. Our initial set of candidate structures draws inspiration from the orthorhombic geometries of polyethylene (PE) and beta-phase PVDF crystals. Recognizing that a real PVF sample may contain multiple motifs due to the small energy differences between ES and GS states at room temperature, our approach is designed to encompass and navigate this diversity. We also verify whether the emerging structures are distinct polymer isomers or merely duplications of the same configuration.

We use CX to perform unit-cell relaxation and optimization, using it's accurate prediction of forces and stress to find the most stable structures. This is a technique previously applied in computational searches for metastable phases of materials like alumina and in investigations of adsorption phenomena in metal-organic frameworks [117–123]. Through calculations of full relaxations, we refine our initial candidates. We also eliminate redundancies to isolate distinct PVF motifs. These are then ranked according to their cohesive energies.

Figure 3.1 illustrates the initial configuration of 24 candidate structures for PVF, labeled A through X. All of them are organized in orthorhombic unit cells prior to relaxation and structures contain two CFH-CH_2 units, one per chain. One main difference in the initial structures is the positioning of fluorine (F) atoms: for half of the candidates, the F atoms are staggered between the chains, while for the remaining half, the F atoms are aligned along chain axis (same c-axis coordinate). The subsequent relaxation process transitions these initial guesses into a refined collection of 16 distinct motifs. The evolution of F-atom positions during relaxation is critical, with some motifs maintaining or transitioning to a 'shifted' arrangement (indicated with a subscript 's'), while others adopt or retain an alignment within the same c-plane (denoted with a subscript 'p'). This differentiation in F-atom positioning is important for defining the structural identity and properties of the resulting PVF motifs.

We find the set of lowest energy motifs (like GS) have a cohesive energy that is similar enough for them to simultaneously co-exist in a macroscopic PVF sample at room temperature. Also all of these them remain in an orthorhomic unit-cell geometry, i.e., they are consistent with trusted experimental observations [124–128].

Figure 3.2 presents the cohesive energy change as the structures transition from their initial guesses to their final motif forms. This transformation often leads different starting configurations to converge towards identical motifs, which is why we conduct a thorough pruning process to eliminate duplicates from our motif collection. Each unique motif is identified by the letter of its originating initial guess, for instance, 'G' signifies the motif that emerged as the ground state (GS). Following a systematic organization motifs are classified according to their cohesive energies, starting from the GS and ascending through various excited states (ES). A square symbol is used to mark those configurations, whether initial guesses or final motifs, that conform to an orthorhombic structure. This categorization includes not only the GS but also the first two ESs, denoted as ES1

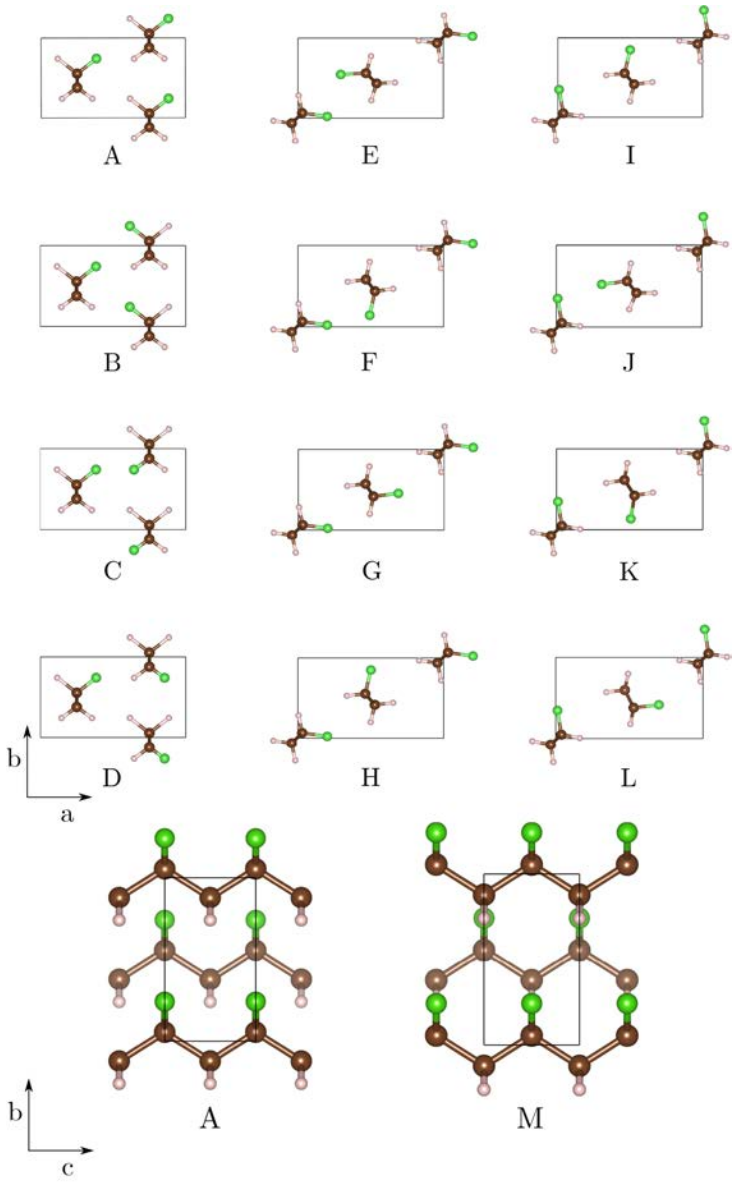

Figure 3.1: Initial structure guesses for two-PVF-chain unit cells that, upon relaxation, yield viable PVF motifs, candidates for crystalline PVF conformers. We explore different relative placements and rotations of the F-atoms between the chains, as shown in the upper panels. Initial guesses 1-12 and 13-24 evaluate scenarios where the F-atom positions on each chain are offset by one-half unit-cell vector c from, or aligned with, each other, depicted in the lower left and right panels, respectively.

and ES2. By establishing criteria for motif similarity based on energy and volume differences, we ensure a comprehensive catalog of low-energy conformers. Once we have the probable lowest-energy motifs, we utilize the two-stage unit-cell characterization scheme to reanalyze and refine our results. This approach ensures the accuracy of our predictions and allows us to determine the characteristics of macroscopic PVF at room temperature.

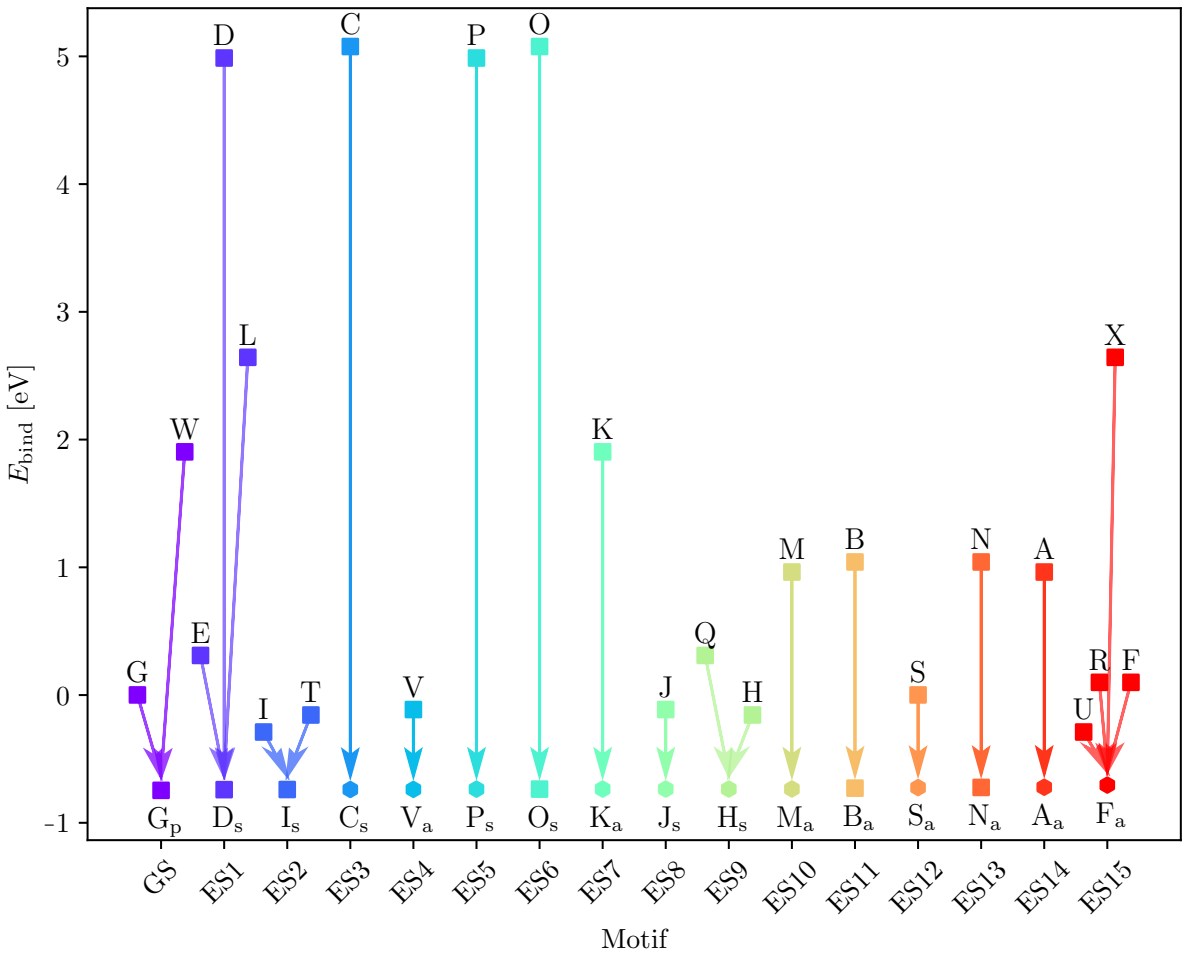

Figure 3.2: Energetics of relaxation for the database of PVF motifs, predicting plausible ground states (GS) and related meta-stable conformers. The y-axis displays the polymer binding energy from CX calculations with complete variable-cell and atomic relaxations.

3.3 Accuracy and Consistency Testing: Thermophysical Properties and Elastic Response

3.3.1 Thermophysical Properties

In this section we discuss accurate computation of thermophysical properties across soft and hard bulk materials. For soft matter, specifically polymers, we employ a variable-cell relaxation technique, utilizing a two-stage unit-cell characterization scheme to discern the ground-state structure and bulk properties. This approach distinguishes between the stronger covalent intra-polymer and weaker non-covalent inter-polymer interactions. For hard matter, like cubic bulk materials and magnetic metals, our analysis is based on energy versus lattice parameter curves and polynomial expansion, while ensuring the calculations adhere to the correct energy manifold. This dual methodology gives us a comprehensive strategy for validating the accuracy of thermophysical properties in diverse material classes.

When dealing with crystalline bulk materials, the ground-state configuration and it's

properties are essential for understanding the physics and mechanical response. Here we will focus specifically on lattice constants, atomic positions, and the bulk modulus. The utility of variable-cell relaxation techniques is in general hard to overstate, as it allows accurate determination of the ground-state structure of a material. These relaxation algorithms traverse the energy landscape in search of the minima by iteratively adjusting the lattice parameters and atomic positions. However, it will not give us elastic properties including the Bulk moduli. Moreover, the variable-cell relaxation is not guaranteed to always converge to the equilibrium structure, especially for soft matter. This is because the energy landscape can be highly anisotropic and skewed due to suboptimal k-point sampling (that is set according to the initial configuration). Finally, for range-separated hybrid studies in QE (e.g. HSE or RSH vdW-DFs), constrained variable-cell optimization does not seem to reflect a reliable account of the stress tensor, at present. In short, for a full characterization of thermophyiscal properties we also need an alternative based on fixed-cell calculations.

Crystalline bulk materials might seem simple, with their symmetric and repetitive structure. But their energy landscape can be highly complex, with multiple local minima. Unlike isotropic materials, crystalline substances may require the definition of multiple lattice parameters and atomic bases to accurately describe their ground state. We use an algorithm, introduced by Ziambaras and Schröder [129], implemented as a Python tool, to handle large datasets and automate the process. This approach integrates the calculation of the bulk modulus and its pressure derivative into the analysis procedure. It offers a more straightforward and precise alternative to fitting data to semi-empirical equations of state (EOS), such as those proposed by Murnaghan or Birch. Because it's derivation is based on the truly elastic behavior, consistency between the set of elastic coefficients and the computed bulk modulus is guaranteed — when used correctly (that is, with a balanced sampling of the phase space). To determine the material's equilibrium structure, we minimize the free energy within the multidimensional lattice parameter space, while accounting for the space group of the material.

To proceed we form a vector $\boldsymbol{x}$ of the necessary variables, where the elastic response corresponds to small deviations $\delta\boldsymbol{x} = \boldsymbol{x} - \boldsymbol{x}_0$ of the structural parameters from the equilibrium structure $\boldsymbol{x}_0$. Using both hybrid and non-hybrid functionals we calculate the total energy per unit cell, $E(\boldsymbol{x})$, for a set of various structure configurations $\{\boldsymbol{x}\}$ around the equilibrium configuration. For each of the configurations we determine the ground-state geometry by letting the atoms relax to their equilibrium positions using the BFGS algorithm. This set of energy and lattice parameter values, $\{E, \boldsymbol{x}\}$, is used to establish a natural potential hypersurface in the parameter space. The curve or surface naturally lends itself to a multidimensional fit of the total energy variation. The fitting is expressed through a polynomial expansion

$$E(\boldsymbol{x}) = k + \frac{1}{2}M_{ij}\delta x_i \delta x_j + \frac{1}{3!}C_{ijl}\delta x_i \delta x_j \delta x_l + \mathcal{O}(\delta\mathbf{x})^4 \tag{3.19}$$

where k, M, and C represent tensors of fitting constants (of zero-, second- and third-rank respectively), allowing us to directly determine the equilibrium structure $\boldsymbol{x}_0$.

From this polynomial expansion, we can make an analogous expansion around the equilibrium volume $V_0 = V(\boldsymbol{x}_0)$ using the gradient

$$\boldsymbol{g} = \nabla V(\boldsymbol{x})\big|_{\boldsymbol{x}=\boldsymbol{x}_0}\,, \tag{3.20}$$

and the Hessian

$$H = H(V(\boldsymbol{x}))\big|_{\boldsymbol{x}=\boldsymbol{x}_0} = \left[\left\{\partial^2 V(\boldsymbol{x})/\left(\partial x_i \partial x_j\right)\right\}_{ij}\right]_{\boldsymbol{x}=\boldsymbol{x}_0}, \tag{3.21}$$

of the volume.

By a systematic treatment of the structural changes induced by the pressure $p = -\partial E/\partial V$ at the minimum of the zero-temperature enthalpy

$$\mathcal{H}(\boldsymbol{x}, p) = E(\boldsymbol{x}) + pV(\boldsymbol{x}), \tag{3.22}$$

we can extract the bulk modulus B_0 as

$$B_0 = \frac{V_0}{\boldsymbol{g}^T M^{-1} \boldsymbol{g}}, \tag{3.23}$$

We also get the associated pressure derivative B' by [129]

$$B_0' = V_0 \frac{3\boldsymbol{g}^T M^{-1} H M^{-1} \boldsymbol{g} - C_{ijl}\left(M^{-1}\boldsymbol{g}\right)_i \left(M^{-1}\boldsymbol{g}\right)_j \left(M^{-1}\boldsymbol{g}\right)_l}{\left(\boldsymbol{g}^T M^{-1} \boldsymbol{g}\right)^2} - 1. \tag{3.24}$$

The value of B_0 and B' characterize a material's mechanical properties in a way that is consistent with the elastic properties constants [129].

To make sure that our implementation of the procedure is correct and robust, we have validated it versus the Murnaghan (often referred to as the Birch-Murnaghan (BM)) EOS [130, 131]:

$$E_{\mathrm{BM}}(V) = -E_0 + \frac{B_0 V}{B_0'}\left[\frac{\left(V_0/V\right)^{B_0'}}{B_0' - 1} + 1\right] - \frac{V_0 B_0}{B_0' - 1}, \tag{3.25}$$

where E_0 is the energy at the equilibrium unit-cell volume V_0.

We now shift our focus to a discussion of some practical considerations associated with employing our method towards benchmarking functionals on the thermophysical properties of bulk materials. These aspects and issues are likely relevant to any benchmarking method in this context. Two primary challenges were identified:

1. Ensuring computational consistency with the correct, lowest-energy configuration. Maintaining adherence to the global minimum, as far as it is possible, is crucial for a valid and fair comparison. Intersections with energy manifolds of low-energy phases can produce discontinuities within the energy landscape, for example in magnetic systems.

2. Accurately sampling the predicted energy-strain behavior near the equilibrium structure. This requires calibration of the lattice-parameter grid to ensure it effectively captures each functional's prediction of the material's elastic properties.

A discontinuity in the energy curve is a tell tale sign the calculations are not consistently sampling the same minima of the same configuration. We found that the reason as to why the computations break consistency was often found in the k-point sampling or in the plane-wave cutoff. Both of which needs to be determined for a choice of pseudopotential, ideally picked to give the best accuracy for all materials (when they are subjected

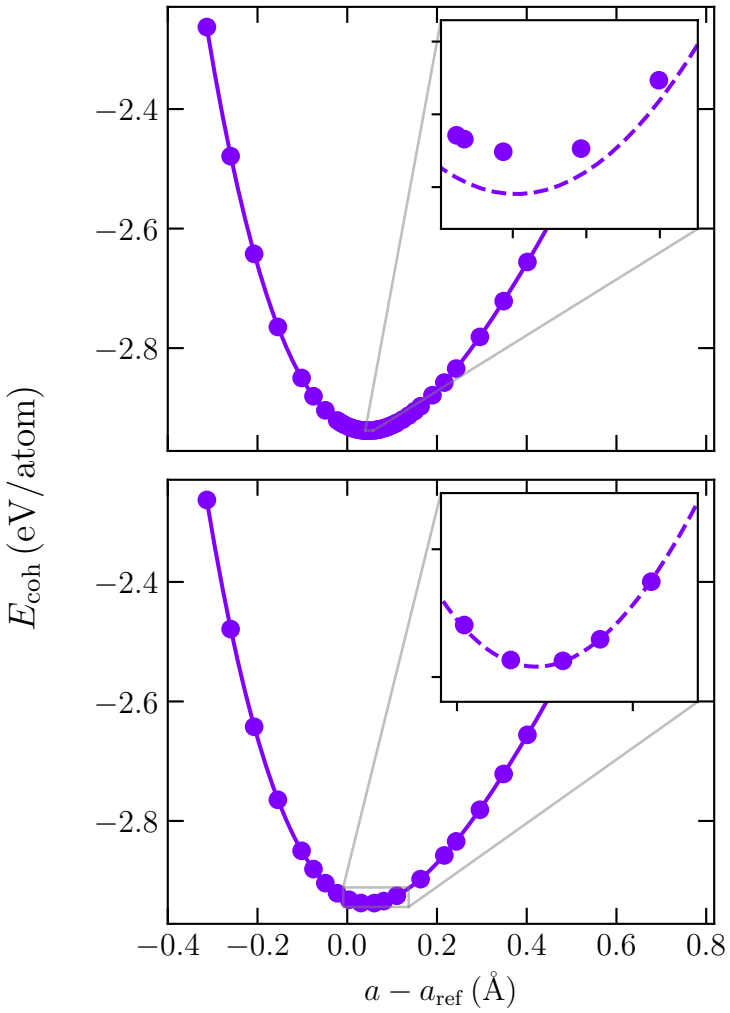

Figure 3.3: Overfitting challenge in modeling the energy variation with lattice parameter for Ag in AHCX. The top panels shows an analysis when we over sample specific regions of the lattice parameter space. The bottom panel shows that it is only when we keep a balanced (AHCX) lattice parameter representation that we can maintain consistency in the representation of the elastic properties around the minima, see insets.

to all relevant deformations). These convergence parameters has to be extracted from a screening process; after converging them for each material, pseudopotential and functional we pick the set of parameters that corresponds to the highest bound on the parameters. In this way we can ensure that these parameters can be used for all materials without convergence issues.

When dealing with cells that vary in size, the plane-wave cutoff $E_{\mathrm{cut}}^{\mathrm{PW}}$ and the corresponding real-space grid can influence the energy mapping even though the cutoff is converged with respect to the total energy. For a given $E_{\mathrm{cut}}^{\mathrm{PW}}$, the minimum spacing of points (along each cell parameter) in real-space is $\Delta_{\boldsymbol{R}} = \pi(E_{\mathrm{cut}}^{\mathrm{PW}})^{-1/2}$. This is the Nyquist criterion [132] for the real-space grid, and gives a lower bound for the real-space grid density to retain the information. The total number of points in the grid is thus determined by the length of the cell parameter and the density of the grid, i.e., energy cutoff and the cell volume. In practice, all extended-system (plane-wave) DFT codes utilize FFT to

transform between real- and reciprocal space. The speed-up of FFT relies on decomposing the number of grid points into small prime factors. Codes will obey this criteria by selecting a grid size that is a product of small prime numbers above the specified lower bound. Consequently, the final density of the FFT grid may vary slightly between calculations — with identical cutoffs — for different cell sizes. To mitigate potential artifacts arising from grid size selection, we increase the plane-wave cutoff to a level where small variations in the FFT grid density become negligible Although the choice of FFT grid generally preserves the accuracy and continuity of the energy mapping, issues primarily occurred when substantial strains (i.e. large changes from the equilibrium cell volume) were applied to the cell.

Computing the electronic structure for both compressed and expanded lattice configurations also necessitates carefully choosing the k-point mesh. The k-point mesh must be dense enough to represent the details of the smallest Brillouin zone among the structures. Insufficient k-point density will lead to the non-converged energies for the high-strain states, resulting in serious inaccuracies in the energy mapping. If we do not accurately sample the electronic states near the Fermi surface of the ground state configuration, we cannot possibly expect to accurately capture the details of the electronic or magnetic properties of the materials.

In Figure 3.3 we highlight the importance of using a balanced sampling in benchmarking functionals for thermophysical properties. In the upper panel we show the modeling that arise when using a dense lattice parameter grid, but only around the experimental lattice value. We then get problems by overfitting, where the polynomial fit does not run through the calculated points close to the equilibrium structure, as shown in the inset. Using this modeling would significantly alter the calculated bulk modulus, failing to represent the actually predicted elastic properties of the material.

The lower panel of Figure 3.3 illustrate the self-consistency criterion that we introduce to safe guard against overfitting and other grid related issues. We use a balanced data set obtained by DFT (dots) and we check (inset) that the the fitting extracted from the full data set also capture the near equilibrium DFT data.

I finally note that study of magnetic elements require special considerations. Spin-polarized calculations are inherently more sensitive to the k-point sampling due to the increased complexity in the electronic structure of these materials. The presence of magnetic degrees of freedom can also complicate the energy landscape, typically resulting in multiple shallow local minima that can significantly influence the stability and properties of both the calculation and the system itself.

The above discussion underscores the rigorous computational practices needed in **Paper B**to ensure accurate benchmarking of the thermophysical properties of bulk materials. Meticulous work went into making sure the sampling density was sufficient and that the calculations remained on the correct energy hypersurface.

3.3.2 Verification of Thermophysical Properties

Bulk Solids

In figure 3.4 we show an example of the energy vs lattice parameter curve that we used to benchmark functionals for thermophysical properties in **Paper A**. Each row in the figure corresponds to a different functional, while each column corresponds to a different bulk metal. To make the comparison as un-biased as possible, we have back-corrected the experimental values for zero-point and thermal vibrational effects. To ensure the accuracy of our method, we also cross-checked our Bulk-moduli predictions with those obtained via the BM EOS.

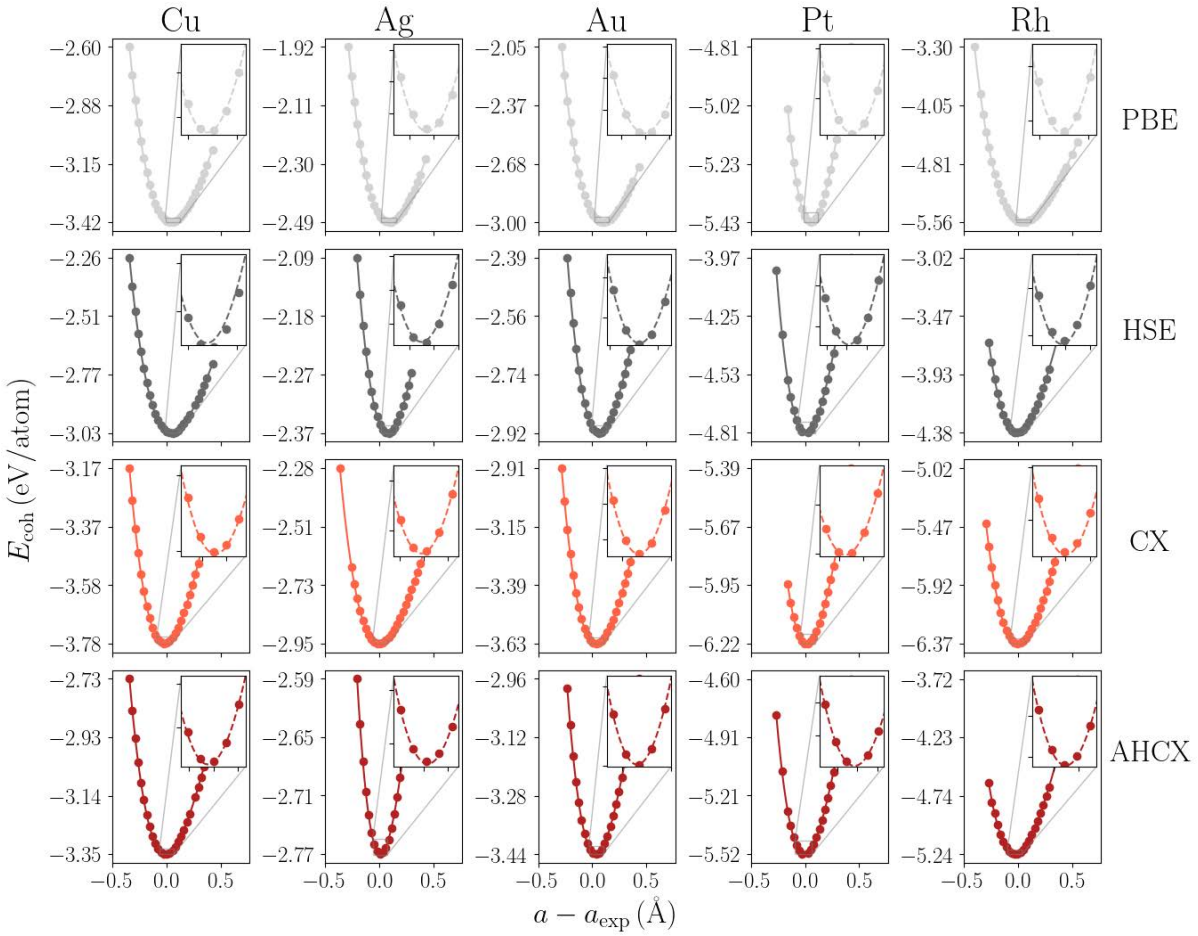

Figure 3.4: Variations of benchmarking work for thermophysical properties: energy vs lattice parameter for a set of bulk metals (per column) and functionals (per row). The top two rows concerns modeling for PBE followed by it's RSH HSE. The bottom two rows shows the modeling obtained for CX and for it's RSH form AHCX. The lattice parameter axis is shown against the back-corrected experimental value, and the cohesive energy is computed against the atomic reference energy, in the corresponding functional.

Soft Matter Systems

As previously mentioned the variable-cell relaxation technique also has its limitations when dealing with soft matter. In the case of polymers, the covalent interactions within the polymer chains are much stronger than the vdW interactions between the polymer chains are weak. This means that the energy potential surface will be highly anisotropic in the lattice parameter space. Furthermore, full unit-cell relaxation within the framework of plane-wave DFT is based on a k-point sampling which is determined by the size of the initial unit cell. To mitigate these issues, we undertake repeated variable-cell calculations, initiating each iteration from the structure predicted in the preceding step. This iterative refinement, which includes updates to the k-point sampling based on the evolving geometry of the unit-cell, ensures that our model progressively aligns with the physical reality of the system until convergence criteria for both structure and energy are met. Such diligence is especially critical in the context of soft-complex-matter systems, where a thorough exploration for conformers is paramount to validate the comprehensiveness of the search.

Parallel to this approach we utilized a two-stage unit-cell characterization scheme to discern the ground-state structure. It builds upon the previous lattice parameter extension method, while separating the intra-chain covalent interactions along the polymer chain from the inter-chain vdW interactions in the directions orthogonal to the chains.

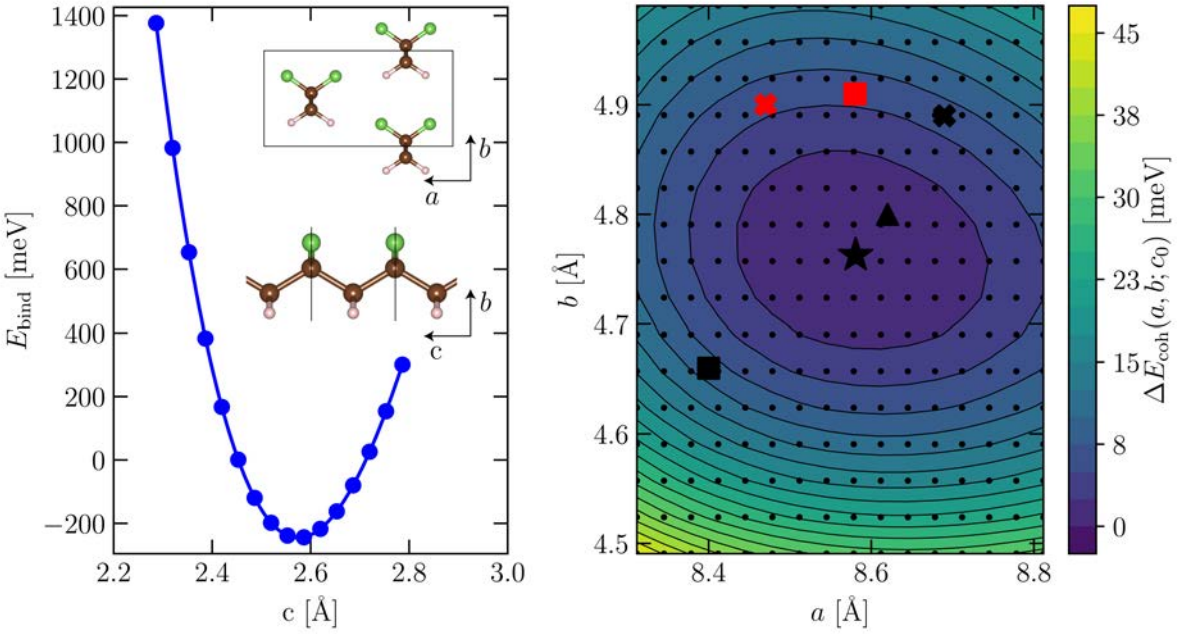

Figure 3.5: Figure of the cohesive energy mapping per lattice parameter for PVDF. The left panel shows the energy versus lattice parameter curve for the PVDF polymer chain along the c-axis (chain direction) dominated by covalent bonding. The right panel shows the energy versus lattice parameter curve for the a and b lattice parameters, which are transverse to the chain direction and dominated by vdW interactions. The black star denotes the result of the variable-cell relaxation, which is in good agreement with the polynomial expansion. The other black makers denotes the result of the variable-cell relaxation in: square for vdW-DF2, triangle for vdW-DF1 and cross for PBE0. The red cross shows the results from x-ray diffraction on a sample drawn at 323 K Ref. [125], while the red square is x-ray diffraction from Ref. [133].

In the left panel of Figure 3.5 we show the energy versus lattice parameter curve for the PVDF polymer chain along the c-axis (chain direction). For each length of the chain (c-axis lattice parameter) we have relaxed the atomic positions of the structure and calculated the energy. We then fit the energy to a polynomial expansion. After finding the equilibrium c lattice parameter, we make a similar mapping of the energy surface for the a and b lattice parameters, which are transverse to the chain direction. As can be seen, around the minima the energy variation is shallow. Nevertheless, the result of the variable-cell relaxation (black star) is in good agreement with the description extracted by a polynomial expansion of the cohesive energy landscape.

3.3.3 Elastic constants

To understand the mechanical stability and elastic properties of a crystalline material, like PVF, we need to again revisit some continuum mechanics.

Going from the first derivative with respect to strain for stress, Eq. 3.5, to the second derivative we can define the matrix second-order elastic constants matrix of a crystal

$$C_{ij} = \frac{1}{V_0}\left(\frac{\partial^2 E}{\partial\varepsilon_i \partial\varepsilon_j}\right), \tag{3.26}$$

where the single indexed $\varepsilon_i \equiv \varepsilon_{ii}$ symbolizes diagonal strain, and where V_0 still denotes the equilibrium volume of the unit cell.

This matrix, also known as the stiffness or elastic matrix and as the name suggest, determines the elastic response of a crystal. It's has the structure of a symmetric 6×6 matrix, containing 21 independent components. The specific symmetry of the crystal's class imposes further constraints, reducing the independent elastic constants required to describe it. For a homogeneously deformed crystal under infinitesimal strain, the energy relationship is given by the quadratic form:

$$E = E_0 + \frac{1}{2}V_0 \sum_{i,j=1}^{6} C_{ij}\varepsilon_i\varepsilon_j + O\left(\varepsilon^3\right). \tag{3.27}$$

Crystalline stability, absent external forces and within the harmonic approximation, is ensured when we find all phonon modes have positive frequencies across all wave vectors. This is sometimes called dynamical-stability criterion.

A simpler but less reliable approach is to look at the elastic response: Stability is plausible if the theory characterization predicts that the elastic energy, encapsulated by the quadratic form above, remains positive for any non-zero strain ($E > 0, \forall\varepsilon \neq 0$). In that case we say that the material fulfills the so called elastic-stability criterion.

The elastic stability criterion is equivalent to, as was first realized by Born [134], the necessary and sufficient mathematical conditions:

1. The C matrix must be definitively positive.
2. All eigenvalues of C are required to be positive.
3. Sylvester's criterion necessitates all leading principal minors of C (the determinants of its $k \times k$ upper-left submatrix for $1 \leq k \leq 6$) to be positive.
4. A chosen set of minors from C should all be positive, which can include trailing minors or any other selected set.

These conditions are the generic Born criteria for elastic stability, apply universally, irrespective of the crystal's symmetry, and are inherently nonlinear.

In summary, we can by theory check if a predicted material is stable. Specifically, necessary but not sufficient conditions for stability requires that all diagonal elements of C must be positive ($C_{ii} > 0, \forall i$). Additionally, a necessary condition concerning the relationship between off-diagonal and diagonal elements is [135]:

$$\left(C_{ij}\right)^2 < C_{ii}C_{jj}, \forall i, j. \tag{3.28}$$

In the case of PVF, the orthorhombic symmetry impose a unique set of constraints on the elastic constants. The orthorhombic crystal system has three mutually perpendicular axes of different lengths, and falls into the symmetry group D_{2h}^{17}. This symmetry group has 9 independent elastic constants, which can be determined from the stiffness matrix,

$$\boldsymbol{C}_{\text{ortho}} = \begin{pmatrix} C_{11} & C_{12} & C_{13} & & & \\ \cdot & C_{22} & C_{23} & & & \\ \cdot & \cdot & C_{33} & & & \\ & & & C_{44} & & \\ & & & & C_{55} & \\ & & & & & C_{66} \end{pmatrix}. \tag{3.29}$$

By the generic Born it follows that we can expect stability (in a throy-predicted material) if the computed C_{ij} values satisfy [136]:

$$\begin{aligned} &C_{11} > 0, \quad C_{11}C_{22} > C_{12}^2, \\ &C_{11}C_{22}C_{33} + 2C_{12}C_{13}C_{23} - C_{11}C_{23}^2 - C_{22}C_{13}^2 - C_{33}C_{12}^2 > 0, \\ &C_{44} > 0, \quad C_{55} > 0, \quad C_{66} > 0, \end{aligned} \tag{3.30}$$

with good margin. These criteria follows by formal search for eigenvalues of Eq. (3.30) Calculations of the elastic coefficients gives a way to further test the consistency of our stress-based motif search.

For a practical motif-structure stability test, we extract the elastic constants by applying strain to the unit cells while evaluating the volume-specific strain energy. We allow for full atomic relaxations at each deformation increment, because the polymer crystals are not centrosymmetric. This prevents artificially high stiffness emerging as a result of covalent bond stretching.

3.4 Predicting Plastic Deformation using vdW-DFs

In our prediction of plastic deformations using vdW-DFs, we study the processes of slip deformations in crystalline regions of PVF and PVDF. We focus on this deformation mechanism based on empirical observations showing that slip is generally the dominant deformation mechanism in crystalline regions of polymer samples. The slip process is characterized by the movement of polymer chains along specific planes, designated using Miller indices (ijk), where the slip occurs along vectors $[ijk]$. The dominant slip planes in polymers are the ones which preserve the integrity of the polymer chains throughout the deformation process.

To model the slip mechanism in polymers, we employ a supercell skew technique as illustrated in Figure 3.6. This method enables the simulation of a localized slip interface (as seen in the lower panel of Figure 3.6) by gradually skewing supercell vectors by small increments $\delta_{[ijk]}$. As we skew the supercell, we track the so-called generalized stacking fault energy (GSFE) which represents the change in binding energy due to the specific deformation, or displacement of the atoms, relative to the optimal stacking configuration. The set of GSFEs for each deformation increment forms an energy surface commonly refereed to as a γ-surface in mechanics. We restrict relaxations to atomic adjustments perpendicular to the shear plane to accurately capture the deformation's nonuniform and anisotropic characteristics across various strain levels. In so doing we capture localized in-plane deformation mechanisms under plane strain conditions.

In **Paper D** we specifically focus on slip in the (100) and $(1\bar{1}0)$ planes, as these are the most common slip planes in the non-flourinated PE crystals. This means we incorporate both along-chain and transverse slips modes as shown in Figure 3.7, denoted by $\delta_{[001]}$ and $\delta_{[ij0]}$ respectively. A noteworthy contribution to GSFE in PVF and PVDF, apart from the vdW interactions, is the steric hindrance arising from the interaction between the fluorine and hydrogen atoms. Changes in the GSFE due to steric hindrance and vdW interactions are critical in determining the slip resistance of the polymer chains.

To identify energy-density signatures of steric hindrance and vdW attraction, we utilize a detailed analysis of cohesive energy contributions, dissecting the gradient-correction-to-exchange e_x^{gc} and nonlocal-correlation e_c^{nl} components of the exchange-correlation energy. This is facilitated by the post-DFT-processing ppACF code, produced in-house to enable detailed study of the energy contributions of the functional used. The energy-densities extracted are defined as:

$$e_x^{\mathrm{gc}}(\boldsymbol{r}) \equiv e_x^{\mathrm{LDA}}(n)[f_x(s(\mathbf{r})) - 1]\,, \tag{3.31}$$

$$e_c^{\mathrm{nl}}(\boldsymbol{r}) \equiv \frac{n(\mathbf{r})}{2}\int \Phi[n](\mathbf{r},\mathbf{r}')\, n\left(\mathbf{r}'\right)\, d\mathbf{r}'\,, \tag{3.32}$$

where e_x^{LDA} denotes the energy density of exchange in the local-density approximation, $s(\mathbf{r})$ is the reduced density gradient, $f_x(s)$ represents the exchange-enhancement factor of Eq. (2.45), and $\Phi[n](\mathbf{r},\mathbf{r}')$ is the nonlocal-correlation kernel defined in Eq. (2.62).

To compute the corresponding contribution to the cohesive energy, we use ppACF to extract the energy term for the DFT calculation of the structure of interest. This essentially involves three different post-processing extractions: one for the full polymer crystal, and two for the structures containing each of the monomer chains. By subtraction

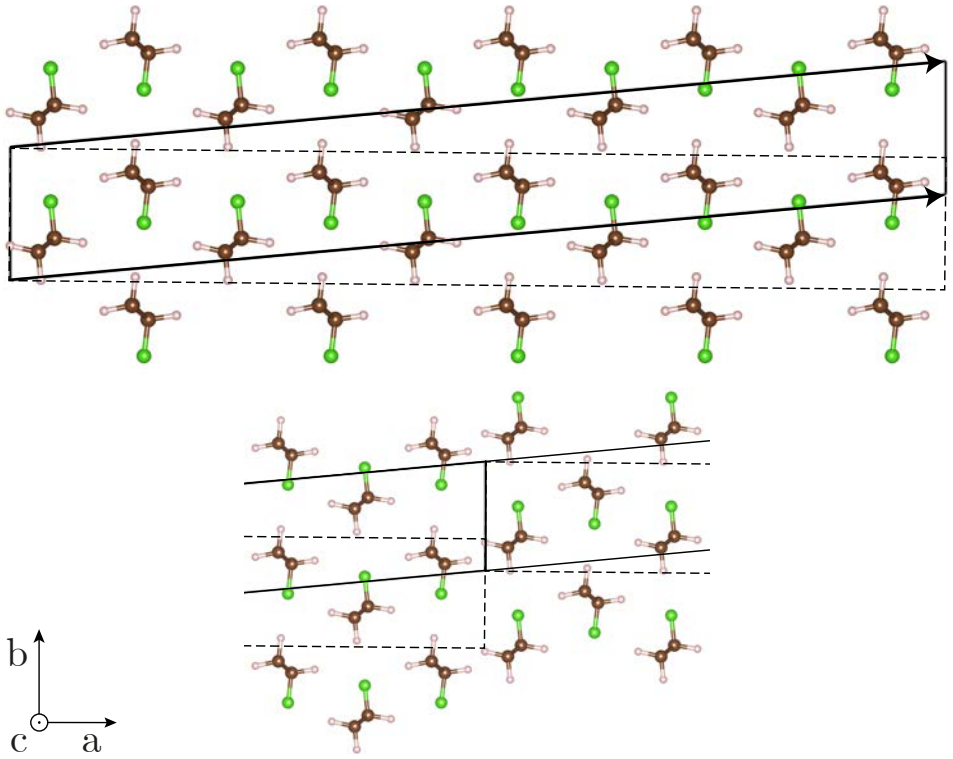

Figure 3.6: Illustration of the super cell skew method utilized to study the crystallographic slip process. In our computational approach, we impose slip deformations through shear-induced deformations within a supercell framework. By applying a incremental skew configurations upon the super cell we track changes in generalized stacking fault energy (GSFE) and thus slip resistance. This setup, illustrated for ground-state PVF, delineates the transition from an un-deformed state (dashed) to a (1/2)[100] deformation (indicated with arrows). In effect we are simulating an interface structure, as shown in the lower panel, while allowing for atomic relaxations perpendicular to the interface.

we gain our markers, i.e., key polymer-cohesion-energy contributions

$$\Delta e_x^{\mathrm{gc}}(\boldsymbol{r}) = -e_x^{\mathrm{gc,crystal}}(\mathbf{r}) + 2e_x^{\mathrm{gc,monomer}}(\mathbf{r})\,, \tag{3.33}$$

$$\Delta e_c^{\mathrm{nl}}(\boldsymbol{r}) = -e_c^{\mathrm{nl,crystal}}(\mathbf{r}) + 2e_c^{\mathrm{nl,monomer}}(\mathbf{r})\,. \tag{3.34}$$

We can visualize these energy density differences as the change under strain, compared to their ground state values. This approach centers on polymer cohesion and is our chosen framework to analyse the effects of strain and steric hindrance induced under slippage. In the ground state, polymer chains are ideally positioned at an optimal separation, maintaining a force minimum conducive to material stability. Under strain, however, the structure is shifted out of the minima, leading to varied rates of change in the cohesion-energy contributions. These changes reflects the resistance to slip that we express as an energy barrier to a transformation. The magnitude of both the gradient-correction-to-exchange and nonlocal-correlation cohesion-energy contributions tends to increase as the overlap between the electron-density tails of adjacent polymer chains grows. The nonlocal-correlation cohesion-energy contribution can also facilitate binding across void spaces within crystal.

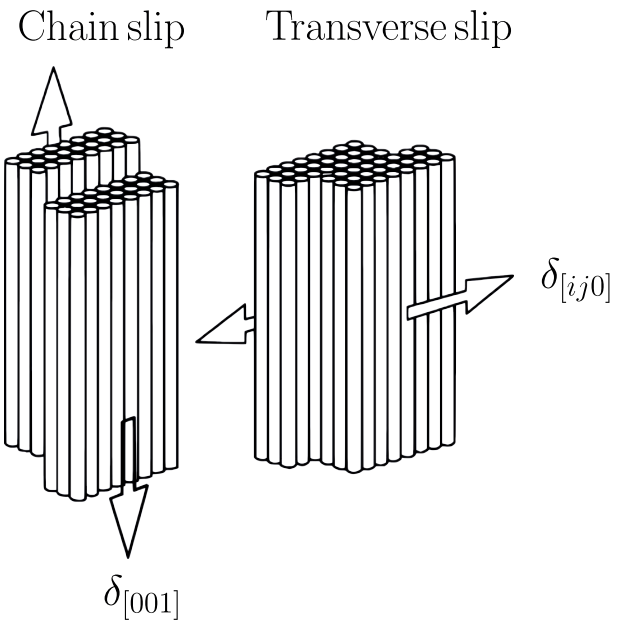

Figure 3.7: The principal deformation modes of the crystallographic slip process in crystalline plymers.

To gain a quantitative understanding of the energy contributions in the context of polymer cohesion, we can also integrate the contributions over the supercell volume to obtain the total energy;

$$\Delta E_{\mathrm{x}}^{\mathrm{gc}} = \int \Delta e_x^{\mathrm{gc}}(\mathrm{r}) d\mathbf{r}, \tag{3.35}$$

$$\Delta E_{\mathrm{c}}^{\mathrm{nl}} = \int \Delta e_c^{\mathrm{nl}}(\mathrm{r}) d\mathbf{r}. \tag{3.36}$$

3.5 Modern Theory of Polarization in Soft Matter

Defining the spontaneous polarization $\boldsymbol{P}_\mathrm{s}$ of a periodic system is not a trivial task, solved in the 1990s with the development of the *Modern Theory of Polarization* [137–139] The net polarization results from a natural alignment of electric dipoles, characterized by an asymmetric distribution of charge within the unit cell. A straightforward (but dysfunctional) adaptation of the classical electromagnetic definition involves replacing point charges q with the charge density $\rho(\boldsymbol{r})$, which includes both the ionic delta-functions and the electronic charge density. Multiplying this density by the distance $\boldsymbol{r}$ (to calculate the dipole moment) and dividing by the unit cell volume V_0 yields

$$\mathbf{P}_\mathrm{dip} = \frac{1}{V_0}\int_\mathrm{cell} \mathbf{r}\rho(\mathbf{r})d^3r. \tag{3.37}$$

Looking at Figure 3.8, the problem with this approach becomes apparent. There is in principle an infinite number of ways to define the unit cell. When we consider the electron contribution to the dipole moment, as computed using Bloch functions, we get

$$\int \mathbf{r}\rho(\mathbf{r})d^3r = -e\sum_j \langle\psi_j|\mathbf{r}|\psi_j\rangle = -e\sum_j \int \mathbf{r}\left|\psi_{n\mathbf{k}}(\mathbf{r})\right|^2 d^3r. \tag{3.38}$$

This results depends on where we place the origin of our coordinate system. It is clearly not applicable without further discussions. Another perspective on this issue is that the information required to compute the polarization is not contained directly in the charge density.

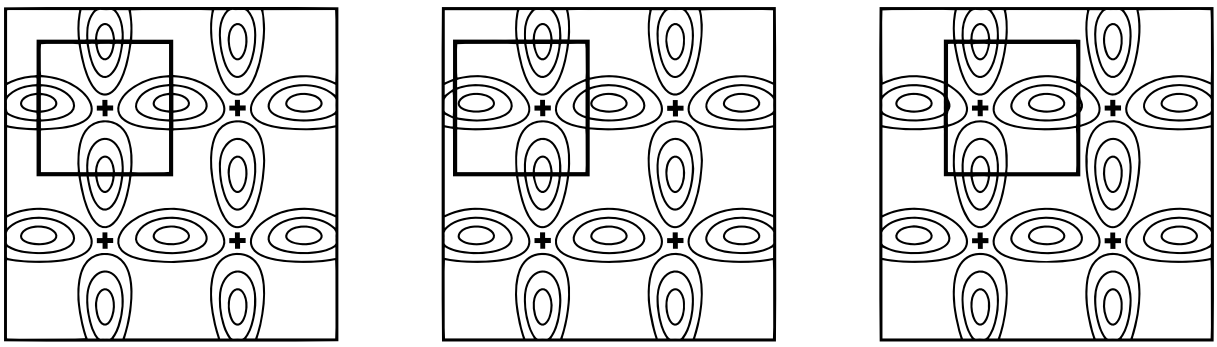

Figure 3.8: Nuclear charge (denoted by +) as delta-distributions and the electron charge density (contours) in a periodic cell. The figure illustrates the problem with defining the polarization using the charge density: In the left most panel the positive nucleis is centered in the unit cell, giving a net zero polarization. In the middle panel an equally large cell but now slightly shifted to the left gives a net polarization pointing to the right. Finally the panel to the right shows the unit cell slightly shifted to the right, giving a net polarization pointing to the left.

The solution to this problem came from starting with the current definition $\mathbf{J} = \frac{d\mathbf{P}}{dt}$ and by instead computing changes in geometrical phases of the Bloch functions $|\psi_{nk}\rangle = e^{i\boldsymbol{k}\cdot\boldsymbol{r}}|u_{nk}\rangle$. These changes are produced as we imagine driving the electrons across the entire Brillouin zone (BZ) in some virtual Sommerfeld modelling of charge displacement [140, 141].

Independent of the definition of the polarization, it must reflect the symmetry and periodicity of the system. This leads to the polarization being multi-valued, meaning the polarization is well defined only modulo a polarization quantum $\Delta_{\boldsymbol{P}} = e\mathbf{R}/V_0$, where $\mathbf{R}$ is any multiple of the lattice vectors $\boldsymbol{a}_{j=1,2,3}$. The polarization forms a periodic set called the polarization lattice, where each consecutive element is separated by $\Delta_{\mathbf{P}}$. To extract a prediction for the true spontaneous polarization $\mathbf{P}_s$ that can be compared to experiments, we must be careful to make the branch choice consistent. We will (borrowing from [140]) indicate this ambiguity using the symbol ":=" when the quantity is defined modulo a polarization quantum.

In the modern theory of polarization, $\boldsymbol{P}_{\mathrm{s}}$ is computed by treating the electron contribution as the change in the geometric or Berry phases $\bar{\theta}_{n,j}$ defined by the Bloch function description $|\psi_{nk}\rangle$.There is a Berry phase $\bar{\theta}_{n,j}$ for every band n and direction 'j'.As indicated by the overbar, each Berry phase is averaged over the $\boldsymbol{k}$-vectors in the other BZ directions. We concentrate on $\bar{\theta}_{n,j}$-differences introduced by a cyclic evolution of the system across the BZ. We need to compute such Berry phases at a sequence of distortions λ.

In practice, we generate a series of structural configurations, or distortions, that captures the transformation from λ_{i}, a non-polar reference state, to system of interest λ_{f}. Ignoring the details of the λ-path, the polarization becomes a two-point difference

$$\Delta\mathbf{P}_{\mathrm{i}\to\mathrm{f}} := \mathbf{p}\left(\lambda_{\mathrm{f}}\right) - \mathbf{p}\left(\lambda_{\mathrm{i}}\right), \tag{3.39}$$

which, as indicated, is defined exclusively modulo a polarization quanta.

In an insulating crystal, while nuclei can be approximated as discrete point charges, the electronic charge is distributed. However, we can still predict the spontaneous polarization as given by the Berry phases:

$$\mathbf{p}(\lambda) := \frac{e}{V_0}\left[\sum_{\mu} Z_\mu \boldsymbol{\tau}_\mu(\lambda) - \sum_{n}^{occ.}\sum_{j=1}^{3} \frac{\bar{\theta}_{n,j}(\lambda)}{2\pi}\mathbf{a}_j\right], \tag{3.40}$$

where Z_μ and $\boldsymbol{\tau}_\mu$ symbolize the charge and position of ion μ, respectively. The result in Eq. (3.40) is in fact, exclusively a point charge representation where the latter term is given by positions of (maximally localized) Wannier functions [142] $|w_{n\mathbf{R}}\rangle$. The evaluation of these are avilable in QE, and they are essentially a Fourier transform of the Bloch functions:

$$\begin{aligned} |w_{n\mathbf{R}}\rangle &= \frac{V_0}{(2\pi)^3}\int_{BZ} d^3\mathbf{k} e^{-i\mathbf{k}\cdot\mathbf{R}} |\psi_{n\mathbf{k}}\rangle, \\ &= \frac{V_0}{(2\pi)^3}\int_{BZ} d^3\mathbf{k} e^{i\mathbf{k}\cdot(\mathbf{r}-\mathbf{R})} |u_{n\mathbf{k}}\rangle. \end{aligned} \tag{3.41}$$

Again, the integration is over the BZ, and we note that $|u_{n\mathbf{k}}\rangle$ is periodic. The Wannier (charge) center $\bar{\boldsymbol{r}}_n$ can be computed using $\mathbf{r} = -i\frac{\partial}{\partial\mathbf{k}}$:

$$\begin{aligned} \bar{\mathbf{r}}_n &= \langle w_{n0}|\mathbf{r}|w_{n0}\rangle \\ &= \frac{V_0}{(2\pi)^3}\int_{\mathrm{BZ}} \langle u_{n\mathbf{k}} \mid i\nabla_{\mathbf{k}} u_{n\mathbf{k}}\rangle\, d^3k \\ &= \sum_j \frac{\bar{\theta}_{n,j}}{2\pi}\mathbf{a}_j. \end{aligned} \tag{3.42}$$

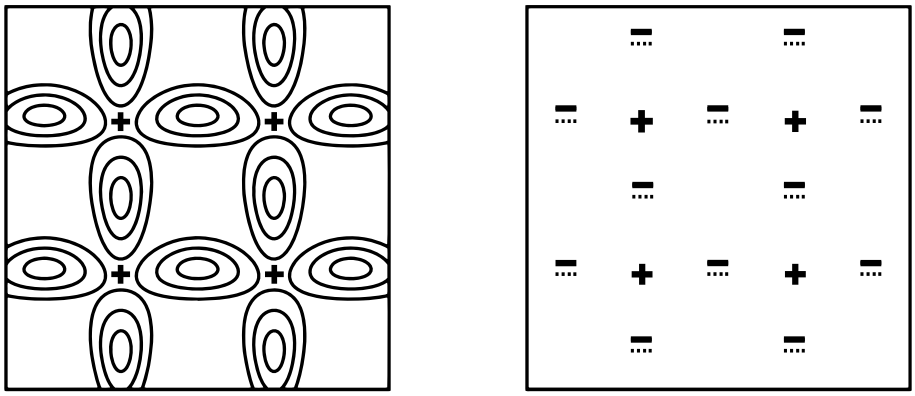

Figure 3.9: The modern theory of polarization mapping of the true electronic charge distribution in an isolating crystal (left) to a model system (right) where the electron charge clouds are replaced with point charges at the Wannier centers. We then compute the polarization in terms of the shift in the centers relative to those of a high-symmetry, non-polar, crystal configuration (illustrated by dotted line).

That is, each such Wanner center is explicitly given as a position in the unit cell determined by the $\bar{\theta}_{n,j}$ set. This brings us directly to a geometrical representation of the multi-valued spontaneous polarization at any given distortion:

$$\mathbf{p}(\lambda) := \frac{e}{V_0}\left[\sum_{\mu} Z_\mu \boldsymbol{\tau}_\mu(\lambda) - \sum_{n}^{\text{occ}} \bar{\mathbf{r}}_n(\lambda)\right]. \tag{3.43}$$

Figure 3.9 illustrates how the deformation ($\lambda_i \rightarrow \lambda_f$) causes a change in the offset between of nuclei and Wannier centers and in effect causes an increasing charge displacement. Eq. (3.43) provides a simple interpretation of spontaneous polarization in terms of these charge relocations.

We finally extract the prediction $\mathbf{P_s}$ for the spontaneous polarization, permitting comparison to experiments, as the difference in $\Delta\mathbf{P}_{\text{i}\rightarrow\text{f}}$ as described along the same branch of the polarization lattice:

$$\mathbf{P_s} = \Delta\mathbf{P}_{\text{i}\rightarrow\text{f}}|_{\text{same branch}}. \tag{3.44}$$

We note, however, that for an actual theory characterization we must model and track the Berry phase change along a physical transformation to be sure that we do in fact remain on the same branch in each and every evaluation of Eq. (3.43).

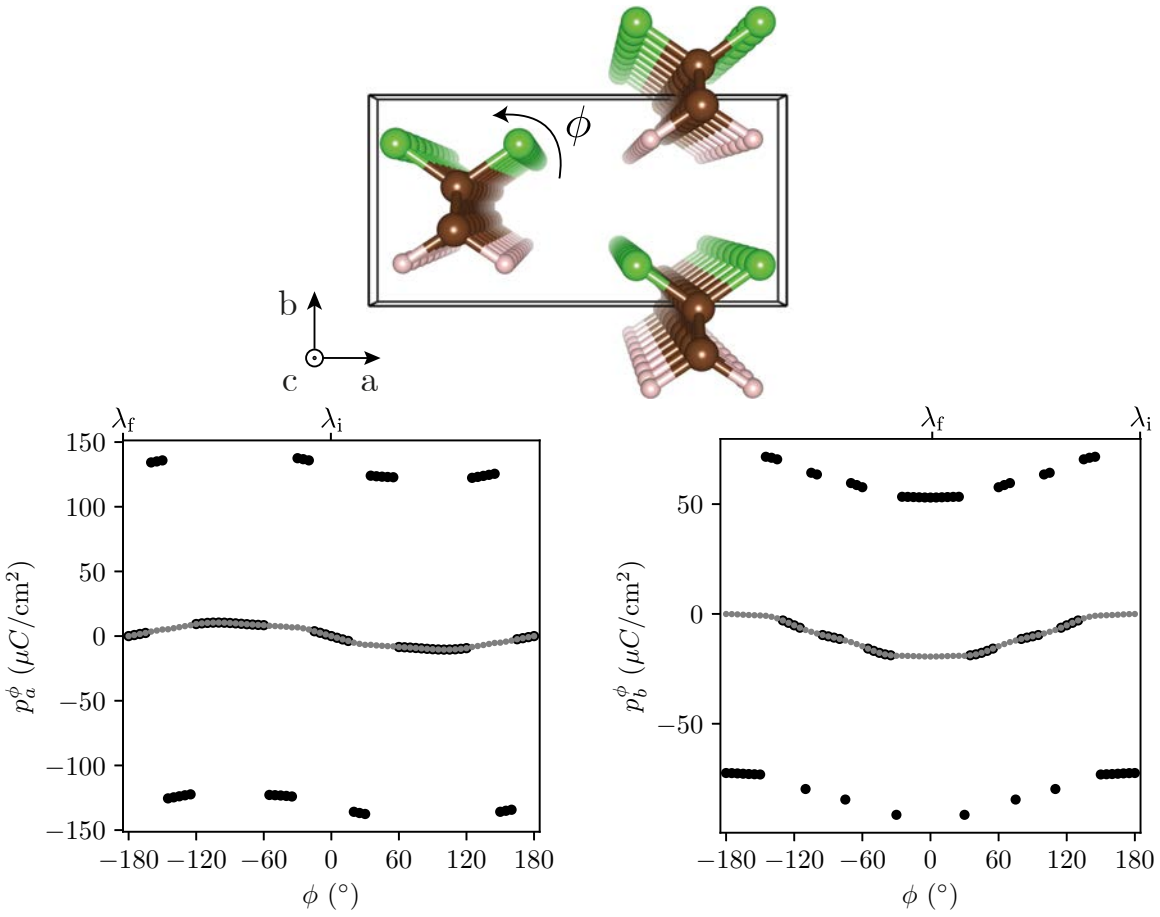

Figure 3.10: The procedure used to compute the spontaneous polarization of β-PVDF. In the top panel we show the deformation path used to map the relaxed structure to a symmetric reference state by rotating the left monomer. The lower two panels show the Berry phase values along the a-direction (left) and b-direction (right) as a function of the distortion parameter ϕ.

We exemplify the method using our results from **Paper B**. There we compute the spontaneous polarization of β-PVDF. The deformation path relevant in this analysis is illustrated in the top middle panel of Figure 3.10. In essence, we track the Berry phase along a distortion path, $\lambda(\phi)$, rotating the left monomer by some angle ϕ in the unit cell. The distortion takes a symmetric reference state λ_i, to the actual (and potentially) polar configuration λ_f. The Berry phase values along the a-direction and b-direction are presented in the lower left and right panels, respectively, of Figure 3.10. These values are plotted as a function of the distortion parameter ϕ. The black dots are the original Berry phase values, which clearly show the multi-valued nature of the Berry phase. In contrast, the grey dots are the Berry phase values after aligning them on the branch closes the origin. The spontaneous polarization along the each lattice parameter is computed as

$$P_{s,\mathbf{a}} = p_{\mathbf{a}}^{\phi=180} - p_{\mathbf{a}}^{\phi=0}, \tag{3.45}$$

$$P_{s,\mathbf{b}} = p_{\mathbf{b}}^{\phi=0} - p_{\mathbf{b}}^{\phi=180}. \tag{3.46}$$

Here $p_{\mathbf{a/b}}$ is the projection of the polarization, as computed in Eq. (3.40), onto a unit vector parallel to either **a** or **b**. The absolute values of Eq. (3.45) and (3.46) are then the theory predictions for β-PVDF.

Chapter 4

Case Studies and Functional Validation

This chapter presents a summary of various case studies to validate the tools and methods introduced in the previous chapter. The initial section is dedicated to benchmarking the thermophysical properties of materials using the AHCX and AHBR, with various mixing of Fock exchange, comparing with PBE and HSE.

Subsequent sections explore the application of AHCX and AHBR to more complex systems found in catalysis and enzymatic reactions. Specifically, we demonstrate the capability of AHCX and AHBR to characterize important charge transfer aspects in activation of molecular oxygen in biological and catalytic contexts.

The chapter ends with a detailed discussion on orthorhombic polymers and the complex soft matter challenge of polyvinyl fluoride (PVF). We re-apply our careful energy mapping with cross test, and we make predictions of the PVF response behaviour.

The structured validation approach helps in guiding the construction of methods and schemes towards their application in materials science, especially towards complex soft matter.

4.1 Thermophysical Properties and Validation of RSH vdW-DFs

We first return to the example of $BiMnO_3$ in Fig 1.4 from the introduction. In Table 4.1 we show the result of our all-in-one-structure-search calculation using our spin vdW stress-tensor implementation for this system. Here CX+U denotes the inclusion of Hubbard U corrections to the Mn d-orbitals, which can sometimes be important for the correct description of the electronic structure of this material. As can be seen from the table, the spin-vdW-DF stress tensor is able to predict the lattice constants with a high precision, giving a mean average error (MAE) of 0.05 Å compared to PBE's 0.11 Å. The CX+U actually has a slightly higher MAE of 0.08Å, and the CX functional's robustness in handling these spin-frustrated systems without the Hubbard U correction is noteworthy. It highlights the functional's inherent strength in predicting material properties.

In Figure 4.1 we show the energy and magnetization of BCC and FCC iron, in an effort to validate the performance of RSH functionals in predicting the correct phase of spin-polarized systems. Using circles for BCC and squares for FCC, we plot the energy with an opaque color (left axis) and the magnetization of the corresponding structure in translucent color (right axis). The results are compared to experimental values. All functionals

	PBE	CX	CX+U	Exper.
a [Å]	9.67	9.51	9.59	9.54
b [Å]	5.50	5.60	5.63	5.61
c [Å]	9.77	9.75	9.70	9.86
β [°]	108.9	108.3	109.2	110.7
V_0 [Å^3]	491.6	492.98	493.64	493.64

Table 4.1: Structural relaxation results for $BiMnO_3$ using different functionals: PBE, CX, and Hubbard corrected CX+U ($U = 3.5$), against experimental values. The lattice constants (a, b, c), monoclinic angle (β), unit cell volume are presented (V_0).

predict the BCC phase as the ground state, which is in agreement with experiments.

Looking at the quantitative results for iron in Table 4.2, we see that the HSE functional gives the most accurate results for the cohesive energy and bulk modulus. However, AHBR is only slightly worse, and the AHCX functional is the most accurate in predicting the equilibrium volume.

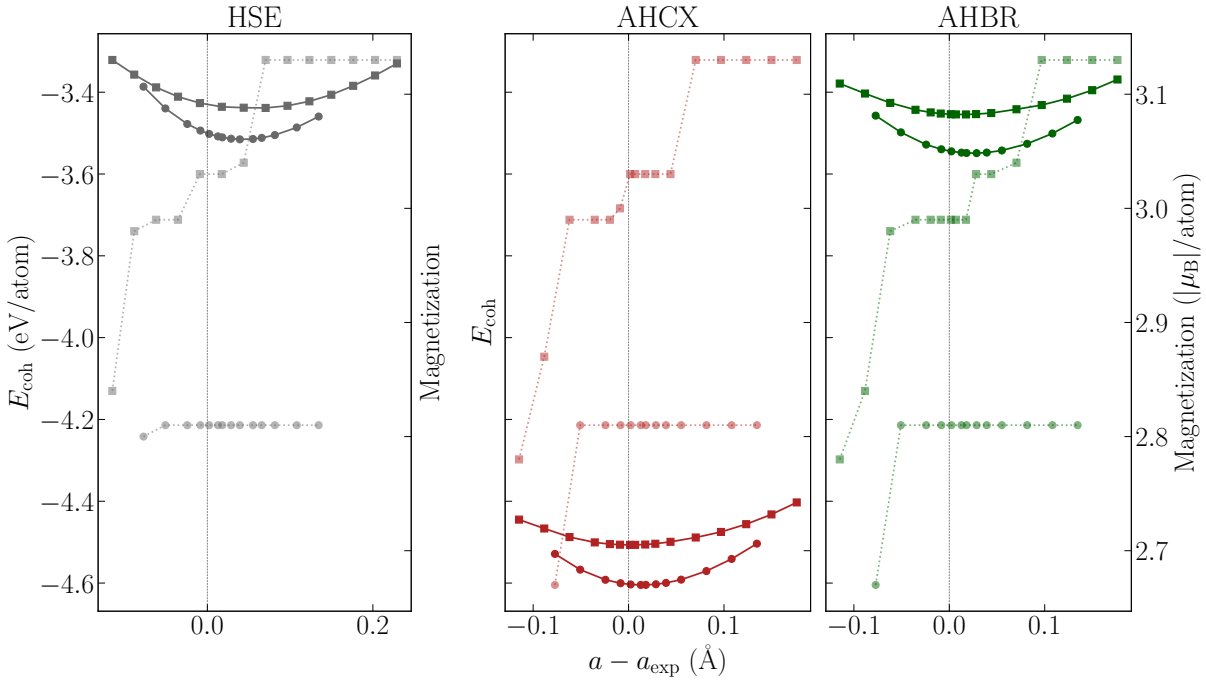

Figure 4.1: Energy (opaque) and absolute magnetization (translucent) for BCC (circles) and FCC (squared) iron, together with the fourth order fit in HSE06, AHCX and AHBR functionals.

In Table 4.3 we show numerical results that help us benchmark different functionals (PBE, HSE, CX, AHCX) for a range of transition metals of relevance in catalysis. The bulk modulus B_0 denotes characterizations obtained by the the lattice-parameter expansion approach, B_0^{BM} extracted by use of Birch-Murnaghan EOS that we use to cross-check our approach. The agreement in the bulk modulus between the two methods is, in fact, excellent. From the lattice constants we can also see that the AHCX functional gives the most accurate results overall, although the non-hybrid CX is a close contender.

In Figure 4.2 we show the statistics of benchmarking functionals for thermophysical

		HSE	AHCX	AHBR	Exp.
FCC	E_{coh}	3.44	4.51	3.45	-
	V_0	12.98	12.28	12.44	12.26
	B_0	142.31	154.48	154.45	-
BCC	E_{coh}	3.52	4.60	3.55	4.32
	V_0	12.13	11.80	11.99	11.64
	B_0	185.58	202.53	198.93	168.30

Table 4.2: Functional phase preference for iron in its FCC and BCC structures, with the cohesive energy (E_{coh} in ev/atom,, equilibrium volume (V_0 in $Å^3$), bulk modulus (B_0 in GPa), and critical pressure (P_{crit} in GPa) for each of the functionals, compared to experimental values. Based on the calculations plotted in Figure 4.1.

properties of 13 non-magnetic bulk materials. The figure shows the relative deviations in lattice parameters a, cohesive energies ΔE, and bulk moduli B_0 for the different functionals, as compared to experimental values back-corrected and adjusted fro thermal vibrational effects. The solids includes the transition metals of Table 4.3, some semiconductors, and some ionic insulators [49].

Figure 4.2 is a sum of all the functional benchmarking on bulk systems that I have been involved with, including the work behind **Paper A** as well as that towards launch of AHBR [47]. What immediately stands out is the performance of the non-hybrids CX and B86r, as compared to PBE and HSE. Both CX and B86r has a lower mean deviation in all properties compared to PBE, and both outperforms HSE in predicting cohesive energy.

Turning to the new vdW-DF hybrids, the performance of the original AHCX (at $\alpha = 0.20$) functional is outstanding. It has the lowest mean deviation in all properties of all the hybrids. AHCX also gives the smallest spread in the distribution of deviations for B_0 and ΔE, indicating a high precision in the predictions. The $AHCX_{0.25}$ functional also performs well, with a slightly higher mean deviation, apart from the lattice parameter where it is the best performing functional. AHBR functional has a slightly higher mean deviation than AHCX, but still outperforms HSE in all properties. Decreasing the Fock exchange fraction to 0.20 in $AHBR_{0.20}$ gives a slightly higher mean deviation in B_0 and a, but it still outperforms HSE on all properties.

	PBE	HSE	CX	AHCX	Exp*
Cu					
a_0 [Å]	3.639	3.638	3.576	3.587	**3.599**
E_{coh} [eV]	3.423	3.027	3.781	3.348	**3.513**
B_0 [GPa]	138.0	127.7	163.3	148.3	**144.3**
B_0^{BM} [GPa]	136.4	124.2	159.8	144.8	**144.3**
B'	5.34	5.56	5.19	5.43	**4.88**
Ag					
a_0 [Å]	4.156	4.145	4.065	4.078	**4.070**
E_{coh} [eV]	2.488	2.368	2.955	2.774	**2.964**
B_0 [GPa]	87.5	84.8	115.3	104.8	**105.7**
B_0^{BM} [GPa]	88.6	86.7	114.2	105.8	**105.7**
B'	6.17	5.83	6.14	6.12	**4.73**
Au					
a_0 [Å]	4.165	4.129	4.101	4.098	**4.067**
E_{coh} [eV]	2.997	2.917	3.634	3.440	**3.835**
B_0 [GPa]	137.4	148.5	170.5	167.8	**182.0**
B_0^{BM} [GPa]	136.1	146.8	167.2	165.5	**182.0**
B'	6.32	6.31	6.03	6.10	**6.40**
Pt					
a_0 [Å]	3.970	3.921	3.929	3.910	**3.917**
E_{coh} [eV]	5.434	4.811	6.226	5.524	**5.866**
B_0 [GPa]	248.5	281.1	284.0	297.7	**285.5**
B_0^{BM} [GPa]	246.6	277.1	282.0	293.0	**285.5**
B'	5.67	5.73	5.49	5.62	**5.18**
Rh					
a_0 [Å]	3.832	3.779	3.786	3.760	**3.786**
E_{coh} [eV]	5.565	4.384	6.367	5.244	**5.783**
B_0 [GPa]	257.6	297.1	295.8	312.7	**277.1**
B_0^{BM} [GPa]	249.8	291.6	289.0	308.0	**277.1**
B'	5.43	5.14	5.10	4.91	**4.5**

Table 4.3: Comparison of calculated lattice constants (a_0), cohesive energies (E_{coh}), zero-pressure bulk moduli (for the polynomial expansion B_0 and the BM EOS B_0^{BM}), and their pressure derivatives (B') for various metals using different functional methods (PBE, HSE, CX, AHCX) against experimental values (Exp*).

4.2 Cu-Chabazite and Enzymatic Crystals

In this section, we present the work of **Paper C**. It concerns my work to evaluate the ability of AHCX, $\mathrm{AHCX}_{0.20}$ and AHBR=$\mathrm{AHBR}_{0.25}$, and HSE+D3 to describe the activation and dissociation of O_2 in an enzymatic crystal and in a $[Cu_2(NH_3)_4O_2]^{2+}$ complex. The latter is related to a key step during low-temperature selective catalytic reduction of NOx over Cu-promoted CHA zeolites [35–40, 50]. The structural characteristics of the $[Cu_2O_2(NH_3)_4]^{2+}$ complex exhibits a local Cu_2O_2 configuration akin to the copper centers found in certain biological enzymes [143–145]. Notably, enzymes such as hemocyanins, tyrosinase, and catechol oxidase utilize copper dimers to activate molecular oxygen. These

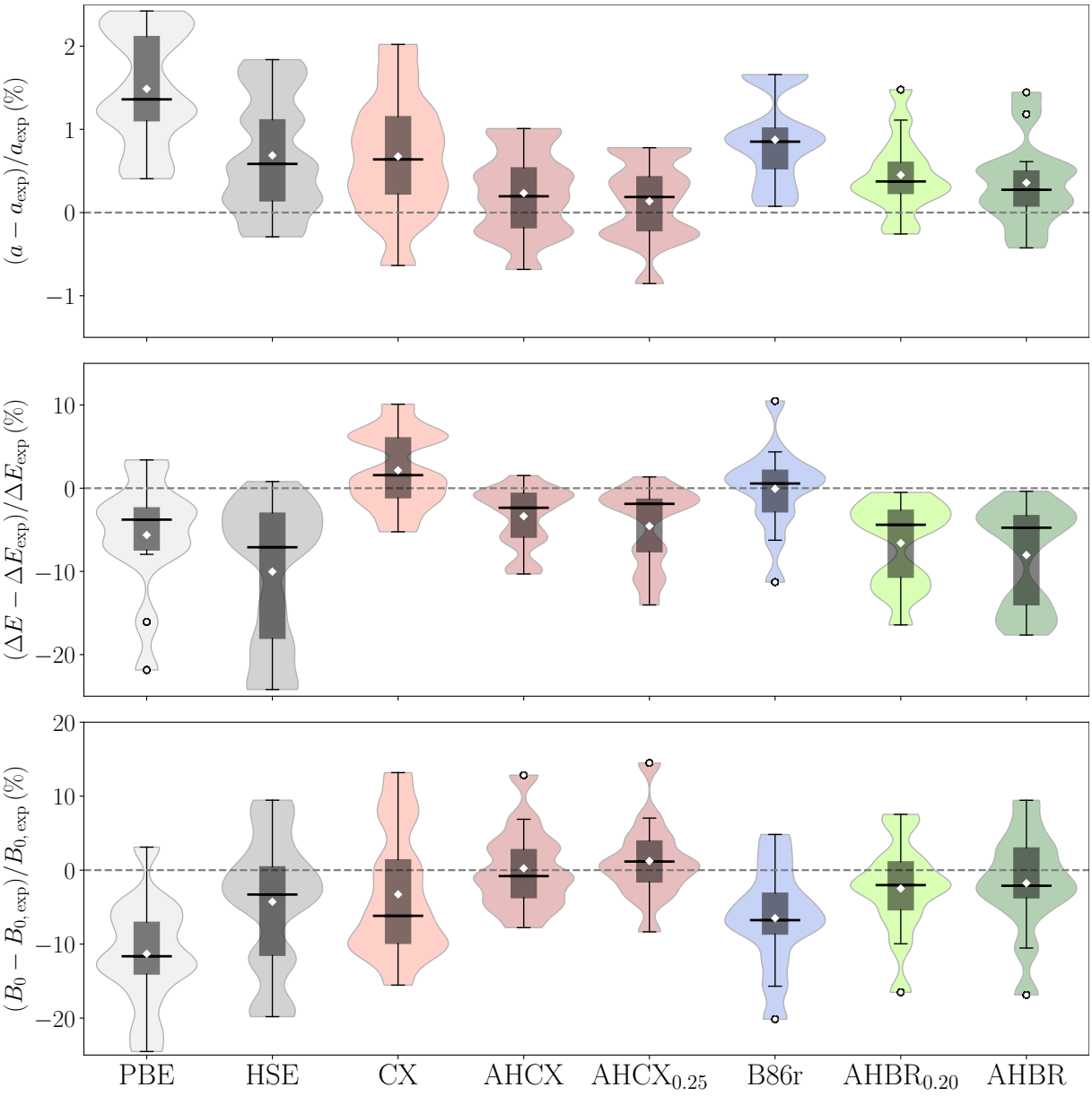

Figure 4.2: Violin plot representing statistics of relative deviations in PBE, HSE, CX, AHCX=AHCX$_{0.25}$, AHCX$_{0.25}$, B86r, AHBR$_{0.20}$, AHBR=AHBR$_{0.25}$ determinations of bulk lattice parameters (top), cohesive energies (middle), and bulk moduli (bottom panel). We compare with experimental values that are back-corrected for zero-point energy and thermal vibrational effects. The benchmarking comprised of 13 non-magnetic elements and compounds (1 simple and 5 transition metals, 4 semiconductors and 3 ionic insulators). In the violin plots, the white diamonds mark the mean deviation, the box identifies the range between the first and third quartile, and the black line indicates the median of the distribution. Whiskers indicate the range of data falling within 1.5*box-lengths of the box.

enzymatic structures have been replicated and analyzed using single crystal diffraction techniques [146]. Within such enzymes, the Cu_2O_2 motif displays variability in its structural arrangements, exemplified by the Side-on peroxo $[Cu_2^{II}(O_2^{2-})]^{2+}$ and the Bis(μ-oxo) $[Cu_2^{III}(O^{2-})_2]^{2+}$ configurations illustrated in Figure 1. The integrity of the O-O bond differs between these forms, remaining intact at approximately 1.4 Å in the side-on configu-

ration, while dissociating to about 2.3 Å in the bis-configuration. The complexes maintain a net charge of +2, with the copper ions in oxidation states 'II' and 'III', respectively. Moreover, the electronic configuration $3d^9$ in the side-on structure permits magnetic interactions, typically favoring anti-ferromagnetic coupling over ferromagnetic [147, 148].

Figure 4.3: Comparison of the investigated $[Cu_2^{II}(O_2^{2-})]^{2+}$ (side-on peroxo) and $[Cu_2^{III}(O^{2-})_2]^{2+}$ (bis(μ-oxo)) complexes, illustrating the intact and dissociated O-O bonds, copper oxidation states and their net charge. Ligands are denoted by L.

We examine the functionals' ability to depict the copper-oxygen interactions by computing the gas-phase CuO molecule in Table 4.4. The binding energy was derived from the energy disparity between the molecular state of CuO and its constituent copper and oxygen atoms, which were considered in doublet and triplet states, respectively. Experimentally, the CuO molecule is characterized by a dissociation energy of 2.79 eV, a bond length of 1.724 Å, and a harmonic wavenumber of 640.2 cm^{-1} [149].

Vibrational analysis is also conducted for CuO and $Cu^+(NH_3)_x$ complexes, with energies subsequently adjusted for zero-point corrections. In the case of the CuO molecule we illustrate the process in Figure 4.4. The vibrational frequency is determined by calculating the total energy as a function of the Cu-O bond length. We calculate the harmonic vibrational frequency, denoted as ω_e, using a harmonic approximation to the potential energy curve. Anharmonic vibrational effects are evaluated by solving the Schrödinger equation for the molecular potential energy surface. Corrections for anharmonicity, $\omega_e x_e$, are then extracted from the second-order perturbative expansion of the potential energy curve:

$$E(n) = \omega_e \left(n + \frac{1}{2}\right) - \omega_e x_e \left(n + \frac{1}{2}\right)^2. \tag{4.1}$$

For the $(CuNH_3)_x$ complexes, we apply vibrational corrections using the CX-functional as computed by the `ph.x` module of the QE suite. These corrections are consistently employed across all other functionals. Bader charge analysis is completed using algorithm developed by Henkelman et al [150].

To incorporate effects of ligand interactions on the Cu-O bond, we examine the $Cu^+(NH_3)_x$ series (x = 1-4) as as seen in Figure 4.5. We compare to kinetic energy measurements during collision-induced dissociation of $Cu^+(NH_3)_x$ with xenon of Walter and Armentrout [151]. The functionals' bond dissociation energies for the series is computed as

$$\mathrm{E_{BDE}}(x) = \mathrm{E}(Cu^+(NH_3)_{x-1}) + \mathrm{E}(NH_3) - \mathrm{E}(Cu^+(NH_3)_x). \tag{4.2}$$

Functional BDE predictions, together with the experimental findings as dashed lines, are presented in Figure 4.6. All functionals reproduce the experimental trend with a higher bond dissociation energy for $Cu^+(NH_3)_2$ as compared to $Cu^+(NH_3)$ and a clearly lower bond dissociation energies for the third and forth NH_3-ligand. The computational results are generally within 0.15 eV of the experimental values. However, CX underestimates

Table 4.4: Comparison of calculated binding energy (E_{bind}) and average Cu-O bond length ($\bar{d}_{Cu-O}$) for the CuO dimer using different exchange-correlation functionals. The computational results are obtained with QE besides the two cases explicitly noted VASP.

Functional	E_{bind} (eV)	$\bar{d}_{Cu-O}$ (Å)	ω_e (cm^{-1})	$\omega_e x_e$ (cm^{-1})	Cu (e)	$\lvert\boldsymbol{P}\rvert$ (D)
CX	-3.26	1.70	703	22	0.57	4.08
CX (VASP)	-3.42	1.69	721	13	0.51	-
B86R	-3.25	1.70	692	11	0.56	4.00
HSE+D3	-2.66	1.74	623	8	0.59	4.56
HSE+D3 (VASP)	-2.73	1.74	626	9	0.56	-
$AHCX_{0.20}$	-2.75	1.72	645	10	0.58	4.42
$AHCX_{0.25}$	-2.64	1.73	633	14	0.59	4.51
AHBR	-2.61	1.73	622	4	0.58	4.45
Exp.[149]	-2.79	1.72	640.2	4.43	-	4.57

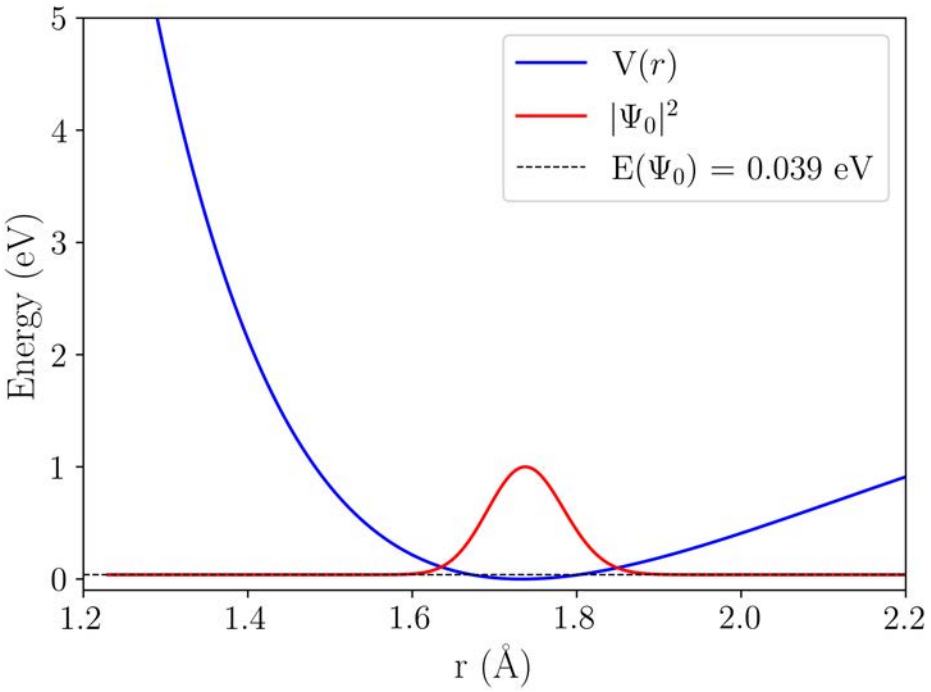

Figure 4.4: Solution to the one-dimensional time-independent Schrödinger Equation (1D TI-SE) for the Cu-O system in the potential $V(r)$ (blue curve) as generated by the AHBR functional as a function of the separation (bond distance) r. The probability density of the ground state $|\Psi_0|^2$ is shown in red. The dashed line indicates the energy level of the ground state, $E(\Psi_0) = 0.039$ eV. The calculated root-mean-square deviation of the position, $\sqrt{\langle \Delta x^2 \rangle}$, is 0.046 Å, and the frequency, ν, is 621.7 cm^{-1}.

the bond dissociation energies for $Cu^+(NH_3)$ and HSE+D3 does not reproduce the higher bond dissociation energy for $Cu^+(NH_3)_2$ as compared to $Cu^+(NH_3)_1$. The issue with HSE+D3 was recognized also in a previous computational study using VASP [40].

Metalloproteins with di-copper centers capable of binding oxygen have been synthe-

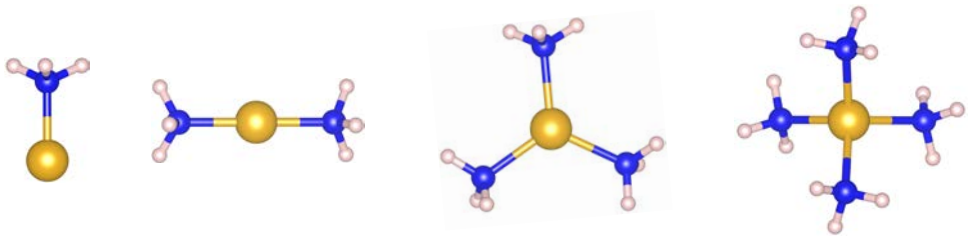

Figure 4.5: Progression of copper-ammonia complexes in the $Cu^{+}(NH_3)_x$ series, showcasing varying numbers of ammonia ligands (x = 1 to 4). Copper is represented by yellow spheres, nitrogen by blue, and hydrogen by white.

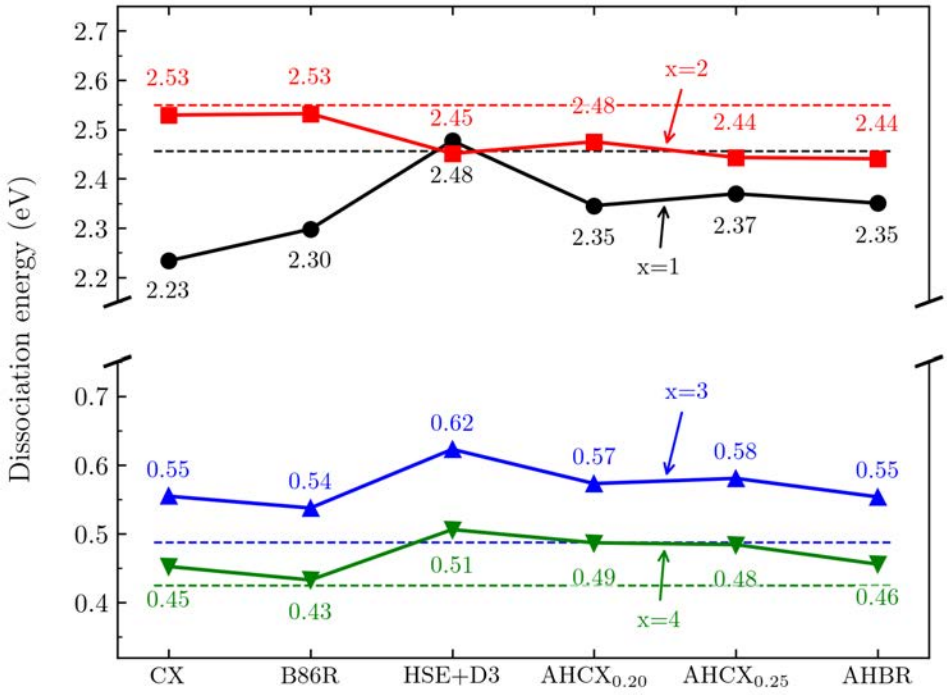

Figure 4.6: Comparison of sequential bond dissociation energies for $Cu(NH_3)_x{}^{+}$for the studied functionals against experimental values (dashed lines) [151].

sized in both bis and side-on configurations, influenced by the ligand type. Our study focus on the complex 1,4,7-iPr-1,4,7-triazacyclodecane (iPr3TACD/peroxo), seen in the bottom row of Figure 4.7. The investigated enzymatic sytem features two units of $[Cu_2O_2(N_3C16H35)_2]^{2+}, (B(C_6H_5)_4{}^{-})_2$ in a side-on configuration as determined by single crystal diffraction [143–146].

The results of the structural relaxation of the iPr3TACD crystal using the CX functional are presented in Table 4.5. We compute the energy difference between the bis and side-on configurations in Table 4.6, using the CX relaxed iPr3TACD crystal. While the CX functional favors the bis configuration by 0.34 eV, the hybrid functionals demonstrate a clear preference for the side-on configuration. The affinity for side-on structures under hybrid functionals correlates with antiferromagnetic coupling of $3d^9$ electronic configurations in the copper atoms, critical for stabilizing the ground state singlet configuration observed in both structural types. Notably, $AHCX_{0.20}$'s prediction of a configuration without magnetic moments highlights the challenge of accurately modeling the delocal-

ized character of these states.

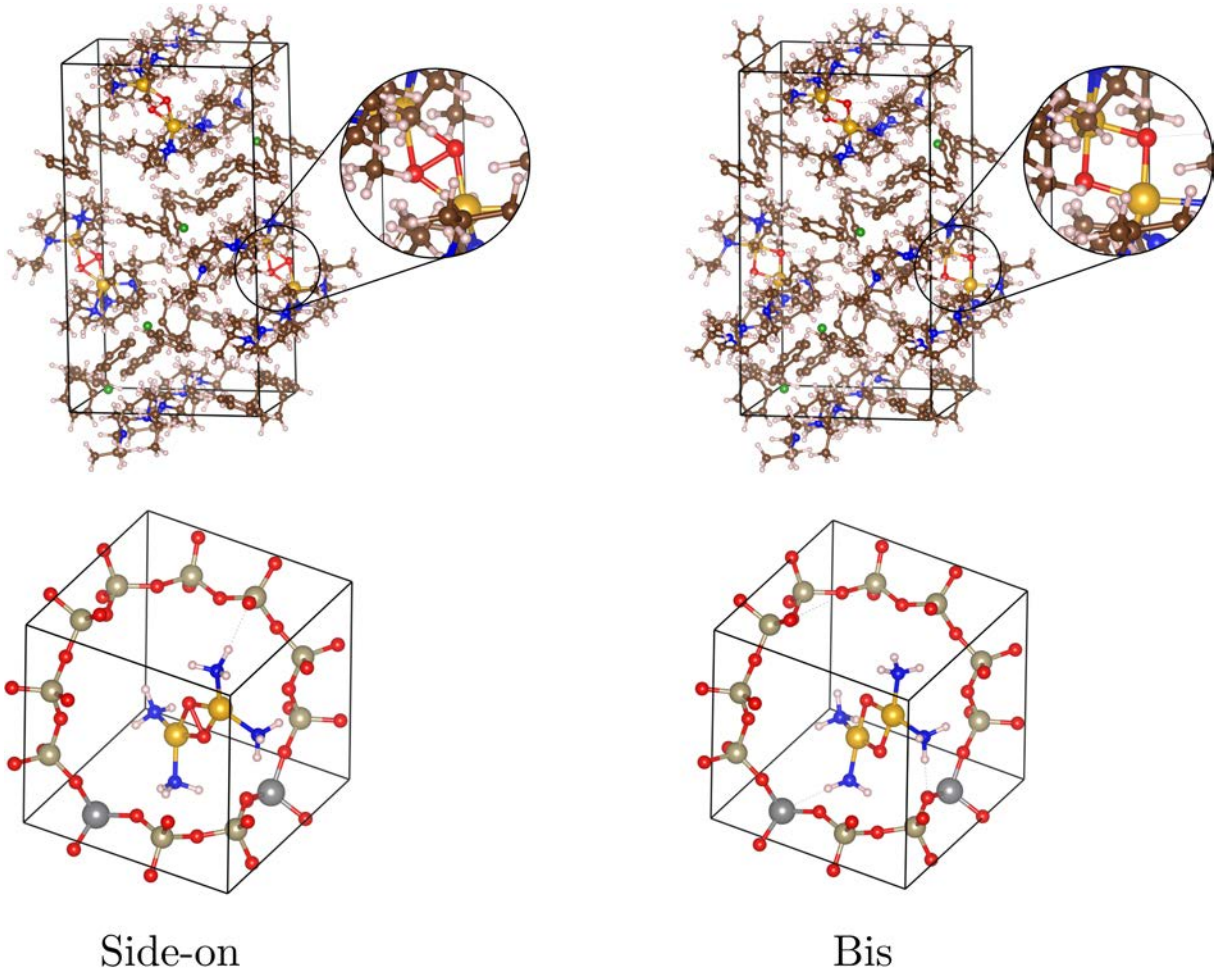

Figure 4.7: Unit cells and configurations of embedded Cu_2O_2 complexes in chabazite (top row) and iPr3TACD (bottom row) environments. The left column shows Side-on configurations, while the right column displays Bis configurations of Cu_2O_2. Chabazite hosts a single unit, and iPr3TACD features two units.

	Structure	CX	Experiment[146]
d_{Cu-Cu}	bis	2.86	-
	side-on	3.57	3.52
d_{Cu-O}	bis	1.82	-
	side-on	1.93	1.89
d_{O-O}	bis	2.25	-
	side-on	1.48	1.37
$\phi\,(^\circ)$	bis	173	-
	side-on	173	172

Table 4.5: Structural parameters of the iPr3TACD crystal relaxed using the CX functional, compared with experimental data.

Finally, we turn to the computational study of $[Cu_2O_2(NH_3)_4]^{2+}$ complex, an intermediate in the NH_3-SCR process at low temperatures within CHA zeolites. As illustrated in

	Structure	CX	HSE+D3	$AHCX_{0.20}$	$AHCX_{0.25}$	AHBR
ΔE	bis	0	0	0	0	0
	side-on	0.34	-0.43	0.06	-0.58	-0.58
μ	bis	0	0	0	0	0
	side-on	0	0.85	0	0.83	0.83

Table 4.6: Functional predictions of energy differences (ΔE) and absolute magnetic moments (μ) for bis and side-on configurations of the Cu_2O_2 unit embedded in the iPr3TACD crystal. We report ΔE in eV and μ in μ_B per copper atom.

the bottom panel of Figure 4.7, we specifically analyzed the side-on peroxo $[Cu_2(O_2^{2-})]^{2+}$ and bis(μ-oxo) $[Cu_2(O^{2-})_2]^{2+}$ configurations. Due to its weak, non-directional interactions with the zeolite framework, the complex exhibits a potential energy surface with multiple shallow minima. The experimentally observed side-on peroxo structure features Cu-Cu and Cu-O bond lengths of 3.40 ± 0.05 Å and 1.911 ± 0.009 Å, respectively, supporting a bent geometry with a Cu-O-O-Cu torsion angle close to 150°.

Fixed-cell relaxations are shown in Table 4.7, employing VASP and QE calculations in CX together with HSE+D3, and PBE+U+D3. The calculations indicate a functional-dependent preference for the molecular configuration; CX favors the bis configuration, while HSE+D3 and PBE+U+D3 show a lower energy preference for the side-on structure. Interestingly, all functionals predict a singlet state with zero magnetic moment for the bis structures, whereas the side-on configuration is predicted to be a singlet state. However, the side-on exhibits distinct electronic characteristics across the functionals: no magnetic moment in CX, and approximately 0.5 μ_B in HSE+D3 and PBE+U+D3, suggesting anti-ferromagnetic coupling and localized d^9 configurations in the latter two. This difference underscores the sensitivity of magnetic coupling between Cu atoms to d-electron localization. Further, the structural parameters like O_2 bond lengths and Cu-Cu distances align closely with experimental findings [152]. We note that torsion angles in the side-on configuration are significantly affected by the degree of electron localization, with lower angles indicating more bent structures in line with localized electron models.

Functional	**Complex**	ΔE	μ	ΔE_{TS} (eV)	d_{Cu-Cu} (Å)	d_{O-O} (Å)	ϕ (°)
CX (QE)	bis	0	0	-	2.715	2.328	169
	side-on	0.352	0	1.09	3.509	1.482	173
CX (VASP)	bis	0	0	-	2.731	2.329	173
	side-on	0.32	0	0.46	3.517	1.487	176
HSE+D3 (VASP)	bis	0	0	-	2.705	2.292	174
	side-on	-0.46	0.53	0.13	3.512	1.462	157
PBE+U+D3 (VASP)	bis	0	0	-	2.731	2.296	175
	side-on	-0.30	0.48	0.07	3.481	1.481	146

Table 4.7: Analysis of the completely structurally optimized bis(μ-oxo) and side-on peroxo structures in CHA. ΔE is the energy difference between the two structures (eV). μ is the absolute magnetic moment on one Cu atom (μ_B), ΔE_{TS} is the energy difference between the singlet and triplet state of the side-on structure (eV). d_{Cu-Cu} and d_{O-O} are the distances between Cu-Cu and O-O, respectively (Å). ϕ (°) is the Cu-O-O-Cu torsion angle of the Cu_2O_2 complex.

Using the CX relaxed structure, we analyze the RSH vdW-DFs ability to describe the

complex, as seen in Table 4.8. The side-on structure is preferred for all RSHs, except for $AHCX_{0.20}$ indicating that the amount of Fock-exchange in that case is too small. The bis-structure is again a fully-spin-balanced delocalized singlet with zero magnetic moment. The hybrid descriptions for the side-on structure gives an antiferromagnetic ground state configuration with an absolute magnetic moment of about 0.7 μ_B. The magnetic moment is higher than for the VASP calculation in Table 4.7 and previous calculations using HSE+D3 (VASP) [40]. The magnetic moment is slightly lower for $AHCX_{0.20}$, which is a consequence of the lower degree of d^9 localization. The difference between the triplet and singlet states for the side-on configuration is for all hybrid calculations about 0.5 eV. The value is higher for the CX functional. Note that the singlet ground state of the side-on structure for CX is spin-balanced, without any magnetic moment on the Cu ion.

The interaction energy of the $[Cu_2O_2(NH_3)_4]^{2+}$ complex within the CHA framework, due to non-local correlation effects, was computed as:

$$\Delta E_c^{\mathrm{nl}} = E_c^{\mathrm{nl}}(\mathrm{system}) - E_c^{\mathrm{nl}}(\mathrm{CHA}^{2-}) - E_c^{\mathrm{nl}}(\mathrm{Cu_2O_2(NH_3)_4}]^{2+}). \tag{4.3}$$

We calculate the non-local correlation energy separately for the entire system, the isolated CHA cage, and the gas phase $Cu_2O_2(NH_3)_4]^{2+}$ complex. Considering the presence of two aluminum sites in CHA, it bears a double negative charge. In Table 4.8, we present the computed non-local correlation embedding energies for the charged and neutral fragments. We note that the vdW-dominated embedding energy is larger for the side-on structure than the bis structure for the vdW-functionals, whereas it is smaller for HSE+D3. The systematics of the difference suggests that the (hybrid) vdW-DFs has advantages because they consistently use the same electron-gas foundation to predict all types of binding contributions.

Functional	**Structure**	ΔE	μ	ΔE_{TS}	$E_{\mathrm{embed}}^{\mathrm{c,nl}}$	$E_{\mathrm{embed}}^{\mathrm{c,nl}}$(neutral)
CX	bis	0	0	-	-2.178	-2.429
	side-on	0.352	0	1.094	-2.524	-2.445
HSE+D3	bis	0	0	-	-1.889	-2.168
	side-on	-0.324	0.76	0.540	-1.818	-2.124
$AHCX_{0.20}$	bis	0	0	-	-2.408	-2.427
	side-on	0.010	0.64	0.553	-2.482	-2.422
$AHCX_{0.25}$	bis	0	0	-	-2.400	-2.428
	side-on	-0.155	0.74	0.558	-2.468	-2.419
AHBR	bis	0	0	-	-1.688	-1.562
	side-on	-0.201	0.73	0.560	-1.739	-1.682

Table 4.8: Functional preference and characterization of the Bis and Side-on structures in CHA using the structure calculated in CX. ΔE denotes the energy difference between structures, μ represents the magnetic moment per Cu atom, ΔE_{TS} measures the singlet-triplet state energy difference for the side-on structure, and $E_{\mathrm{embed}}^{\mathrm{c,nl}}$ quantifies the non-local correlation component of the embedding energy for charged or neutral fragments.

Figure 4.8 reports spatial mappings of the binding by non-local correlation. As such the figure panels pinpoint the origins of the dispersion interactions and tracks the impact of charge transfer between the $[Cu_2O_2(NH_3)_4]^{2+}$ complex and the CHA cage. The mappings of binding correspond to CX studies and are provided under the correct/incorrect assumption that individual fragment is charged/neutral, in the left/right panel. The most

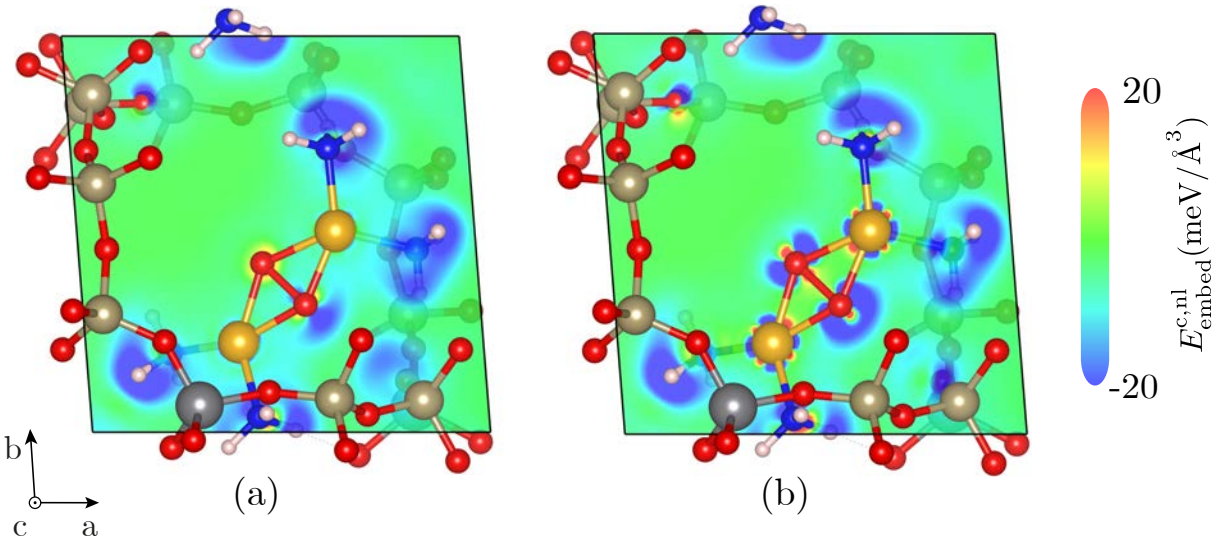

Figure 4.8: Non-local correlation binding energy density $\Delta e_c^{\mathrm{nl}}(\boldsymbol{r}) = E_{\mathrm{embed}}^{\mathrm{c,nl}}$ (Eq. (3.32)) computed in CX for charged fragments (left) and neutral fragments (right).

substantial contributions to the ΔE_c^{nl} binding arise in both cases from the NH_3 ligands, though contributions from one of the oxygen atoms is also important.

The role of complex charging is significant. The non-local correlation binding $\Delta e_c^{\mathrm{nl}}(\boldsymbol{r})$, for the neutral complex (right panel) is larger at the oxygen because the charge transfer goes from the complex to the zeolite, and under the actual conditions (left panel) the O has lost some electrons. The integrated ΔE_c^{nl} for the case with neutral fragments is -2.44 eV, which shows that the changes in the charge distribution has a clear effect on the magnitude of vdW-interaction.

This detailed analysis underscores the advantage of employing a (hybrid) vdW-DF XC-functional because it captures the effects of electronic charge redistribution in it's description of vdW forces. This is essential for achieving a balanced description of the competition between strong chemical bonds, weaker non-local correlation interactions and steric hindrance. Also, the vdW-attraction could be exaggerated if over-delocalization of Cu $3d$ is not prevented. For this problem we clearly need both the generic vdW-DFs ability to reflect the charge transfer impact on vdW forces and the hybrid ability of to counteract electron density errors [47, 49]. It is gratifying that the RSH vdW-DFs AHCX and AHBR delivers a description of the catalytic copper-oxide system that is generally consistent with the limited experimental data that exist.

4.3 Polymers

Here we present the results of our study of distinctly soft matter from **Paper A** and **Paper D**: orthorhombic polymers, specifically polyethylene (PE), polyvinyl fluoride (PVF), and β-polyvinylidene fluoride (PVDF), as depicted in the unit cell illustrations in Figure 4.9. Building on the work of Olsson et al. [153], this study extends the capabilities of the CX-functional to predict polymer structures accurately. PE and PVDF are widely studied and exhibit a strong correlation between experimental and computational findings, thus providing a reliable foundation for validating our computational approaches [9, 154, 155]. Conversely, the structure of PVF remains less understood due to discrepancies in experimental data, positioning it as a complex soft matter problem [127, 156].

Fluorinated polymers like PVDF and PVF are derived from monomers of vinyl fluoride (CH_2=CHF) and vinylidene fluoride (CH_2=CF_2), respectively, and are notable for their distinct structural, reactive, and dielectric properties [13, 157, 158]. The substitution of hydrogen atoms with fluorine in the polymer backbone imparts significant changes in properties compared to PE. These polymers exhibit enhanced thermal and mechanical stability and can be utilized in diverse applications including fuel cells, capacitors, and electromechanical sensors [159–165].

A critical aspect of these polymers is their polarizability, especially notable in PVDF, which show considerable spontaneous polar responses due to the asymmetric inclusion of fluorine atoms [9, 154, 155, 166–169]. The polarizability in these polymers not only depends on their crystalline atomic structure but also on the contributions from metastable variants that are close in cohesive energy and compatible with the ground state structure. This characteristic makes the detailed study of their structure and properties essential for technological applications and theoretical understanding.

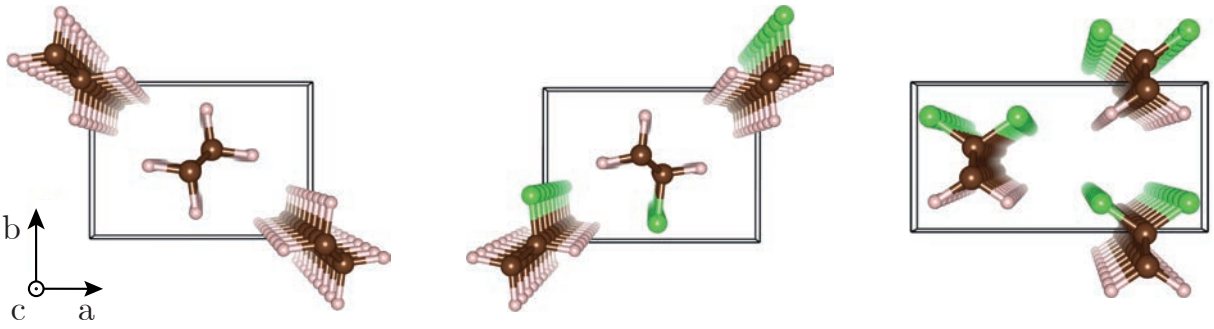

Figure 4.9: Unit cells of orthorhombic polymers studied in **Paper A**and **Paper B**: From left to right, polyethylene (PE), polyvinyl fluoride (PVF), and β-polyvinylidene fluoride (PVDF). The sequence illustrates increasing fluorination; starting with the non-fluorinated PE, substitute one hydrogen atom by a fluorine atom on one of the carbon atoms in the monomer to form PVF. In β-PVDF, all remaining hydrogen atoms on the same carbon are substituted with fluorine atoms.

4.3.1 Structure

We optimize the unit-cells of the polymers using the CX-functional and the results are presented in Table 4.9. The table contains the optimal lattice parameters as predicted

using both a variable-cell relaxation and the energy mapping method from section 3.4, denoted in the table as stress and mapping respectively. CX predicts the lattice parameters of PE with a mean relative deviation (MRD) of 1.9% using the stress- and 1.8% using the mapping method. For β-PVDF the MRD is 1.4% using both methods. The close agreement between the stress- and mapping-methods indicates that the CX-functional is robust for predicting the lattice parameters of polymers. With this high accuracy, we conclude that the CX-functional is well suited for predicting the lattice parameters of polymers. This gives us confidence in the CX-functional's ability to predict the possible structures of PVF, as necessitated by the fact that there is no experimental consensus on the unit cell parameters. In section 3.2, we discuss how we use CX to find the lowest-lying motifs of PVF based on a set of initial guesses. The last part of Table 4.9 shows the unit-cell for the ground state (GS) and the first and second excited states (ES1 and ES2) of PVF.

Table 4.9: Table of calculated lattice parameters for PE, all values in Å. We contrast presently calculated results with both experiments and previous calculations [153] that used different pseudopotentials and a smaller k-points sampling. Here-provided results are denoted 'map' ('stress') when obtained by the robust constrained-stress-optimization+map (potentially unsafe, but carefully controlled, full-stress) strategy for motif validation (motif search). Additional parameters for PVDF and PVF along with experimental values are included [125, 133].

PE			
Type	a_0	b_0	c_0
CX[153]	7.218	5.024	2.553
Exp.[170]	7.121	4.851	2.548
Exp.[171]	7.161	4.866	2.546
Exp.[172]	7.388	4.929	2.539
Exp.[173]	7.420	4.960	–
CX map	7.144	5.044	2.552
CX stress	7.155	5.032	2.552
β-PVDF			
x-ray diffraction[125]	8.47	4.90	2.56
x-ray diffraction[133]	8.58	4.91	2.56
CX map[h]	8.581	4.763	2.575
CX stress[9]	8.579	4.758	2.575
CX stress	8.581	4.752	2.575
PVF			
GS stress	7.260	5.178	2.556
GS map	7.267	5.181	2.556
ES1 stress	7.192	5.272	2.556
ES1 map	7.194	5.274	2.556
ES2 stress	7.341	5.169	2.556
ES2 map	7.346	5.170	2.556

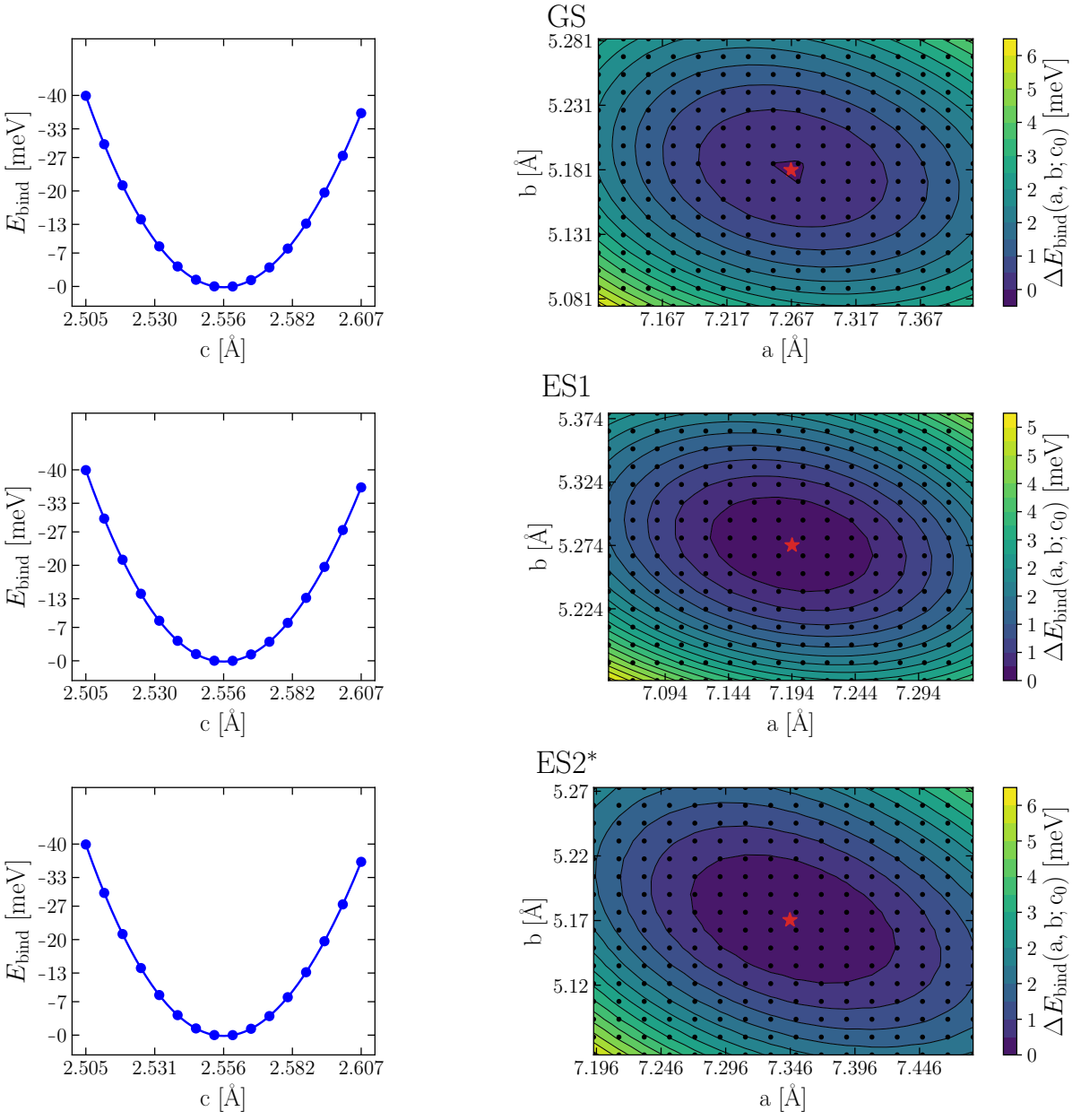

Figure 4.10: Energy mapping of the three low-lying structures of PVF, illustrating their cohesive-energy values and validation through constrained-stress optimization. In the left panels, the variation in binding energy for the motif is depicted through constrained-stress unit cell optimization, facilitating identification of the optimal along-chain unit-cell dimensional c_0. The right panels exhibits contours of the binding-energy variation $\Delta E_{\mathrm{bind}}(a, b; c_0)$ as a function of assumed unit-cell dimensions a and b, interpolated between atomic relaxation calculations (black dots), with the red star marking the validated a_0 and b_0 values predicted using variable cell relaxation method.

In Figure 4.10, we present the energy mapping of the three lowest-lying structures of PVF. As we can see from the figure, and Table 4.9 the GS, ES1 and ES2 are close in structure (and energy). All of the energy surfaces seem to be relatively flat, with the GS having a slightly more pronounced minimum.

Table 4.10: Functional estimations of lattice parameters for γ-PVDF, as computed by variable-cell relaxation. The experimental characterization was made on a sample containing a mixture of the up and down γ-phase at T = 300 K. The unit cell is essentially orthorhombic, with a small tilt of the along-chain axis c and the $a-b$ basis plane.

Functional	a[Å]	b[Å]	c[Å]	V_0[Å^3]	$\angle ac$[°]
$\boldsymbol{\gamma_d}$ Phase					
vdW-DF1	9.41	5.08	9.50	454.97	90.0
vdW-DF2	9.17	4.99	9.43	431.90	90.2
CX	9.31	5.02	9.60	449.28	90.0
$\boldsymbol{\gamma_u}$ Phase					
vdW-DF1	9.60	4.98	9.31	444.32	96.5
vdW-DF2	9.34	4.86	9.31	421.42	96.0
CX	9.36	4.84	9.32	421.81	94.6
Exper.[a]	9.67	4.96	9.20	440.65	93

[a] Ref. [174]

To further validate the CX functional, we compare the lattice parameters of the γ-phases of PVDF with experimental values in Table 4.10. CX predicts the lattice parameters of the γ_d and γ_u phases with a total deviation of 2.7% from the experimental values. vdW-DF1 and vdW-DF2 predict the lattice parameters with a deviation of 1.8% and 2.4%, respectively.

4.3.2 Spontaneous Polarization

Figure 4.11 presents the polarization calculations of the three lowest-lying PVF structures. As we discussed in the last paragraph of section 3.5, we compute the polarization along the rotation angle ϕ as we rotate one of the monomers between the predicted structure to a reference structure. The black dots represent the computed polarization values, many of them pertaining to branches outside the scale of the figure. The spontaneous polarization, analogous to a hysteresis measurement, is the difference in polarization between the two structures, see Eq. (3.45) and (3.46). To make sure this difference is taken along the same branch, we map the computed value by some number of the so called polarization quanta, to the branch closest to the origin.The adjusted 'same-branch' variation is shown by the grey dots. The results of the spontaneous polarization computation are presented in Table 4.11.

The structures are symmetric along the a-axis, and we expect the polarization to be zero along this axis. From Figure 4.11 we find that along the a-axis, the polarization is close to zero for all three structures. Since the structures are symmetric for $\varphi = 0°$ as well as $\varphi = 180°$ the polarization lattice is symmetric around 0. We ascribe this to the errors introduced by the mapping, and set the polarization along the a-axis to zero.

Parallel to the b-axis, the spontaneous polarization should be non-zero only for ES2* due to it's asymmetry along the b-axis. This is also what we get from the Berry-phase

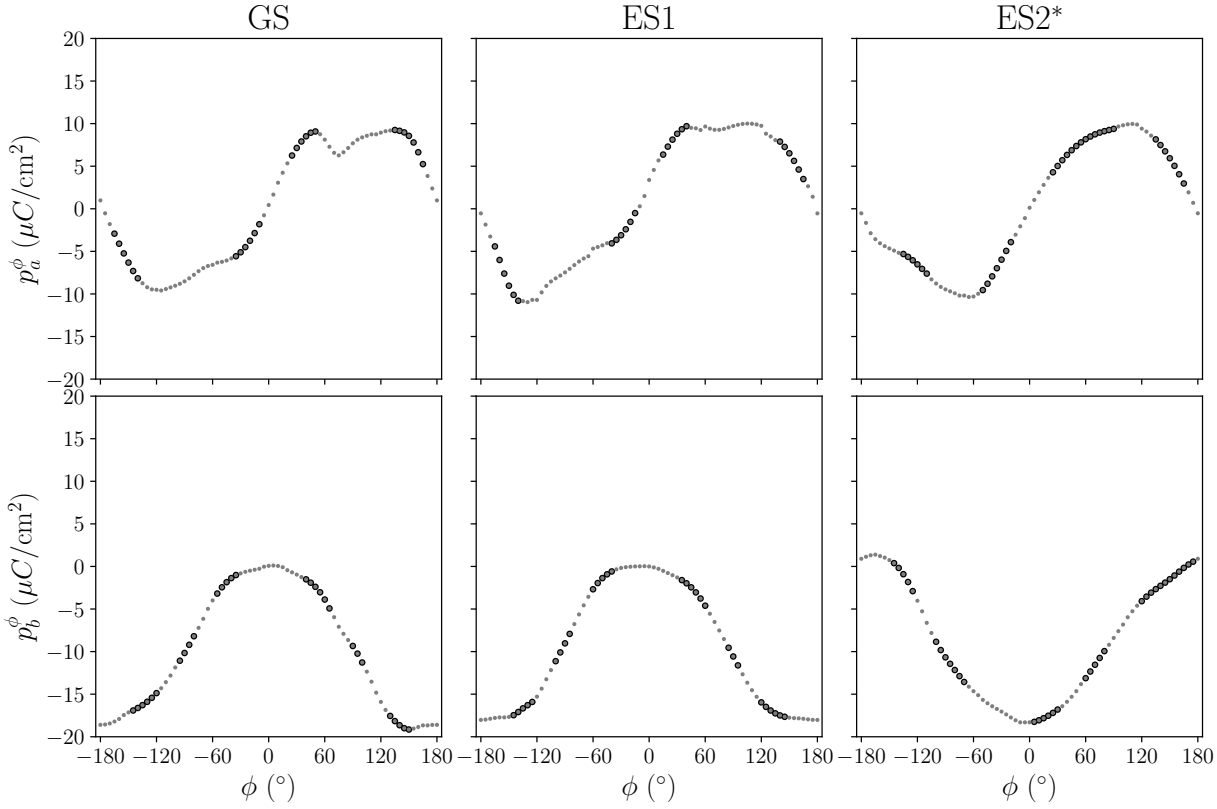

Figure 4.11: Polarization calculations for the three lowest-lying PVF structures along the rotation of one of the monomer chains. The top row shows the polarization along the a-axis, while the bottom row shows the polarization along the b-axis. The rotation takes the predicted structure ($\phi = 0°$) to a neutral reference structure ($\phi = 180°$) — apart from the b-axis case for GS and ES1 where the opposite is true. The black dots represent the computed polarization values, while the grey dots are the values mapped to the branch closest to the origin.

calculations, as shown in Table 4.11. For the GS and ES1 structures the relaxed configuration is symmetrical we can directly conclude $|P_{s,\mathbf{b}}| = 0$.

Spontaneous polarization parallel to the b-axis should be non-zero exclusively for ES2*, because of the asymmetry in atom position when viewed along this axis. This is consistent with polarization calculations, as indicated in Table 4.11.

Table 4.11: Spontaneous polarization, P_s (in μC cm^{-2}), along the a- and b-axes for the three lowest-energy motifs of PVF as predicted using CX. The final row shows our prediction of the spontaneous polarization for a macroscopic sample of PVF as computed by a thermal average at room temperature.

	$\lvert P_{s,\mathbf{a}}\rvert$	$p_a^{\phi=0}$	$p_a^{\phi=180}$	$\lvert P_{s,\mathbf{b}}\rvert$	$p_b^{\phi=0}$	$p_b^{\phi=180}$
GS	0	0.4	1.0	0	0.1	−18.6
ES1	0	3.4	−0.5	0	0.0	−18.0
ES2*	0	0.1	−0.5	19.2	18.3	0.9
$\langle P\rangle_{T=293\,\mathrm{K}}$	~ 0			5.7		

In the last row of Table 4.11 we show the estimation of the spontaneous polarization of a macroscopic sample of PVF by averaging the polarization of the low-energy conformers

(GS, ES1, and ES2) at room temperature. The results show that the polarization for PVF, along b-axis, is potentially non-zero and in the range of 5.7 μC cm^{-2}.

Calculating the polarization of β-PVDF in CX without considering the effects of low-energy conformers, as presented in **Paper A**, yields a polarization of 40 μC cm^{-2}. When compared to the experimental measurements $\sim$ 10 μC cm^{-2} [167], it is evident that interphase interactions and the potential presence of oppositely aligned β-phase domains results in a significantly lower polarization in a macroscopic sample.

At the same time it is clear that PVF cannot even under ideal room temperature conditions match the promise of β-PVDF as a flexible piezoelectric material.

4.3.3 Plastic Deformation

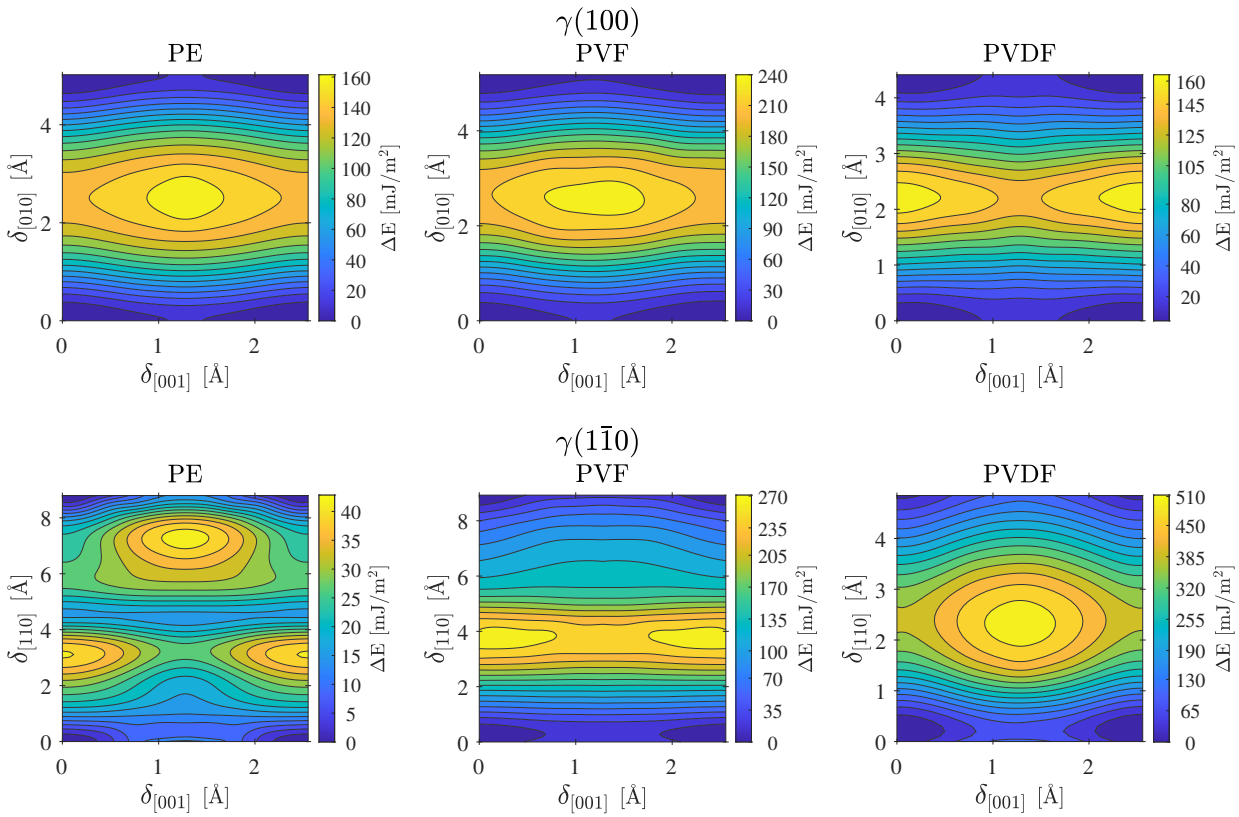

Figure 4.12: γ-surfaces or the generalized stacking fault energy (GSFE) for a set of deformations δ along the (100) and (1$\bar{1}$0) planes for the GS structure of PVF, PE and β-PVDF. The GSFE is computed as the energy difference between the GS and the deformed structure, normalized by the area of the slip plane. The slip displacement $\delta_{[hkl]}$ represent a fraction of the relative unit-cell displacement, see section 3.4, Figure 3.6, and Figure 3.7 for details. The data for PE γ-surface was taken from a coauthor, in Ref. [153].

In Figure 4.12 we compare the shear resistance of the three polymers by analyzing the changes in binding energy per unit cell and general stacking fault energy (GSFE) across different slip planes, see section 3.4 for details. The horizontal axis represents chain slip and the vertical axis corresponds to transverse slip. We note that the γ-surfaces are periodic, making all corners equivalent

We find that chain slips are typically associated with lower energy barriers. The study of local chain orientations adjacent to the shearing planes shows that chains interact in a

consistent manner during transverse slip, leading to analogous GSFE profiles as depicted in Figure 4.12. A similar analysis of $(1\bar{1}0)$-PE, $(1\bar{1}0)$-PVF, and (100)-PVDF highlights comparable structural traits that suggest equivalent slip mechanisms. However, only PE exhibits local minima on its GSFE surface, which potentially facilitates dislocation dissociation in this material [153].

The GSFE surfaces indicated a gradual increase in barrier heights when hydrogen in PE is replaced with fluorine in PVF and PVDF. This suggest a structural stiffening effect of fluorination. The energy barriers indicate that fluorination increases the resistance to chain slip: in the (100)-slip plane the energy barriers associated with chain slip correspond to 12, 18 and 17 mJ/m^2 (corresponding to 9, 15 and 13 meV per modeling super cell) for PE, PVF and PVDF, respectively.

Furthermore, the analysis revealed that the appearance and behavior of the (100)-GSFE surfaces for PE, PVF, and $(1\bar{1}0)$-PVDF on the plane are significantly influenced by the local chain orientations. Between PE/PVF and PVDF there is a shift of saddle point and maximum by (1/2)[001]. This PE/PVF versus PVDF difference follows from the fact that in PE and in PVF, the neighbouring chains are rotated by approximately 90°, while they are aligned for β-PVDF.

Chapter 5

Conclusions and Outlook

5.1 Summary of Findings

This thesis presented tools and methods aimed at developing and validating computational methodologies within the framework of Density Functional Theory; focusing particularly on the application to complex soft matter.

Applications in Hard and Soft Materials

The implementation of the vdW-DF spin-stress tensor within QE in **Paper A**has enabled precise predictions in spin-polarized vdW systems. We demonstrate the effective and predictive power of the spin-stress tensor using CX to accurately predict physical properties of magnetic metals and a multiferroic perovskites ($BiMnO_3$). We also show that AHCX enhances the accuracy in descriptions of magnetic elements such as iron compared to CX.

This study also includes the first of the thesis example applications of the vdW-DF method on a truly soft matter system, using CX to predict structure and ferroelectric response of polyvinylidene fluoride (PVDF).

Development and Validation of the vdW-DF-ahcx Functional

The introduction of the range-separated hybrid vdW-DF called AHCX in **Paper B** represents an advancement to vdW-inclusive DFT. The AHCX functional, integrating truly non-local correlation and exchange within the electron-gas framework, extends the consistent-exchange vdW-DF-cx (CX) and offers a systematic approach to the treatment of electron interactions over varying distances. Using the computational scheme we developed for validation of thermophysical properties, we demonstrate that AHCX provides superior accuracy compared to traditional HSE in predicting lattice constants, cohesive energies, and bulk moduli of cubic bulk materials.

Further, **Paper B**reports a survey of AHCX's accuracy in modeling molecular properties. We find that it surpasses the performance of the HSE+D3 combination for molecular systems. We also show that AHCX reliably predicts work functions and surface energies for metals such as copper, silver, and gold, as well as accurately predicting the CO site

preference for adsorption energies on metals, proving its utility in understanding surface phenomena.

Studies on Zeolite and Enzymatic Crystals

In **Paper C**, we applied AHCX and the RSH vdW-DF2-ahbr (AHBR) functionals to a series of catalysis problems, specifically focusing on the characterization of activated oxygen within a $[Cu_2O_2]$ unit. We studied systems with the unit embedded within both Cu-Chabazite zeolites and enzymatic crystal structures, as well as examined gas-phase CuO dimers and $Cu(NH_3)_x$ complexes to gain comparative insights.

The RSH vdW-DFs, demonstrates clear advantages in understanding the intricate behaviors of the Cu_2O_2 structures. These functionals afford the unique capability to model both chemical and physical bonds simultaneously, without the need for semi-empirical adjustments. They therefore provide a more robust and theoretically consistent framework for tackling complex catalytic systems. The approach also enhances our ability to predict and manipulate the chemical activity, paving the way for advanced applications.

Investigation of Fluorinated Polymers

In the final **Paper D**, we utilized CX to explore the orthorhombic phases of PVDF and polyvinyl fluoride (PVF), focusing particularly on determining the ground state structure of PVF. This investigation culminated in the successful identification of a probable orthorhombic ground state for PVF that closely resembles the β-phase of PVDF.

We also characterized and predicted key properties of its ground state, including cohesive energy, lattice constants, elastic properties, and overall polarizability. These calculations employed ensemble averages of the lowest energy motifs, yielding insight on the potential macroscopic properties of PVF samples. The comprehensive studies led to the conclusion that, even under ideal conditions, PVF is unlikely to match the superior ferroelectric properties exhibited by the closely related β-phase of PVDF systems.

Additionally, **Paper D** explores the plastic slip deformation modes in both PVF and PVDF by calculating the generalized stacking fault energy γ. Analysis of γ in terms of DFT-energy components is crucial for understanding the mechanical behavior under deformation. An qualitative analysis was conducted compare the barriers for slip in the ground states of PVF and PVDF, including a comparisons with polyethylene (PE) for a broader perspective on the effects of flourination on the mechanical properties of these materials. Finally, we investigated the role of non-local correlation and gradient corrections to exchange in the slip barriers of PVF. This sheds light on the nature of the interactions that govern the mechanical properties of these materials.

5.2 Tools and Methods

Open-Source Software

We chose to implement and release the new RSH vdW-DFs and the spin-stress tensor in QE. We believe that by committing implementations of new computational tools within open-source computational software like the QE suite [51–53], and the ASE [175]/pymatgen [176] libraries, researchers can collectively help propel advancements in the field of computational materials science. Much like scientific progress is typically based on collaborations, the development of computational tools benefits from the collaborative nature of open-source ecosystems.

The modular architecture of open-source DFT code suites [177–183] allows researchers to develop and integrate specialized modules, inheriting existing functionality for easy extension. There are module integration for calculating vibrational properties, for simulations of materials in solutions and under the influence of external electric fields, among others. These tools extend DFT to more realistic environmental conditions. The tools are already giving us, the researchers, an ability to model biochemistry systems [28], electrochemical interfaces [184–186] and reactions in solutions [187, 188].

By incorporating new tools into a well-established framework like QE, we hope to benefit from standardized approaches to solving material science problems. This standardization supports reproducibility and comparability among different studies, which are critical for the validation of methods, tools and the field as a whole.

Finally, open-source software such as QE offers exceptional flexibility, empowering users to tailor their computational environment to specific project requirements. Users can select from a variety of pseudopotentials and directly modify the XC functional parameters within the input files, when appropriate. This adaptability is invaluable for testing and benchmarking new functionals, as it allows us to easily implement changes on the fly and compare results for different PPs and functionals.

Tools, Schemes and Scripts

The RSH vdW-DF functionals launched in the work of this thesis are derived from first-principles behaviour of the electron gas and a coupling constant analysis. AHCX and AHBR provide a theoretically robust alternative to deal with vdW systems without relying on ad-hoc methods and corrections, like an empirical setting of a Hubbard U parameter, or on externally defined vdW-corrections like D3. Our hybrids may be computationally expensive, just as all hybrids are, but their ab-initio design secure what seems (so far) to be significant accuracy gains and thus practical value through their predictive power for challenges in complex soft matter systems. They can help us screen materials for better performance. We believe that our results have further underscored the potential of the long-standing ab-initio Chalmers-Rutgers development program.

In this thesis work we also utilized extensive Python coding for automation and analysis of thermophysical properties, based on a formal lattice parameter expansion. Here we again managed to stay clear of empirical methods, avoiding the use of standard EOS fitting procedures. Additionally, the use of libraries such as ASE and Pymatgen was integral in managing and interfacing with DFT calculators. Streamlining the workflow and enhancing the efficiency of simulations performed using QE and VASP. With the use

of Python, we created detailed schemes for the determination of the ground state structure of PVF, automating the process of mapping out the structural details and response properties of soft matter polymers.

Most of the workflow and analysis code we created will be shared through the code-sharing platform GitLab to encourage collaboration and reproducibility of the work. I hope this will be a resource for the community, especially for newcomers to the field of computational materials science.

Finally, we attempted to clarify the theoretical and practical details of the Modern Theory of Polarization, using the Berry phase to predict the spontaneous polarization of PVF and PVDF systems. In practice the Berry phase analysis requires careful consideration of the reference state, choosing a non-polar reference configuration to assure that the polarization calculation gives physically meaningful results. The complexities associated with interpreting the results appropriately stems not only from the multi-valued nature of the polarization but there is also a modelling need. Specifically we need to find a related but completely symmetric configuration from which we can still transform (in our case via rotation of one of the chains) back to the actual polymer isomer. Of course, one also needs to make sure to converge the system, especially with respect to the k-point mesh, to ensure the integration over the BZ is accurate.

5.3 Perspectives

I end this thesis by considering some future perspectives on potential directions for further research, informed by the insights I have garnered through our work. My perspective on possibilities reflects my interests in both deepening our understanding of fundamental phenomena and advancing practical applications in materials science:

1. **Refinement of Ground-State Analysis of PVF:** The exploration of the configuration space in predicting the ground states of PVF could benefit from extension with more advanced computational strategies. Techniques such as minima hopping, genetic algorithms (GAs), and particle swarm optimization (PSO) represent promising methods for navigating the complex landscape of meta-stable states. Furthermore, apart from using our own intuition in guessing possible motifs, the integration of machine learning and diffusion models [189] could provide an extension to our database of potential ground-state structures. Finally, I would be interested in checking whether a switch to a RSH vdW-DF impacts the description of the plastic deformation.

2. **Development of Hybrid van der Waals Density Functionals:** The potential expansion of hybrid vdW-DFs that incorporate the long-range part of the Fock exchange poses an opportunity for enhancing the RSH's description of electronic structures. However, we take a cautious approach to maintain a manageable number of hybrid functionals. We believe that ensuring that each functional is robust across a variety of material systems, maintaining a balance between accuracy and ab-inition arguments, makes for a more reliable and user-friendly approach. Flooding the already vast landscape of functionals with even more choices, based on detailed optimization for specific problems, is not in line with the philosophy of the Chalmers-Rutgers vdW-DF approach.

3. **Integration of Machine Learning with van der Waals Density Functional (vdW-DF):** The adoption of machine learning potentials could integrate the accuracy of vdW-DF DFT calculations within molecular dynamics simulations. Allowing for large simulations of polymer-surface interactions and provide a pathway to more accurately model large systems where dispersion forces are critical. This approach could lead to large improvements in the predictive capabilities of computational methods, particularly in complex soft-matter systems.

4. **Improving Open Science Practices:** I believe the future of materials science research could be accelerated by fostering a tradition around the sharing of code and data. While substantial discourse on this topic exists, continuous emphasis on open science practices is important for improving reproducibility and especially for facilitating a more collaborative research environment.

Bibliography

[1] Richard P. Feynman, Robert B. Leighton, and Matthew Sands. *The Feynman Lectures on Physics, Vol. I: The New Millennium Edition: Mainly Mechanics, Radiation, and Heat*. Basic Books, (1963).

[2] R. Comes, M. Lambert, and A. Guinier. The chain structure of $BaTiO_3$ and $KNbO_3$. *Solid State Communications*, **6**:715–719, (1968).

[3] K. A. Müller and W. Berlinger. Static critical exponents at structural phase transitions. *Phys. Rev. Lett.*, **26**:13–16, (1971).

[4] Ronald E. Cohen. Origin of ferroelectricity in perovskite oxides. *Nature*, **358**: 136–138, (1992).

[5] Adrien Perrichon, Erik Jedvik Granhed, Giovanni Romanelli, et al. Unraveling the ground-state structure of bazro3 by neutron scattering experiments and first-principles calculations. *Chemistry of Materials*, **32**:2824–2835, (2020).

[6] K. Berland, C. A. Arter, V. R. Cooper, et al. van der Waals density functionals built upon the electron-gas tradition: Facing the challenge of competing interactions. *J. Chem. Phys.*, **140**:18A539, (2014).

[7] Erik Jedvik Granhed, Anders Lindman, Carin Eklöf-Österberg, et al. Band vs. polaron: vibrational motion and chemical expansion of hydride ions as signatures for the electronic character in oxyhydride barium titanate. *J. Mater. Chem. A*, **7**: 16211–16221, (2019).

[8] Erik Jedvik Granhed, Göran Wahnström, and Per Hyldgaard. $BaZrO_3$ stability under pressure: the role of non-local exchange and correlation. *Phys. Rev. B*, **101**: 224105, (2020).

[9] Carl M Frostenson, Erik Jedvik Granhed, Vivekanand Shukla, et al. Hard and soft materials: putting consistent van der waals density functionals to work. *Electronic Structure*, **4**:014001, (2022).

[10] Paul J. Flory. *Principles of Polymer Chemistry*. Cornell University Press, Ithaca, New York, (1953). 688 pp. Illus.

[11] A. Ravve. *Principles of Polymer Chemistry*. Springer New York, (2012).

[12] Michael Rubinstein and Ralph H. Colby. *Polymer Physics*. Oxford University Press, Oxford, (2003). pp 440.

[13] E. Leivo, T. Wilenius, T. Kinos, et al. Properties of thermally sprayed fluoropolymer pvdf, ectfe, pfa and fep coatings. *Progress in Organic Coatings*, **49**:69–73, (2004).

[14] Robert J. Young and Peter A. Lovell. *Introduction to Polymers*. CRC Press, (2011).

[15] Yi-Yang Peng, Shruti Srinivas, and Ravin Narain. Chapter 2 - nature and molecular structure of polymers. In Ravin Narain, editor, *Polymer Science and Nanotechnology*, 1 page. Elsevier, (2020).

[16] S. Ebnesajjad and P.R. Khaladkar. *Fluoropolymer Applications in the Chemical Processing Industries: The Definitive User's Guide and Databook*. Elsevier Science, (2004).

[17] Manas Chanda. *Introduction to polymer science and chemistry*. CRC Press, Boca Raton, FL, (2006).

[18] W.D. Callister and D.G. Rethwisch. *Materials Science and Engineering: An Introduction, 8th Edition*. Wiley, (2009).

[19] J. Bernstein. *Polymorphism in Molecular Crystals*. International Union of Crystallography monographs on crystallography. Clarendon Press, (2002).

[20] G.R. Desiraju, J.J. Vittal, and A. Ramanan. *Crystal Engineering: A Textbook*. Crystal Engineering: A Textbook. World Scientific, (2011).

[21] H.G. Brittain. *Polymorphism in Pharmaceutical Solids*. ISSN. CRC Press, (2018).

[22] Tonatiuh Rangel, Kristian Berland, Sahar Sharifzadeh, et al. Structural and excited-state properties of oligoacene crystals from first principles. *Phys. Rev. B*, **93**:115206, (2016).

[23] Joel Bernstein. ***Polymorphism In Molecular Crystals*** 14. Oxford University Press, (2002).

[24] Sarah L. Price. Predicting crystal structures of organic compounds. *Chem. Soc. Rev.*, **43**:2098–2111, (2014).

[25] Anthony M. Reilly, Richard I. Cooper, and et al. Report on the sixth blind test of organic crystal structure prediction methods. *Acta Crystallographica Section B Structural Science, Crystal Engineering and Materials*, **72**:439–459, (2016).

[26] Lars Goerigk, Andreas Hansen, Christph Bayer, et al. A look at the density functional theory zoo with the advanced GMTKN55 database for general main group thermochemistry, kinetics and noncovalent interactions. *Phys. Chem. Chem. Phys.*, **19**:32184, (2017).

[27] Clare Aubrey-Medendorp, Matthew J. Swadley, and Tonglei Li. The polymorphism of indomethacin: An analysis by density functional theory calculations. *Pharmaceutical Research*, **25**:953–959, (2007).

[28] Samuel Andermatt, Jinwoong Cha, Florian Schiffmann, and Joost VandeVondele. Combining linear-scaling dft with subsystem dft in born–oppenheimer and ehrenfest molecular dynamics simulations: From molecules to a virus in solution. *Journal of Chemical Theory and Computation*, **12**:3214–3227, (2016). PMID: 27244103.

[29] Anna Helena Mazurek, Łukasz Szeleszczuk, and Dariusz Maciej Pisklak. Periodic DFT Calculations—Review of Applications in the Pharmaceutical Sciences. *Pharmaceutics*, **12**:415, (2020).

[30] Brian W Matthews. Protein crystallography and drug discovery: recollections of knowledge exchange between academia and industry. *Journal of International Union of Crystallography*, **5**:428–438, (1988).

[31] Martin Karplus and John Kuriyan. Molecular dynamics and protein function. *Proceedings of the National Academy of Sciences*, **102**:6679–6685, (2005).

[32] Joseph Kraut. How do enzymes work? *Science*, **242**:533–540, (1988).

[33] Hans Frauenfelder, Stephen G Sligar, and Peter G Wolynes. The energy landscapes and motions of proteins. *Science*, **254**:1598–1603, (1991).

[34] Dagmar Ringe and Gregory A Petsko. Mapping enzyme catalysis through the protein structure database. *Proceedings of the National Academy of Sciences*, **82**:5040–5044, (1985).

[35] Lin Chen, Ton V. W. Janssens, Peter N. R. Vennestrøm, et al. A complete multisite reaction mechanism for low-temperature nh3-scr over cu-cha. *ACS Catalysis*, **10**: 5646–5656, (2020).

[36] Xueting Wang, Lin Chen, Peter N. R. Vennestrøm, et al. Direct measurement of enthalpy and entropy changes in nh3 promoted o2 activation over cu-cha at low temperature. *ChemCatChem*, **13**:2577–2582, (2021).

[37] Yingxin Feng, Xueting Wang, Ton V. W. Janssens, et al. First-Principles Microkinetic Model for Low-Temperature NH_3-Assisted Selective Catalytic Reduction of NO over Cu-CHA. *ACS Catal.*, 1 page, (2021).

[38] Yingxin Feng, Ton V. W. Janssens, Peter N. R. Vennestrøm, et al. The role of H^+- and Cu^+-sites for N_2O formation during NH_3-scr over cu-cha. *The Journal of Physical Chemistry C*, **125**:4595–4601, (2021).

[39] Yingxin Feng, Derek Creaser, and Henrik Grönbeck. Simplified kinetic model for NH_3-scr over cu-cha based on first-principles calculations. *Topics in Catalysis*, **66**: 743–749, (2022).

[40] Lin Chen, T. V. W. Janssens, and Henrik Grönbeck. A Comparative Test of Different Density Functionals for Calculations of NH_3-SCR over Cu-Chabazite. *Phys. Chem. Chem. Phys.*, **21**:10923–10930, (2019).

[41] J. P. Perdew, K. Burke, and M. Ernzerhof. Generalized gradient approximation made simple. *Phys. Rev. Lett.*, **77**:3865–3868, (1996).

[42] K. Berland and P. Hyldgaard. Exchange Functional That Tests the Robustness of the Plasmon Description of the van der Waals Density Functional. *Phys. Rev. B*, **89**:035412, (2014).

[43] Julia Wiktor and Alfredo Pasquarello. Absolute deformation potentials of two-dimensional materials. *Phys. Rev. B*, **94**:245411, (2016).

[44] Julia Wiktor, Ursula Rothlisberger, and Alfredo Pasquarello. Predictive determination of band gaps of inorganic halide perovskites. *The Journal of Physical Chemistry Letters*, **8**:5507–5512, (2017). PMID: 29077408.

[45] Francesco Ambrosio, Julia Wiktor, Filippo De Angelis, and Alfredo Pasquarello. Origin of low electron–hole recombination rate in metal halide perovskites. *Energy Environmental Science*, **11**:101–105, (2018).

[46] Erik Jedvik, Anders Lindman, Magnús
THór Benediktsson, and Göran Wahnström. Size and shape of oxygen vacancies and protons in acceptor-doped barium zirconate. *Solid State Ionics*, **275**:2–8, (2015). 17th International Conference on Solid State Protonic Conductors, Seoul, Korea, 14-19 September 2014.

[47] Vivekanand Shukla, Yang Jiao, Jung-Hoon Lee, et al. Accurate Nonempirical Range-Separated Hybrid van der Waals Density Functional for Complex Molecular Problems, Solids, and Surfaces. *Phys. Rev. X*, **12**:041003, (2022).

[48] Jung-Hoon Lee, Per Hyldgaard, and Jeffrey B. Neaton. An Assessment of Density Functionals for Predicting CO_2 Adsorption in Diamine-Functionalized Metal-Organic Frameworks. *J. Chem. Phys.*, **156**:154113, (2022).

[49] Vivekanand Shukla, Yang Jiao, Carl M. Frostenson, and Per Hyldgaard. vdW-DF-ahcx: a range-separated van der Waals density functional hybrid. *J. Phys.: Condens. Matter*, **34**:025902, (2022).

[50] A. M. Beale, F. Gao, I. Lezcano-Gonzalez, et al. Recent advances in automotive catalysis for nox emission control by small-pore microporous materials. *Chem. Soc. Rev.*, **44**:7371–7405, (2015).

[51] Paolo Giannozzi, Stefano Baroni, Nicola Bonini, et al. QUANTUM ESPRESSO: a modular and open-source software project for quantum simulations of materials. *J. Phys.: Condens. Matter*, **21**:395502, (2009).

[52] P. Giannozzi, O. Andreussi, T. Brumme, et al. Advanced capabilities for materials modelling with quantum espresso. *J.Phys.: Condens. Matter*, **29**:465901, (2017).

[53] I. Carnimeo, S. Baroni, and P. Giannozzi. Fast hybrid density-functional computations using plane-wave beasis sets. *Electron. Struct.*, **1**:015009, (2019).

[54] P. Hohenberg and W. Kohn. Inhomogeneous electron gas. *Phys. Rev.*, **136**:B864, (1964).

[55] W. Kohn and L.J. Sham. Self-Consistent Equations Including Exchange and Correlation Effects. *Phys. Rev.*, **140**:1133–1138, (1965).

[56] O. Gunnarsson and B. I. Lundqvist. Exchange and correlation in atoms, molecules, and solids by the spin-density-functional formalism. *Phys. Rev. B*, **13**:4274–4298, (1976).

[57] David C. Langreth and John P. Perdew. Exchange-correlation energy of a metallic surface: Wave-vector analysis. *Phys. Rev. B*, **15**:2884–2901, (1977).

[58] K. Rapcewicz and N. W. Ashcroft. Fluctuation attraction in condensed matter: A nonlocal functional approach. *Phys. Rev. B*, **44**:4032–4035, (1991).

[59] David C. Langreth and S. H. Vosko. Exact electron-gas response functions at high density. *Phys. Rev. Lett.*, **59**:497–500, (1987).

[60] K. Burke, J. P. Perdew, and M. Levy. Modern density functional theory: A tool for chemistry. Elsevier, Amsterdam, (1995).

[61] R. O. Jones and O. Gunnarsson. The density functional formalism, its applications and prospects. *Rev. Mod. Phys.*, **61**:689–746, (1989).

[62] Marie Dumaz, Reese Boucher, Miguel A. L. Marques, and Aldo H. Romero. Authorship and citation cultural nature in density functional theory from solid state computational packages. *Scientometrics*, **126**:6681–6695, (2021).

[63] J. P. Perdew. Electronic structure of solids '91. Akademie Verlag, Berlin, (1991).

[64] A. D. Becke. Density-functional thermochemistry. III. The role of exact exchange. *J. Chem. Phys.*, **98**:5648, (1993).

[65] Richard M. Martin. *Electronic Structure: Basic Theory and Practical Methods*. Cambridge University Press, (2004).

[66] M. Born and R. Oppenheimer. Zur quantentheorie der molekeln. *Annalen der Physik*, **389**:457–484, (1927).

[67] Eberhard Engel and Reiner M. Dreizler. *Density Functional Theory: An Advanced Course*. Springer Berlin Heidelberg, (2011).

[68] C. C. J. Roothaan. New developments in molecular orbital theory. *Reviews of Modern Physics*, **23**:69–89, (1951).

[69] Per-Olov Löwdin. Quantum theory of many-particle systems. i. physical interpretations by means of density matrices, natural spin-orbitals, and convergence problems in the method of configurational interaction. *Physical Review*, **97**:1474–1489, (1955).

[70] I. Shavitt. The method of configuration interaction. *Methods of Electronic Structure Theory*, **3**:189–275, (1977).

[71] B. O. Roos, P. R. Taylor, and P. E. M. Siegbahn. A complete active space scf method (casscf) using a density matrix formulated super-ci approach. *Chemical Physics*, **48**:157–173, (1980).

[72] Stefano Racioppi, Phalgun Lolur, Per Hyldgaard, and Martin Rahm. A density functional theory for the average electron energy. *Journal of Chemical Theory and Computation*, **19**:799–807, (2023).

[73] James Daniel Whitfield, Peter John Love, and Alán Aspuru-Guzik. Computational complexity in electronic structure. *Phys. Chem. Chem. Phys.*, **15**:397–411, (2013).

[74] Norbert Schuch and Frank Verstraete. Computational complexity of interacting electrons and fundamental limitations of density functional theory. *Nature Physics*, **5**:732–735, (2009).

[75] L. H. Thomas. The calculation of atomic fields. *Mathematical Proceedings of the Cambridge Philosophical Society*, **23**:542–548, (1927).

[76] Enrico Fermi. Un metodo statistico per la determinazione di alcune priorieta dell'atome. *Rend. Accad. Naz. Lincei*, **602**, (1927).

[77] P. A. M. Dirac. Note on exchange phenomena in the thomas atom. *Mathematical Proceedings of the Cambridge Philosophical Society*, **26**:376–385, (1930).

[78] J. P. Perdew and Alex Zunger. Self-interaction correction to density-functional approximations for many-electron systems. *Phys. Rev. B*, **23**:5048–5079, (1981).

[79] D. C. Langreth and J. P. Perdew. The exchange-correlation energy of a metallic surface. *Solid State Commun.*, **17**:1425–1429, (1975).

[80] David C. Langreth and John P. Perdew. Exchange-correlation energy of a metallic surface: Wave-vector analysis. *Phys. Rev. B*, **15**:2884–2901, (1977).

[81] Yue Wang and John P. Perdew. Correlation hole of the spin-polarized electron gas, with exact small-wave-vector and high-density scaling. *Phys. Rev. B*, **44**:13298–13307, (1991).

[82] V. Fock. Näherungsmethode zur lösung des quantenmechanischen mehrkörperproblems. *Zeitschrift für Physik*, **61**:126–148, (1930).

[83] P. Hyldgaard, K. Berland, and E. Schröder. Interpretation of van der Waals density functionals. *Phys. Rev. B*, **90**:075148, (2014).

[84] M. Dion, H. Rydberg, E. Schröder, et al. Van der Waals Density Functional for General Geometries. *Phys. Rev. Lett.*, **92**:246401, (2004).

[85] L. Hedin and B. I. Lundqvist. Explicit local exchange-correlation potentials. *J. Phys. C*, **4**:2064, (1971).

[86] John P. Perdew and Wang Yue. Accurate and simple density functional for the electronic exchange energy: Generalized gradient approximation. *Phys. Rev. B*, **33**: 8800–8802, (1986).

[87] Axel D. Becke. Perspective: Fifty years of density-functional theory in chemical physics. *The Journal of Chemical Physics*, **140**:18A301, (2014).

[88] Axel D. Becke. Real-space post-Hartree-Fock correlation models. *The Journal of Chemical Physics*, **122**:064101, (2005).

[89] Kristian Berland and Per Hyldgaard. Analysis of van der Waals density functional components: Binding and corrugation of benzene and C_{60} on boron nitride and graphene. *Phys. Rev. B*, **87**:205421, (2013).

[90] John P. Perdew, Adrienn Ruzsinszky, Gábor I. Csonka, et al. Restoring the density-gradient expansion for exchange in solids and surfaces. *Phys. Rev. Lett.*, **100**:136406, (2008).

[91] Éamonn D. Murray, Kyuho Lee, and David C. Langreth. Investigation of exchange energy density functional accuracy for interacting molecules. *J. Chem. Theory Comput.*, **5**:2754–2762, (2009).

[92] Ikutaro Hamada. van der Waals density functional made accurate. *Phys. Rev. B*, **89**:121103(R), (2014).

[93] K. Lee, É. D. Murray, L. Kong, et al. Higher-Accuracy Van Der Waals Density Functional. *Phys. Rev. B*, **82**:8207–8215, (2010).

[94] C. Adamo and V. Barone. Towards reliable density functional methods without adjustable parameters: The PBE0 model. *J. Chem. Phys.*, **110**:6158, (1999).

[95] Fabien Tran, Leila Kalantari, Boubacar Traoré, et al. Nonlocal van der Waals functionals for solids: Choosing an appropriate one. *Phys. Rev. M*, **3**:063602, (2019).

[96] L. Gharaee, P. Erhart, and P. Hyldgaard. Finite-temperature properties of nonmagnetic transition metals: Comparison of the performance of constraint-based semi and nonlocal functionals. *Phys. Rev. B*, **95**:085147, (2017).

[97] T. Tchakoua, N. Gerrits, E. W. F. Smeets, and G.-J. Kroes. Sbh17: Benchmark database of barrier heights for dissociative chemisorption on transition metal surfaces. *Journal of Chemical Theory and Computation*, **19**:245–270, (2023). PMID: 36529979.

[98] Nick Gerrits, Stefan Vuckovic Egidius W. F. Smeets, Andrew D. Powell, et al. Density Functional Theory for Molecule-Metal Surface Reactions: When Does the Generalized Gradient Approximation Get It Right and What to Do If It Does Not. *Phys. Chem. Lett.*, **11**:10552, (2020).

[99] Mark Wijzenbroek, David M. Klein, Bauke Smits, et al. Performance of a non-local van der Waals density functional on the dissociation of H2 on metal surfaces. *J. Phys. Chem. A*, **119**:12146–12158, (2015). PMID: 26258988.

[100] Per Hyldgaard, Yang Jiao, and Vivekanand Shukla. Screening nature of the van der waals density functional method: a review and analysis of the many-body physics foundation. *Journal of Physics: Condensed Matter*, **32**:393001, (2020).

[101] B. Hammer and J. K. Norskov. Why gold is the noblest of all the metals. *Nature*, **376**:238–240, (1995).

[102] Kristian Berland, Valentino R Cooper, Kyuho Lee, et al. van der waals forces in density functional theory: a review of the vdw-df method. *Reports on Progress in Physics*, **78**:066501, (2015).

[103] H. Rydberg, B.I. Lundqvist, D.C. Langreth, and M. Dion. Tractable Nonlocal Correlation Density Functionals for Flat Surfaces and Slabs. *Phys. Rev. B*, **62**: 6997–7006, (2000).

[104] H. Rydberg, M. Dion, N. Jacobson, et al. Van der Waals Density Functional for Layered Structures. *Phys. Rev. Lett.*, **91**:126402, (2003).

[105] T. Thonhauser, Valentino R. Cooper, Shen Li, et al. Van der waals density functional: Self-consistent potential and the nature of the van der waals bond. *Phys. Rev. B*, **76**:125112, (2007).

[106] H. Rydberg. *Nonlocal correlations in density functional theory*. PhD thesis, Department of Applied Physics, Chalmers University of Technology, Göteborg, Sweden, (2001). `http://bitmath.se/rydberg/Thesis`.

[107] Elsebeth Schröder, Valentino R. Cooper, Kristian Berland, et al. The vdW-DF family of non-local exchange-correlation functionals. In Alberto Otero de la Roza and Gino Di Labio, editors, *Non-covalent Interactions in Quantum Chemistry and Physics: Theory and Applications*. Elsevier, Amsterdam, (2017).

[108] A. D. Becke. On the large-gradient behavior of the density functional exchange energy. *J. Chem. Phys.*, **85**:7184–7187, (1986).

[109] Yingkai Zhang and Weitao Yang. Comment on "generalized gradient approximation made simple". *Phys. Rev. Lett.*, **80**:890–890, (1998).

[110] Thomas M. Henderson, Benjamin G. Janesko, and Gustavo E. Scuseria. Generalized gradient approximation model exchange holes for range-separated hybrids. *The Journal of Chemical Physics*, **128**:194105, (2008).

[111] K. Burke, M. Ernzerhof, and J. P. Perdew. The adiabatic connection method: a non-empirical hybrid. *Chem. Phys. Lett.*, **265**:115, (1997).

[112] Kristian Berland, Yang Jiao, Jung-Hoon Lee, et al. Assessment of two hybrid van der waals density functionals for covalent and noncovalent binding of molecules. *J. Chem. Phys.*, **146**:234106, (2017).

[113] Jonathan H. Skone, Marco Govoni, and Giulia Galli. Self-consistent hybrid functional for condensed systems. *Phys. Rev. B*, **89**:195112, (2014).

[114] Yang Jiao, Elsebeth Schröder, and Per Hyldgaard. Extent of Fock-exchange mixing for a hybrid van der Waals density functional? *J. Chem. Phys.*, **148**:194115, (2018).

[115] O. H. Nielsen and Richard M. Martin. Quantum-mechanical theory of stress and force. *Phys. Rev. B*, **32**:3780, (1985).

[116] Riccardo Sabatini, Emine Küçükbenli, Brian Kolb, et al. Structural evolution of amino acid crystals under stress from a non-empirical density functional. *J. Phys.: Condens. Matter*, **24**:424209, (2012).

[117] Yashar Yourdshayan, Carlo Ruberto, Mats Halvarsson, et al. Theoretical Structure Determination of a Complex Materials: κ-Al_2O_3. *J. Am. Ceram. Soc.*, **82**:1365–80, (1999).

[118] Carlo Ruberto, Yashar Yourdshahyan, and Bengt I. Lundqvist. Stability of a Flexible Polar Ionic Crystal Surface: Metastable Alumina and One-Dimensional Surface Metallicity. *Phys. Rev. Lett.*, **88**:226101, (2002).

[119] Carlo Ruberto, Yashar Yourdshahyan, and Bengt I. Lundqvist. Surface properties of metastable alumina: A comparative study of κ- and α-Al_2O_3. *Phys. Rev. B*, **67**: 195412, (2003).

[120] Behrooz Razaznejad, Carlo Ruberto, Per Hyldgaard, and Bengt I. Lundqvist. Self-Organized One-Dimensional Electron Systems on a Low-Symmetry Oxide Surface. *Phys. Rev. Lett.*, **90**:236803, (2003).

[121] Jochen Rohrer, Carlo Ruberto, and Per Hyldgaard. Ab initio structure modelling of complex thin-film oxides: thermodynamical stability of TiC/thin-film alumina. *J. Phys.: Condensed Matter*, **22**:015004, (2010).

[122] Jochen Rohrer and Per Hyldgaard. Understanding adhesion at as-deposited interfaces from ab initio thermodynamics of deposition growth: thin-film alumina on titanium carbide. *J. Phys.: Condensed Matter*, **22**:015004, (2010).

[123] Jochen Rohrer and Per Hyldgaard. Stacking and band structure of van der waals bonded graphane multilayers. *Phys. Rev B*, **83**:165423, (2011).

[124] J. L. Koenig and J. J. Mannion. Infrared study of poly(vinyl fluoride). *Journal of Polymer Science Part A-2: Polymer Physics*, **4**:401–414, (1966).

[125] J. B. Lando, H. G. Olf, and A. Peterlin. Nuclear magnetic resonance and x-ray determination of the structure of poly(vinylidene fluoride). *Journal of Polymer Science Part A-1: Polymer Chemistry*, **4**:941–951, (1966).

[126] G. Zerbi and G. Cortili. Structure of poly-(vinyl fluoride) from its infrared spectrum. *Spectrochimica Acta Part A: Molecular Spectroscopy*, **26**:733–739, (1970).

[127] G Natta, L Porri, and A Carbonaro. Atti. accad. nazl. lincei, rend., classe sci. fis., mat. e nat. **In *Chem. Abstr.*** 55, (1961).

[128] J.W. Hong, J.B. Lando, J.L. Koenig, et al. Normal-mode analysis of infrared and raman spectra of poly(vinyl fluoride). *Vibrational Spectroscopy*, **3**:55–66, (1992).

[129] Eleni Ziambaras and Elsebeth Schröder. Theory for structure and bulk modulus determination. *Phys. Rev. B*, **68**:064112, (2003).

[130] Francis Birch. Finite elastic strain of cubic crystals. *Physical Review*, **71**:809–824, (1947).

[131] F. D. Murnaghan. The compressibility of media under extreme pressures. *Proceedings of the National Academy of Sciences*, **30**:244–247, (1944).

[132] Harry Nyquist. Certain topics in telegraph transmission theory. *AIEE Transactions*, **47**:617–644, (1928).

[133] Ryozo Hasegawa, Yasuhiro Takahashi, Yozo Chatani, and Hiroyuki Tadokoro. Crystal structures of three crystalline forms of poly(vinylidene fluoride). *Polymer Journal*, **3**:600–610, (1972).

[134] Max Born. On the stability of crystal lattices. i. *Mathematical Proceedings of the Cambridge Philosophical Society*, **36**:160–172, (1940).

[135] Fedor I. Fedorov. *Theory of Elastic Waves in Crystals*. Springer US, (1968).

[136] Félix Mouhat and Francois Xavier Coudert. Necessary and sufficient elastic stability conditions in various crystal systems. *Phys. Rev. B*, **90**:224104, (2014).

[137] R. D. King-Smith and David Vanderbilt. Theory of polarization of crystalline solids. *Physical Review B*, **47**:1651, (1993).

[138] Raffaele Resta. Macroscopic polarization in crystalline dielectrics: the geometric phase approach. *Rev. Mod. Phys.*, **66**:899–915, (1994).

[139] Raffaele Resta. Quantum-mechanical position operator in extended systems. *Physical Review Letters*, **80**:1800, (1998).

[140] David Vanderbilt. *Berry Phases in Electronic Structure Theory: Electric Polarization, Orbital Magnetization and Topological Insulators*. Cambridge University Press, (2018).

[141] N. W. Ashcroft and N. D. Mermin. *Solid State Physics*. Holt-Saunders, (1976).

[142] Nicola Marzari, David Vanderbilt, and M. C. Payne. Maximally localized generalized wannier functions for composite energy bands. *Physical Review B*, **56**:12847, (1997).

[143] L.M. Mirica, X. Ottenwaelder, and T.D.P. Stack. Structure and Spectroscopy of Copper-Dioxygen Complexes. *Chem. Rev*, **104**:1013–1046, (2004).

[144] M. Metz and E.I. Solomon. Dioxygen Binding to Deoxyhemocyanin: Electronic Structure and Mechanism of the Spin-Forbidden Two-Electron Reduction of O_2. *J. Am. Chem. Soc.*, **123**:4938–4950, (2001).

[145] E.I. Solomon, D.E. Heppner, E.M. Johnston, et al. Copper Active Sites in Biology. *Chem. Rev*, **114**:3659–3853, (2014).

[146] B.M. Lam, J.A. Halfen, V.G. Young, et al. Ligand Macrocycle Structural Effects on Copper-Dioxygen Reactivity. *Inorg. Chem.*, **39**:4059–4072, (2000).

[147] Rosendo Valero, Ramon Costa, Iberio de P. R. Moreira, et al. Performance of the M06 family of exchange-correlation functionals for predicting magnetic coupling in organic and inorganic molecules. *J. Chem. Phys.*, **128**:114103, (2008).

[148] Pablo Rivero, Christoph Loschen, Iberio De P. R. Moreira, and Francesc Illas. Performance of Plane-Wave-Based LDA plus U and GGA plus U Approaches to Describe Magnetic Coupling in Molecular Systems. *J. Comput. Chem.*, **30**:2316–2326, (2009).

[149] K. P. Huber and G. Herzberg. *Molecular Spectra and Molecular Structure*. Springer US, (1979).

[150] G. Henkelman and H. Jónsson. Improved Tangent Estimate in the Nudged Elastic Band Method for Finding Minimum Energy Paths and Saddle Points. *J. Chem. Phys.*, **113**:9978–9985, (2000).

[151] D. Walter and P. B. Armentrout. Sequential Bond Dissociation Energies of $M^+(NH_3)_x$ (x = 1-4) for M = Ti-Cu. *J. Am. Chem. Soc.*, **120**:3176–3187, (1998).

[152] Chiara Negri, Tommaso Selleri, Elisa Borfecchia, et al. Structure and Reactivity of Oxygen-Bridged Diamino Dicopper(II) Complexes in Cu-Ion-Exchanged Chabazite Catalyst for NH_3-Mediated Selective Catalytic Reduction. *J. Am. Chem. Soc.*, **142**: 15884–15896, (2020).

[153] Pär A. T. Olsson, Elsebeth Schröder, Per Hyldgaard, et al. Ab initio and classical atomistic modelling of structure and defects in crystalline orthorhombic polyethylene: Twin boundaries, slip interfaces, and nature of barriers. *Polymer*, **121**:234–246, (2017).

[154] F. Pelizza, B.R. Smith, and K. Johnston. A van der waals density functional theory study of poly(vinylidene difluoride) crystalline phases. *The European Physical Journal Special Topics*, **225**:1733–1742, (2016).

[155] Francesco Pelizza and Karen Johnston. A density functional theory study of poly(vinylidene difluoride) crystalline phases. *Polymer*, **179**:121585, (2019).

[156] R R. Large, W.G. Maddams, , and J.E. Preedy. X-ray-diffraction pole figure measurements on a polyvinyl fluoride) film. *Journal of Applied Polymer Science*, **22**: 3031–3033, (1978).

[157] Bruno Ameduri. Fluoropolymers: The right material for the right applications. *Chemistry – A European Journal*, **24**:18830–18841, (2018).

[158] Mahua G. Dhara and Susanta Banerjee. Fluorinated high-performance polymers: Poly(arylene ether)s and aromatic polyimides containing trifluoromethyl groups. *Progress in Polymer Science*, **35**:1022–1077, (2010).

[159] Maryam Bozorg, Aldo Altomare, and Katja Loos. 4 - synthesis of polyvinylidene fluoride and its copolymers. In Kamal Asadi, editor, *Organic Ferroelectric Materials and Applications*, Woodhead Publishing Series in Electronic and Optical Materials, 8 page. Woodhead Publishing, (2022).

[160] Bruno Ameduri and Bernard Boutevin. *Well-architectured fluoropolymers: synthesis, properties and applications*. Elsevier, (2004).

[161] Albert L. Moore. 2 - fluoroelastomer composition and properties. In Albert L. Moore, editor, *Fluoroelastomers Handbook*, Plastics Design Library, 1 page. William Andrew Publishing, Norwich, NY, (2006).

[162] Jiri George Drobny. 3 - fluoroelastomer composition and properties. In Jiri George Drobny, editor, *Fluoroelastomers Handbook (Second Edition)*, Plastics Design Library, 1 page. William Andrew Publishing, second edition edition, (2016).

[163] Bruno Ameduri. From vinylidene fluoride (vdf) to the applications of vdf-containing polymers and copolymers: Recent developments and future trends. *Chemical Reviews*, **109**:6632–6686, (2009). PMID: 19731907.

[164] Vanessa Cardoso, Daniela Correia, Clarisse Ribeiro, et al. Fluorinated polymers as smart materials for advanced biomedical applications. *Polymers*, **10**:161, (2018).

[165] Jeremy J Reisinger and Marc A Hillmyer. Synthesis of fluorinated polymers by chemical modification. *Progress in Polymer Science*, **27**:971–1005, (2002).

[166] Heiji Kawai. The piezoelectricity of poly (vinylidene fluoride). *Japanese Journal of Applied Physics*, **8**:975, (1969).

[167] Koh Nakamura, Masayuki Nagai, Tetsuo Kanamoto, et al. Development of oriented structure and properties on drawing of poly(vinylidene fluoride) by solid-state coextrusion. *Journal of Polymer Science Part B: Polymer Physics*, **39**:1371–1380, (2001).

[168] Akira Itoh, Yoshiyuki Takahashi, Takeo Furukawa, and Hirofumi Yajima. Solid-state calculations of poly(vinylidene fluoride) using the hybrid dft method: spontaneous polarization of polymorphs. *Polymer Journal*, **46**:207–211, (2014).

[169] Fu-Chang Sun, Avinash M. Dongare, Alexandru D. Asandei, et al. Temperature dependent structural, elastic, and polar properties of ferroelectric polyvinylidene fluoride (pvdf) and trifluoroethylene (trfe) copolymers. *Journal of Materials Chemistry C*, **3**:8389–8396, (2015).

[170] M. S. Miao, M.-L. Zhang, V. E. Van Doren, et al. Density functional calculations on the structure of crystalline polyethylene under high pressures. *The Journal of Chemical Physics*, **115**:11317–11324, (2001).

[171] G. Avitabile, R. Napolitano, B. Pirozzi, et al. Low temperature crystal structure of polyethylene: Results from a neutron diffraction study and from potential energy calculations. *Journal of Polymer Science: Polymer Letters Edition*, **13**:351–355, (1975).

[172] S. Kavesh and J. M. Schultz. Lamellar and interlamellar structure in melt-crystallized polyethylene. i. degree of crystallinity, atomic positions, particle size, and lattice disorder of the first and second kinds. *Journal of Polymer Science Part A-2: Polymer Physics*, **8**:243–276, (1970).

[173] P. W. Teare. The crystal structure of orthorhombic hexatriacontane, C_36H_74. *Acta Crystallographica*, **12**:294–300, (1959).

[174] Andrew J. Lovinger. Unit cell of the x phase of poly(vinylidene fluoride). *Macromolecules*, **14**:322–325, (1981).

[175] Ask Hjorth Larsen, Jens Jørgen Mortensen, Jakob Blomqvist, et al. The atomic simulation environment—a python library for working with atoms. *Journal of Physics: Condensed Matter*, **29**:273002, (2017).

[176] Shyue Ping Ong, William Davidson Richards, Anubhav Jain, et al. Python materials genomics (pymatgen): A robust, open-source python library for materials analysis. *Computational Materials Science*, **68**:314–319, (2013).

[177] Jens Jørgen Mortensen, Ask Hjorth Larsen, Mikael Kuisma, et al. Gpaw: An open python package for electronic structure calculations. *The Journal of Chemical Physics*, **160**:092503, (2024).

[178] J. J. Mortensen, L. B. Hansen, and K. W. Jacobsen. Real-space grid implementation of the projector augmented wave method. *Phys. Rev. B*, **71**:035109, (2005).

[179] J Enkovaara, C Rostgaard, J J Mortensen, et al. Electronic structure calculations with gpaw: a real-space implementation of the projector augmented-wave method. *Journal of Physics: Condensed Matter*, **22**:253202, (2010).

[180] Thomas D. Kühne, Marcella Iannuzzi, Mauro Del Ben, et al. CP2k: An electronic structure and molecular dynamics software package - quickstep: Efficient and accurate electronic structure calculations. *The Journal of Chemical Physics*, **152**: 194103, (2020).

[181] M. Valiev, E.J. Bylaska, N. Govind, et al. Nwchem: A comprehensive and scalable open-source solution for large scale molecular simulations. *Computer Physics Communications*, **181**:1477–1489, (2010).

[182] Xavier Gonze, Bernard Amadon, Gabriel Antonius, et al. The abinit project: Impact, environment and recent developments. *Comput. Phys. Commun.*, **248**:107042, (2020).

[183] Aldo H. Romero, Douglas C. Allan, Bernard Amadon, et al. Abinit: Overview, and focus on selected capabilities. *J. Chem. Phys.*, **152**:124102, (2020).

[184] J. K. Nørskov, J. Rossmeisl, A. Logadottir, et al. Origin of the overpotential for oxygen reduction at a fuel-cell cathode. *The Journal of Physical Chemistry B*, **108**: 17886–17892, (2004).

[185] J. Rossmeisl, Z.-W. Qu, H. Zhu, et al. Electrolysis of water on oxide surfaces. *Journal of Electroanalytical Chemistry*, **607**:83–89, (2007). Theoretical and Computational Electrochemistry.

[186] Isabela C. Man, Hai-Yan Su, Federico Calle-Vallejo, et al. Universality in oxygen evolution electrocatalysis on oxide surfaces. *ChemCatChem*, **3**:1159–1165, (2011).

[187] Yongquan Zhou, Toshio Yamaguchi, Wenqian Zhang, et al. The structural elucidation of aqueous h3bo3 solutions by dft and neutron scattering studies. *Phys. Chem. Chem. Phys.*, **22**:17160–17170, (2020).

[188] Xiaotian Zhao, YaMing Li, Shibo Lin, et al. Dft studies of solvent effect in hydrogen abstraction reactions from different allyl-type monomers with benzoyl radical. *BMC Chemistry*, **17**, (2023).

[189] Claudio Zeni, Robert Pinsler, Daniel Zügner, et al. Mattergen: a generative model for inorganic materials design. (2023).